INFLUENCE OF HEAT TREATMENT ON HEAT AFFECTED ZONE MICROFISSURING IN EB WELDED MICROCAST-X INCONEL 718

by

Gerard Cadieux

A thesis submitted to the faculty of Graduate studies in partial fulfillment of the requirements for the degree of

Master of Science in Mechanical Engineering

Department of Mechanical and Industrial Engineering

University of Manitoba

Winnipeg, Manitoba

December 1997

THE UNIVERSITY OF MANITOBA

FACULTY OF GRADUATE STUDIES

*****

COPYRIGHT PERMISSION PAGE

INFLUENCE OF HEAT TREATMENT ON HEAT AFFECTED ZONE MICROFISSURING IN EB WELDED MICROCAST-X INCONEL 718

BY

GERARD CADEIUX

A Thesis/Practicum submitted to the Faculty of Graduate Studies of The University of Manitoba in partial fulfillment of the requirements of the degree of

MASTER OF SCIENCE

ACKNOWLEDGMENTS

I would like to take this opportunity to thank Dr. M.C. Chaturvedi and Dr. N.L. Richards for their expert advice and guidance. Thanks are due to NSERC and Manitoba Hydro for their financial support and the Electrical and Mechanical Engineering Department of Manitoba Hydro as well as the Materials and Processes Lab at Bristol Aerospace for giving me the opportunity to work with them for some time.

I would like to thank the following people for their advice and assistance; Dr. Naresh Goel, Dr. Gou, Dr. Xu, Dr. Weixing Chen, Dr. Xiao Huang, Anurag Thakur, Wenji Fan, and Jason Zagula. I would also like to thank Dr. Gregory McMahon and CANMET labs in Ottawa for their expert assistance in performing the SIMS analysis and Dr. Xu for his assistance with the TEM analysis.

Special thanks are due to our invaluable technicians Don Mardis and John Van Dorp for their assistance with lab practices, their unending patience, and their ever-present technical support without which the lab could not possibly function. I would also like to thank John Davies of Bristol Aerospace for assisting in perfroming the electron beam welding of specimens.

I would also like to extend my deepest gratitude to my family and friends for their ever-present support and encouragement.

ABSTRACT

A new form of cast Inconel 718 has recently been receiving attention as it has demonstrated improved mechanical properties over that of the conventionally cast material and is now being introduced in many investment cast components including high pressure housings for liquid rocket boosters in NASA's SSME (Space Shuttle Main Engine) program. This new form is known as Microcast-X (MX) investment cast alloy 718 and was developed and patented by Howmet corporation. MX-cast components are characterized by a uniform, homogenous, fine-grained microstructure of ASTM grain size 4 to 5. This fine-grained cast structure is achieved through a low pouring temperature of a few degrees above the liquidus of the alloy.

Recent studies on both conventionally cast and wrought alloy 718 have suggested that elemental segregation of trace elements, in particular boron, to grain boundaries during heat treatment can greatly affect microfissuring susceptibility during welding. Boron is suspected to act as a grain boundary melting point suppressant. It has been sugested that an increase in boron grain boundary concentration may cause a corresponding decrease in the melting point of the grain boundaries. Decreasing the melting point of HAZ grain boundaries in turn aggravates HAZ microfissuring by encouraging further grain boundary melting and allowing additional time for grain boundary wetting and grain boundary sliding under the influence of welding stresses.

Specimens were given an initial pre-weld homogenization heat treatment at 1200 °C and water quenched followed by solution heat treatments at 1050, 1100, and 1150 °C which were designed to maintain a fine-grained and "clean" microstructure while allowing sufficient time for equilibrium segregation of sulfur. Both air cooling and water quenching were used for each solution heat treatment to study the effect of cooling rate on both boron segregation levels and HAZ microfissuring susceptibility.

Electron beam welding is used in commercial repair welding and joining practices due to the high quality of weld achievable using this technique and was used in this study. HAZ microfissuring measurements as well as microstructural observations and characterization were conducted using Scanning Electron Microscopy (SEM), Transmission Electron Microscopy (TEM), Energy Dispersive Spectroscopy (SEM/EDS and TEM/EDS), Secondary Ion Mass Spectrometry (SIMS), and Orientation Imaging Microscopy (OIM).

Results indicate that boron segregation increases with increasing solution heat treatment temperature and decreasing cooling rate and that microfissuring levels coincide with observed levels of boron segregation. HAZ microfissuring analysis results suggest common liquation cracking mechanisms were operating for all heat treated conditions analyzed. Air cooled specimens demonstrated greater microfissuring than water quenched specimens at each solution heat treatment temperature in agreement with the observed increased level of boron segregation in air cooled specimens.

TABLE OF CONTENTS

LIST OF FIGURES

LIST OF TABLES

Page

CHAPTER ONE

INTRODUCTION

Alloy 718 was first developed in the early 1960's and has since risen in prominence and popularity as one of today's most widely used superalloys. Alloy 718 is a nickel-iron-chromium base superalloy strengthened primarily by γ'' precipitation. The alloy exhibits exceptional strength characteristics over a wide temperature range from cryogenic temperatures to 650 °C and is not susceptible to the common strain age cracking problems associated with many superalloys. Alloy 718 was first used in wrought form and still is today, however, over the years, it became evident that many parts used in gas turbine aircraft engines could be made much more economically if they were investment cast into complex near-net shape components requiring little additional machining which had previously been a series of components welded together. Investment casting also improves component integrity over a component fabricated as a welded assembly of parts.

Cast components, however, have been found to be more susceptible to weld heat affected zone microfissuring and have been shown to possess mechanical properties below those of wrought material. As a result, Howmet developed a technique of investment casting fine-grained components of ASTM grain size 3 to 5, termed the Microcast-X (MX) process. Microcast-X Alloy 718 has been shown to possess improved mechanical properties over the conventionally cast material which approach the mechanical properties of the wrought material. These improvements are due in large part to the uniform, equiaxed, non-dendritic,

fine-grain microstructure achieved in MX cast components. The MX process was first reported in 1984 and has since resulted in MX cast components being used in many applications including high pressure liquid fuel rocket housings for NASA's Space Shuttle Main Engine (SSME) program [1].

Welding of cast components both in assembly and repair operations is an integral part of superalloy production and use and, thus, it is important that welding behaviour and properties be studied in order to improve weld integrity and reduce or eliminate persistent problems such as heat-affected zone (HAZ) microfissuring. Since the MX alloy has demonstrated improved performance over the conventionally cast material it is deemed useful to study the weldability of this alloy and the effect of pre-weld heat treatments both on microstructure and welding characteristics. Electron-beam welding is chosen as it is one of the optimal choices for welding since it provides extremely high quality welds.

Recent studies on wrought and conventionally cast Alloy 718 material have demonstrated that elemental segregation of trace elements, in particular boron and sulfur, to grain boundaries during pre-weld heat treatments may be a major factor contributing to the HAZ microfissuring problem. Thus the present study will pay careful attention to the segregation of boron and sulfur and how they relate to heat treatments and HAZ microfissuring susceptibility.

CHAPTER TWO

LITERATURE REVIEW

2.1 Introduction

Superalloy development began when the need for alloys which could withstand the high operating temperatures of aircraft engines increased through the 1930s and beyond [2:5]. Superalloy advances continued through the 1940s as the demand for alloys able to withstand higher and higher temperatures increased with the continuous advance of gas turbine engine technology. Superalloys are used extensively in aircraft, marine, industrial, and vehicular gas turbines and are now found in space vehicles, rocket engines, nuclear reactors, submarines, steam power plants, and other high-temperature applications as well as some cryogenic applications. Superalloys today account for over 70% of aircraft engine weight as compared to 10% in early aircraft gas turbines and the turbine inlet temperatures have increased from 950 °C to over 1500 °C in some of today's advanced machines [3:33]. Superalloy use has also allowed great increases in times between overhaul and increased life spans. Superalloys may be divided into three main groups: cobalt base, iron base, and nickel base. Inconel 718 is often regarded as a nickel-iron-chromium base alloy but is considered part of the nickel-base class.

2.2 Superalloys

2.2.1 Mechanical Properties

The existence of superalloys can be attributed primarily to their outstanding ability to maintain excellent tensile, rupture and creep properties at high temperatures. The face-centered-cubic (FCC) lattice of these alloys allows for good control of precipitating intermetallic phases and solid solution hardening effects. Superalloys must also demonstrate good characteristics in many different mechanical properties. Good ductility is of key importance as well as impact resistance, high and low cycle fatigue (HCF and LCF) resistance, weldability, and thermal fatigue resistance [3:35]. Density should be kept low in order to reduce weight and, in the case of rotating components, reduce centrifugal stresses. Low thermal expansion is important to reduce thermal stresses and minimize expansion since components are often fabricated with close tolerances [3:35].

Microstructural stability is an important factor which affects the ability of a superalloy to maintain its mechanical properties. Phases may become unstable and may transform or melt when subjected to high temperatures and stresses. It is often the ability of a superalloy to form or maintain phases which provide its high strength and creep resistance at high temperatures that determines the usefulness of the alloy in many applications.

Surface stability is also of great importance as the environments in which superalloys are used are often very aggressive (corrosive and erosive) such as the hot, high-velocity fuel-burning environment of gas turbines engines. Thus good oxidation and hot corrosion resistance are essential [2:17-20].

2.2.2 Strengthening Mechanisms

Superalloys are typically extensively alloyed. These various alloying elements each play specific roles in strengthening the superalloy. Some, such as molybdenum, are typically used as solid solution strengtheners while others produced precipitate phases such as carbides or γ' particles which greatly increase the strength of the alloy. It is the temperature range in which these strengthening phases remain stable which determines the temperature range over which the superalloy may be used without significant degradation of mechanical properties. Processing techniques such as hot and cold working may further improve alloy properties through various microstructural changes.

2.2.3 Processing Techniques

Superalloy components may be produced via several methods among which the most common are casting and forging. Vacuum induction melting (VIM) is one of the primary

methods of producing the alloy of a desired composition and minimizing impurities. VIM removes oxygen and nitrogen from the melt which prevents the formation of oxide and nitride inclusions [2:21,4:183]. Superheat and temperature control is important as casting properties, such as fluidity, and final cast microstructure are dependent upon solidification behaviour and rates..

Forgings

Wrought nickel-base alloys first appeared in the 1940s and were used in forged turbine blades [2:20]. As the industry grew, different wrought superalloys were developed for specific applications such as sheet material for use in welded-fabricated components. Nickel-base alloys are often used in forged turbine disks. Welding of superalloys has always been difficult and many are susceptible to cracking due to post-weld heat treatments referred to as strain-age cracking. Inconel 718 is unique in that it is highly resistant to strain-age cracking due to the sluggish age hardening characteristics of the alloy.

Investment Castings

As a result of the high strength of superalloys and the fact that they are designed specifically to resist high temperature deformation they are often very difficult and costly if not

impossible to forge. Thus it is often highly beneficial to cast components of high strength and low forgeability. The near-net shape achieved with investment castings is also beneficial as it improves material usage and reduces additional machining and thus tool wear [5]. Vacuum investment casting allows lower pouring temperatures which allows better control and reduction of grain size as well as maintaining purity. As a result of advances in the precision casting industry, investment cast turbine airfoils are found in most modern engines for commercial and military aircraft.

Thin-walled ceramic shell molds which can be selectively insulated, ceramic cores, and inoculating agents in the mold interior surface have allowed great improvements in casting microstructural and shape control. Components which were once an assembly of castings welded together can now be cast as a single component thus improving component integrity while reducing cost of fabrication. The typical disadvantages of 718 investment castings have been found to be porosity, coarse grain size, and segregation effects [5]. HIPing, microcasting, and heat treatments have been found to be effective ways of reducing these problems and will be discussed later in detail.

2.3 Metallurgy of Inconel 718

2.3.1 Introduction

Inconel 718 is a γ'' strengthened superalloy and thus is resistant to the strain age cracking problem to which γ' strengthened superalloys are highly susceptible. As a result of this and other desirable properties and characteristics, Inconel 718 has become one of the most widely favoured of superalloys for many high temperature applications. Some general physical properties of Inconel 718 as quoted by Overfelt (et al.) are provided in Table 2-1 [6].

Thermal Conductivity [W/m K]	30.0
Density [kg/m^3]	7632
Total Latent Heat [kJ/kg]	295
Liquidus Temperature [K]	1603
Solidus Temperature [K]	1461

2.3.2 Mechanical Properties

In general, Inconel 718 is a highly favoured alloy for high temperature applications because of its high strength at high temperatures. The typical operating range for Inconel 718 is 540

to 560 °C. The mechanical properties of the alloy begin to degrade at 650 °C. The alloy also maintains a high yield, notch and tensile strength in low temperature environments thus making it useful in many cryogenic applications. The alloy is also well known for its high oxidation and hot corrosion resistance. One of the most important properties of Inconel 718 is its high stress-rupture strength at both high and low temperatures.

One of the primary reasons for the existence of MX (Microcast-X) IN-718 is the improved performance it has demonstrated in several areas of mechanical properties over the conventionally cast material. Stress-rupture life, low cycle fatigue (LCF), high cycle fatigue (HCF), tensile and yield strength are the properties for which the MX alloy has shown improvement over the conventionally cast (CC) material [7]. The LCF of the MX alloy was found to be twice that of the CC material and equal to that of wrought 718. The HCF life of the MX alloy was found to be 5 to 14 times longer than CC with wrought 718 having a 3 to 5 time HCF advantage over the MX alloy. Table 2-2 compares the tensile and yield strength of wrought, MX cast, and conventionally cast alloys as found by Bouse and Behrendt [7].

Alloy Type	Tensile strength [MPa]	Yield strength [MPa]	% Elongation
Wrought	1317	1056	48.1
Microcast-X (HIP at 1120 °C)	1146	942	23.1
Conv. Cast (HIP at 1120 °C)	970	831	28.9
Conv. Cast (HIP at 1165 °C)	1017	891	31.2

2.3.3 Composition and Effect of Alloying Elements

Inconel 718 is a complex alloy formed of many different alloying elements each of which plays a particular role in producing the microstructure and properties of the alloy. Table 2-3 provides the nominal composition of Inconel 718. Nickel provides the stable, ductile austenitic matrix while iron reduces cost and promotes γ'' formation. Iron, however, has been found to reduce the solubility temperature of precipitate phases and thus the maximum service temperature for the alloy is lowered.

Nickel (Ni)	50.0 - 55.0	Silicon (Si)	0.35 (max)
Chromium (Cr)	17.0 - 21.0	Manganese (Mn)	0.35 (max)
Iron (Fe)	Balance	Boron (B)	0.006 (max)
Niobium (Nb)	4.75 - 5.50	Phosphorus (P)	0.009 (max)
Molybdenum (Mo)	2.80 - 3.30	Sulfur (S)	0.015 (max)
Titanium (Ti)	0.65 - 1.15	Magnesium (Mg)	<0.001
Aluminum (Al)	0.20 - 0.80	Carbon (C)	0.08 (max)

Solid-Solution Strengtheners

Those alloying elements which act as solid-solution strengtheners in Inconel 718 and other nickel-iron base superalloys are primarily chromium (Cr), molybdenum (Mo), titanium (Ti), aluminum (Al), and niobium (Nb) [4:169]. The lattice parameter of cobalt is too close to that of nickel and iron to be an effective solid-solution strengthener. Carbon, vanadium and zirconium can also provide some solid-solution strengthening but this is not their primary role. Solid-solution strengthening is achieved by introducing lattice strain which in turn may affect precipitation hardening since the strength achieved through precipitation hardening is related to the degree of mismatch or coherency between the precipitate particles and the matrix [4:169].

Precipitation Strengtheners

Precipitation strengthening is achieved through several different mechanisms. The primary mode of precipitation strengthening is by impeding the motion of dislocations and thus impeding plastic deformation. Precipitate size, shape, distribution, and orientation will affect its interaction with the surrounding matrix and dislocation movement as well as grain boundary movement.

Niobium is the primary precipitation strengthener as it forms the BCT Ni_3Nb γ'' phase. Aluminum and Titanium both form the FCC $Ni_3(Al,Ti)$ γ' phase. Higher levels of titanium increase strength and discourage the formation of some deleterious phases while extra aluminum additions will increase the γ' solvus temperature and discourage γ' transition to η-phase. MC-type carbides are formed with titanium, molybdenum, niobium, vanadium, zirconium and tantalum.

Effects of Other Alloying Elements

Chromium provides the principle source of oxidation and hot corrosion (sometimes referred to as sulfidation) resistance. High silicon and niobium and low aluminum contents typically encourage δ formation [4:181]. Boron and zirconium are added to improve workability and stress rupture properties by promoting the coalescence and spherodization of precipitate

phases at the grain boundaries thereby creating a more ductile grain boundary [4:171]. Increasing boron and zirconium additions will minimize Laves and μ phase formation while increasing aluminum, titanium, niobium and silicon will promote Laves phase formation [4, 8]. Thompson found a 60% increase in titanium produced an average 137% increase in Laves phase found in cast fine-grained 718 [9].

Magnesium is used as a refining element to remove impurities such as oxygen, nitrogen, and sulfur. Manganese and silicon are added to increase workability and act as deoxidizers. Carbon also acts as a deoxidant through carbide formation. Phosphorus additions have recently been shown to increase stress rupture life at 650 °C [8,10,11]. Ultra-low P content has also recently been shown to have no obvious effect on high and low cycle fatigue (HCF and LCF) properties [12].

2.3.4 Microstructure

Due to the many alloying elements present in Inconel 718 the alloy has a very complex microstructure. As a result of processing, heat treating, or in-service use, several secondary phases can be formed, dissolved, liquated, or transformed depending on the conditions the alloy experiences. It is thus useful to describe the base metal matrix as well as the morphology and microstructural effects of common secondary phases found in Inconel 718 to further understand the characteristics of the alloy.

Gamma (γ) Matrix:

The gamma (γ) matrix is an FCC nickel-iron-base austenitic phase with chromium (Cr), molybdenum (Mo), and niobium (Nb) as the principle solid solution strengtheners.

Gamma Double Prime (γ'') Phase

The γ'' phase is a metastable Ni_3Nb phase which provides the principle precipitation age hardening of Inconel 718. γ'' precipitates appear as fine coherent disk-shaped particles of BCT (body centered tetragonal) crystal structure commonly with lattice parameters a_0 = 3.624 and c_0 = 7.406 [4:176]. Iron promotes γ'' formation by enabling favorable electronic and crystallographic conditions for precipitation while chromium promotes γ'' precipitation through favorable mismatch conditions. Due to the slower rate of formation of γ'' than γ' the alloy is resistant to strain age cracking sensitivity. If the alloy is over-aged (i.e. exposed to temperatures above 650 °C for extended periods of time) the γ'' particles will begin transforming to δ phase which is a much less effective strengthening phase and thus the alloy will lose much of its strength. The solvus temperature of γ'' in Inconel 718 is approximately 915 °C [4:184].

Gamma Prime (γ') Phase

The γ' phase is a $Ni_3(Al,Ti)$ ordered FCC secondary precipitate strengthening phase. Depending upon the aging and heat treatment used, γ' precipitates can form as spheroidal or cubic particles or as platelets. It has been shown that hardening increases with increasing γ' particle size until a peak hardening is reached and then decreases with further γ' growth. The ratio of aluminum and titanium must be carefully controlled as they each play a specific role (see section 2.3.2). γ' will begin to transform to η phase at extended exposure to high temperatures.

Delta (δ) Phase

The δ phase is a stable Ni_3Nb orthorhombic phase. δ can form due to processing and heat treatments as well as during service. δ is the stable form of the finer γ'' phase and forms at temperatures above 650 °C as needles or platelets. δ forms at grain boundaries and around Laves phase and inclusions. Transition of γ'' to δ causes strength degradation but has been found to reduce notch rupture sensitivity and thus is not an entirely detrimental phase [4:181]. The solvus temperature of δ in Inconel 718 is approximately 995 °C [4:184]. The presence of δ needles in overaged 718 have been found to increase plasticity and crack propagation resistance of the alloy through crack propagation guidance and interaction [13].

Eta (η) Phase

The η phase is a stable hexagonal close-packed (HCP) phase. η, like δ, can form during processing, heat treating, or during service and is the stable form of γ'.

Laves Phase

Laves phase is a highly detrimental, low melting point A_2B type eutectic phase where "A" refers to Fe, Cr, Si or Ni and "B" corresponds to Nb, Ti, or Mo. Laves phase forms at the end of the solidification sequence as a eutectic phase along grain boundaries in Microcast-X (MX) Inconel 718 and also in interdendritic regions in conventionally cast 718 [9, 14]. Laves phase depletes niobium which could otherwise be used to form γ'' strengthening precipitates and adds greatly to HAZ liquation cracking problems during welding. Mitchell (et al.) have quoted Laves phase as having a variable composition based around Ni35 Nb31 Fe13 Cr13 Mo7 Ti1 Si1 (wt%) [15].

Carbides

MC-type carbide and M(C,N) carbonitride precipitation occurs during primary solidification of the γ matrix, both within grains and along grain boundaries [9]. Carbides are an important precipitation strengthening mechanism and appear in cast 718 primarily as blocky niobium MC-type carbides (NbC). Titanium carbides (TiC) are also common but appear in far smaller numbers than NbC. The liquation of NbC has been identified as a strong contributor to the HAZ liquation cracking phenomenon in alloy 718 [16]. Carbides also serve for grain size control during heat treatments by pinning grain boundaries [9]. There have been no reports of $M_{23}C_6$-type carbides found in Inconel 718 [15].

Borides, Nitrides, and other minor phases (G, σ, and μ)

Several other minor phases are often found in Inconel 718 which are worthy of consideration. Borides appearing along HAZ microfissures in 718 have been suggested as a possible indication of boron segregating to grain boundaries and acting as a grain boundary melting point depressant and also promoting grain boundary wetting thus contributing to liquation cracking [17].

Nitrides, in particular TiN particles (1 - 10 μm in size), have been identified as appearing in the liquid melt prior to the start of solidification and act as nucleating sites for primary

carbide precipitation. Carbides are thus sometimes found to have nitride cores leading to the commonly used term "carbonitride" [15]. Nitrogen content and TiN precipitation has also been linked to microporosity formation in alloy 718 castings [18].

The formation of the minor phases G, σ, and μ is rare since nickel-iron alloys are not typically used at temperatures high enough to encourage precipitation of theses phases. Formation of sigma (σ) platelets can cause brittle fracture along the platelet-matrix interface and also general strength loss by depleting important strengthening elements. Little is known concerning the effects of μ, however, G, a complex cubic of nickel, titanium, and silicon, was found to decrease stress-rupture life in alloy A-286, another nickel base superalloy [4:182].

2.3.5 Microcast-X (MX) Investment Casting and The Solidification Process

Through careful control of casting parameters it is often possible to reach a desired cast microstructure and thereby literally cast strength into a near-net shape component requiring little to no additional machining. Investment casting is a complex process which is further complicated by the irregular shapes of sections which must be cast. The MX process is used to produce a homogeneous isotropic microstructure of consistent equiaxed (non-dendritic) fine grains of ASTM grain size 3 to 5 [19]. The MX investment casting technique is patented by Howmet and involves using a superheat which is typically within 11 °C above the liquidus and not more than 17 °C above the liquidus. This low superheat ensures rapid

solidification of the melt upon pouring with high heat extraction rate and lower thermal gradients. Turbulence in the molten metal and possible grain refiners in the melt which act as grain nucleation sites may aid in producing the final homogenous fine-grain microstructure but it is the low superheat which is primarily responsible for the fine grain size achieved in MX investment castings. The low superheat results in low fluidity of the liquid metal which in turn causes difficulty in filling thin sections. MX castings also require HIPing (hot isostatic pressing) due to limited feeding characteristics, however many conventional castings are also HIPed [7].

HIPing following casting is done to close residual porosity in the casting thereby producing nearly 100% dense castings. HIPing at or below 1120 °C is necessary to avoid grain growth [20]. A typical HIPing process is the application of 103 MPa (15 ksi) for 3 hours at 1120 °C (2050 °F) [7]. However, HIPing removes only internal porosity and not surface porosity. Microporosity is highly detrimental to stress rupture and fatigue properties of superalloy components [6].

HIPing typically causes a slight increase in grain size from the pre-HIPed grain size of ASTM #5 (65 μm) to a post-HIPed size of ASTM #4 (90 μm) [9]. Carbides and Laves phase present in the cast material act as pinning phases and thus aid in reducing excessive solid state grain growth during subsequent HIPing.

As solidification proceeds some solute elements, such as niobium, are rejected in front of the solid-liquid interface resulting in higher concentrations at the grain boundaries in the cast microstructure. The high concentration of these elements leads to the formation of precipitate phases such as γ'', δ, and Laves at the grain boundaries. High niobium concentrations in grain boundary regions in cast alloy 718 has also been found to cause localized increases in hardness which leads to increased tool wear and occasional catastrophic tool failure [5]

The solidification and precipitation sequence of Inconel 718 as determined through differential thermal analysis (DTA) of samples from ESR IN-718 ingots by Murata (et al.) is presented in Table 2-4 below. Temperatures are only approximate as many factors such as heat extraction rate and composition can greatly affect precipitation temperatures [21].

Solidification or Precipitation Reaction	Solidification and Precipitation Temperature [°C] (upon cooling)
Proeutectic γ reaction	~ 1360
γ + MC eutectic reaction	~ 1290
γ + Laves eutectic reaction	~ 1160
δ phase precipitation	~ 1145
γ'' and γ' precipitation reaction	~ 1000

2.4 Electron Beam Welding of Inconel 718

2.4.1 Introduction

High-vacuum electron beam welding (EBW) owes its popularity to the fact that it is capable of producing very high purity, high quality welds with relatively small heat affected zones. One drawback however is that large parts require a large vacuum chamber. The following discussion will describe some of the basic principles of EB welding and general characteristics of weld solidification.

2.4.2 Basic Principles

Electron beam welding involves the application of a collimated high-energy beam of electrons to the surface of the specimen to be welded. Electrons are accelerated to velocities of 0.3 to 0.7 times the speed of light via an electron gun with an accelerating potential of 25 to 200 kV [22]. The kinetic energy of the electrons is converted into thermal energy as they impact with the surface of the workpiece. The high energy density beam causes instantaneous local melting of the weld material [22]. The high vacuum is required to produce high purity welds and also to avoid scattering of the beam electrons via collisions with O_2 and N_2 molecules in the beam path.

A typical triode style electron gun consists of a cathode/grid/anode configuration where the cathode is a heated electron source (emitter) maintained at a high negative potential. The grid cup is a carefully designed electrode which can be held at a negative bias with respect to the cathode. The anode is an electrode held at ground potential through which the electrons pass as they are drawn from the emitter. Typical emitting material is tungsten (W) or tantalum (Ta) with an emitting temperature of about 2480 °C (4500 °F). After passing through the anode the electrons are focused into an narrow high-energy beam by an electromagnetic focusing coil. The electron gun assembly is always maintained in high vacuum in order to protect the gun components from impurity contamination and oxidation [22].

2.4.3 Weld Solidification and Residual Stress

Fusion welds solidify via epitaxial solidification in which a solid embryo nucleates on the solid surface of the melted back base metal. Epitaxial solidification is thus a heterogeneous process in which the wetting angle, ψ, of the spherical embryo cap relative to the original solid-liquid interface depends upon a balance of forces produced by the interfacial energies. This balance of forces depicted in Figure 2-1 is described by equation (2.1) and (2.2) where γ_{SL} is the solid-liquid surface energy, γ_{SM} is the solid weld metal-base metal surface energy, and γ_{ML} is the base metal-liquid surface energy.

$$\gamma_{ML} = \gamma_{SM} + \gamma_{SL} \cos \psi \quad (2.1)$$

$$\cos \psi = (\gamma_{ML} - \gamma_{SM}) / \gamma_{SL} \quad (2.2)$$

The approximations $\gamma_{SM} \approx 0$ and $\gamma_{ML} \approx \gamma_{SL}$ can be used since solidification is epitaxial and the composition of the weld metal and base metal are commonly very similar. This results in a wetting angle of $\psi \approx 0$ indicating that there is virtually no energy barrier to solidification and thus no undercooling is needed and solidification proceeds uniformly over the entire solid-liquid interface area of the base metal grain. The initial crystal size of the solidifying weld metal will often correspond to the base metal HAZ grain size which can be considerably large in some instances. Thus the coarseness of the resulting weld metal structure may be affected by the HAZ grain size.

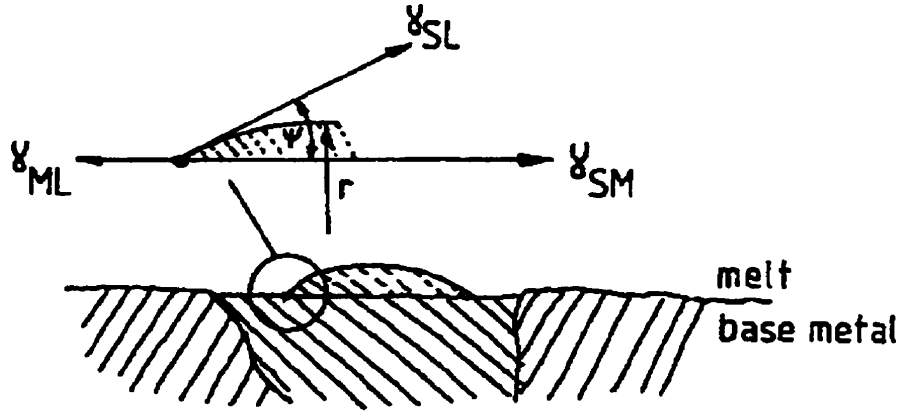

Figure 2-1: Heterogeneous nucleation of solid weld metal embryo at fusion boundary [23:67]

Weld solidification is a rapid non-equilibrium solidification process. If it is assumed that no diffusion occurs in the solid, which is commonly considered a good assumption [23:71], then a favourably oriented crystal will grow under two different general cases namely; (1) perfect mixing in the liquid and (2) diffusional mixing in the liquid.

Weld solidification is considered to be a combination of both of these mechanisms beginning with good mixing at the initial stages and moving towards diffusional mixing as solidification proceeds. In either case, solute is rejected in front of the advancing interface which leads to a solute rich centerline which may be susceptible to hot cracking problems.

Cellular and Dendritic Solidification

As solidification proceeds, the liquid ahead of the solid-liquid interface develops a build-up in solute concentration . If the new equilibrium solidification temperature, T_E , of the solute enriched liquid at some point just ahead of the interface is above the actual temperature in the melt, T_L , as shown in Figure 2-2 , then the liquid is said to be constitutionally supercooled. Constitutional supercooling results in the formation and rapid growth of nodules from the advancing interface since the tip of the growing nodule may still be below the liquidus temperature.

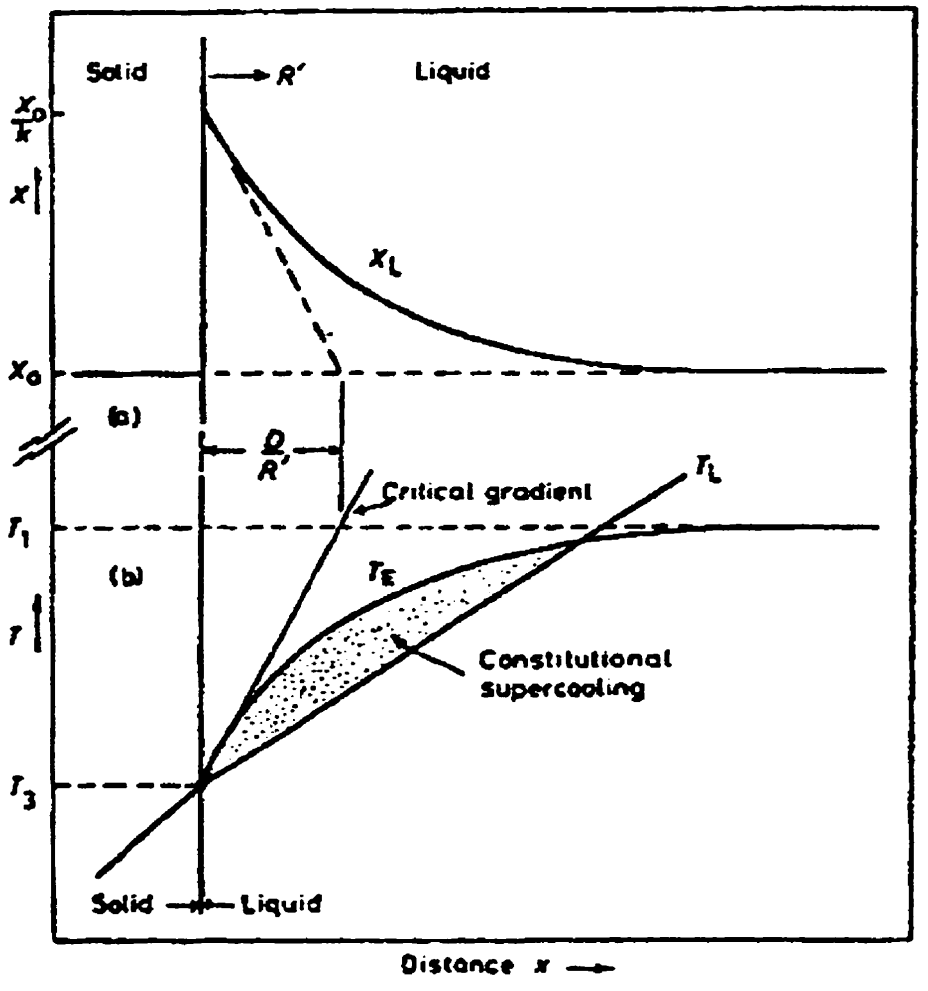

Figure 2-2: Constitutional supercooling resulting from solute enrichment of the liquid ahead of the advancing solid-liquid interface [23:77].

As a nodule grows it rejects solute to either side thereby lowering the solidification temperature even further at its root causing other protrusions to form which eventually grow into a set of long, virtually parallel cells. Rejected solute will be concentrated between cell walls. Secondary arms, and even tertiary arms, may develop and form along the primary cell walls and grow outward in the same manner as the primary cells grew from the planar interface. The cells are then considered to be dendrites. The cellular to dendritic transition depends upon cooling rates, cell spacing, and solute levels. It has been observed that higher cooling rates tend to decrease cell and dendrite arm spacing since higher cooling rates decrease the time available for rejected solute to diffuse laterally.

Residual Stresses

Thermal stresses generated in the weld and the surrounding material change as welding proceeds. As shown in Figure 2-3, there remains a high tensile and compressive residual stress in the base material to either side of the weld. The shape of the weld cross-section will also affect the residual stress levels around the weld due to different heat flow patterns [23:38]. It is these stresses generated during the welding thermal cycle which enable HAZ microfissuring to occur.

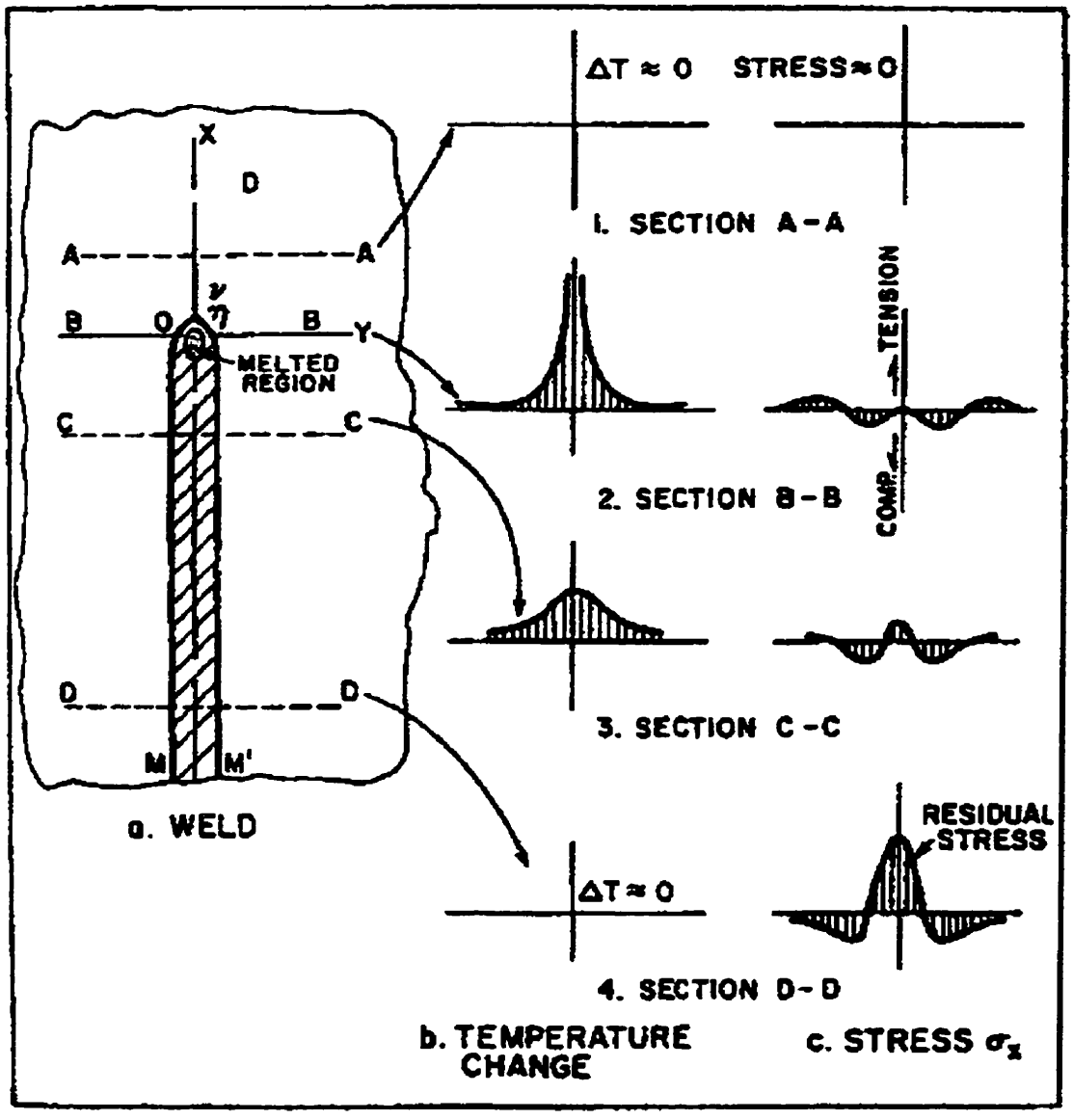

Figure 2-3: Schematic representation of changes in stress with temperature during the welding cycle [23:39].

2.4.4 Effect of Welding Parameters

Several general parameters can be controlled in EB welding in order to produce the desired weld. These parameters include accelerating voltage, beam current, beam focus, working distance, and welding speed (travel speed). Increasing accelerating voltage or beam current will increase depth of penetration by increasing the energy density of the beam. A sharper beam focus with a decreased beam spot size on the workpiece surface will decrease the EB weld head width and increase the depth of penetration while a slightly de-focused beam (larger spot size) would produce a wider weld head with less penetration. Increasing welding speed will decrease the heat input per unit length and will thus decrease the overall cross-sectional size and heat input of the weld.

2.5 Elemental Segregation Theory

2.5.1 Introduction

Segregation of solute atoms to grain boundaries which occurs during solidification, heat treating, hot working, and welding is an extremely important consideration in studying microfissuring since HAZ microfissuring in Inconel 718 is predominantly intergranular. Solute atoms residing at the grain boundaries at the time of welding may greatly affect the weldability of the alloy. As previously discussed, niobium resides in higher concentrations at

the grain boundaries due to solidification behaviour and, due to the relative immobility of Nb in the gamma matrix during heat treatments. As a result, it is available to form lower melting point phases such as Laves which can lead to liquid film formation in intergranular regions. Other trace or impurity elements may lead to the formaiton of secondary phase grain boundary films which will promote liquation cracking, however, the presence of such films is not necessary and it has been shown that high concentrations of impurity atoms residing at the grain boundaries may promote cracking without secondary phase formation [24:84]. Grain boundary segregation of trace elements has been found to occur via two primary mechanisms; namely equilibrium and non-equilibrium segregation.

2.5.2 Equilibrium Segregation

Equilibrium segregation occurs when a material is exposed to elevated temperatures for a period of time which is sufficient to promote significant diffusion of solute atoms to energetically favorable locations in the matrix [25]. The interfacial free energy of the loosely packed grain boundary regions is thus reduced by the absorption of segregating impurity elements.

In 1957, McLean developed a quantitative model for the equilibrium concentration of solute atoms at grain boundaries [25]. McLean's assumptions were;

(i) only one segregating element is present

(ii) only one type of boundary site exists

(iii) there exists no site-to-site interactions

With these assumptions McLean formulated the following expression for the grain boundary concentration of segregating atoms (C_b) in atomic fractions;

$$C_b / (C_{bO} - C_b) = \{C_m / (1-C_m)\} \exp (E / kT)$$

Where C_{bO} is the saturation value of C_b, C_m the matrix concentration of the segregant, and E the binding energy at the grain boundary. Since C_{bO} is typically about one monolayer and C_m is of the order 10^{-4} we can approximate the above equation as;

$$C_b / (1 - C_b) = C_m \exp (E / kT)$$

McLean went on to formulate more extensive equations considering the time dependence of segregation which are outlined in Huang's work [24] and are not repeated here.

2.5.3 Non-equilibrium Segregation

Non-equilibrium segregation occurs during cooling from high temperatures. Non-equilibrium segregation was first observed by Westbrook who discovered a significant grain boundary hardening in quenched alloys which could not be fully explained by equilibrium segregation theories and suggested that another mechanism was operating. Non-equilibrium segregation occurs via diffusion of vacancy-solute atom complexes down vacancy gradients toward vacancy sinks such as grain boundaries and free surfaces [25]. As the temperature decreases, a vacancy gradient is formed due to a corresponding decrease in equilibrium vacancy (and complex) concentration levels. The vacancy gradient creates a net flow of vacancies and vacancy-impurity complexes toward vacancy sinks. The degree of non-equilibrium segregation depends upon;

(i) the heat treatment temperature and cooling rate

(ii) the concentration of solute atoms

(iii) the vacancy-solute atom binding energy

The existence of non-equilibrium as a strong segregation mechanism has been well established in various studies using such techniques as boron particle tracking autoradiography, secondary ion mass spectroscopy (SIMS), electron microprobe analysis (EMPA) for Zn, Cu, Ge, and Al, and scanning transmission electron microscopy with energy dispersive spectrometry (STEM/EDS) for Ti and Cr [26]. As heat treatment temperature

increases the magnitude of non-equilibrium segregation will also increase for a given vacancy-binding energy and cooling rate as shown in Fig. 2-4 [24:102].

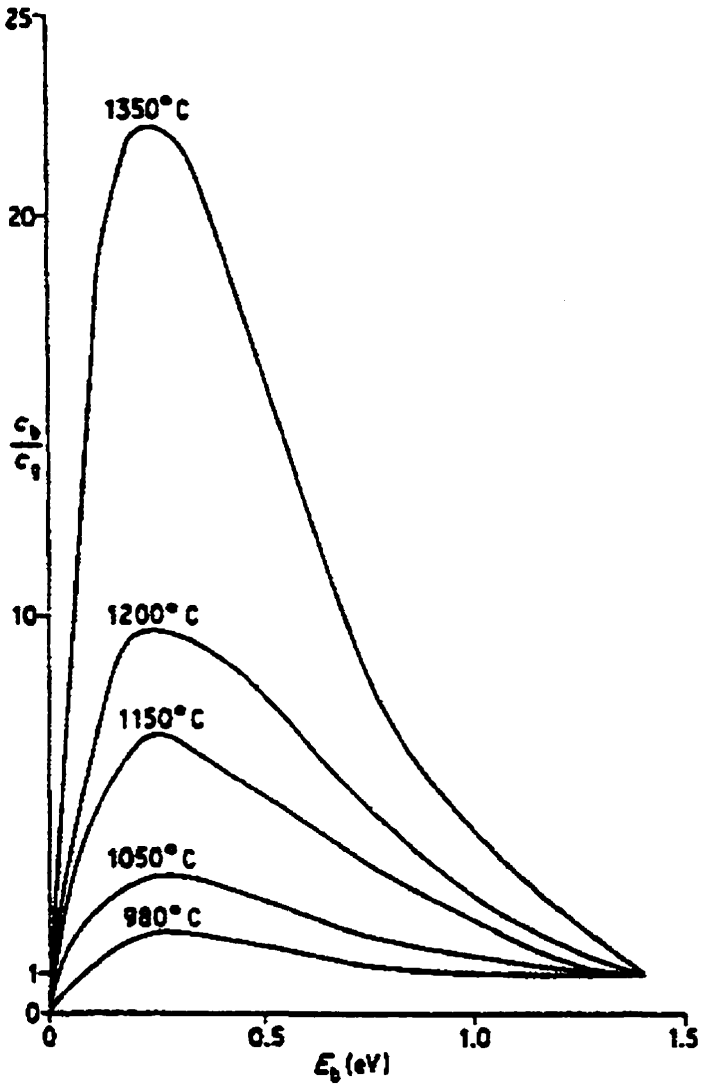

Figure 2-4: Effect of vacancy-impurity binding energy (E_b) on the degree of non-equilibrium segregation (C_b/C_g) on cooling to 750°C from different heat treatment temperatures [24:102].

2.5.4 Boron Segregation

Boron segregation has been the subject of many investigations and in particular Karlsson's extensive work on boron segregation in austenitic stainless steel has proven very revealing. Due to the fact that the atomic diameter of boron is larger than typical interstitials like carbon and nitrogen but is still smaller than substitutional elements such as niobium and chromium, the migration of boron to loosely packed interfaces should be energetically favourable.

It is also known that, as the heat treatment temperature increases, the degree of equilibrium segregation decreases and the degree of non-equilibrium segregation increases [26] as shown in Figure 2-5. However the degree of non-equilibrium segregation of boron in austenite was found to be strongly dependent on cooling rate and thus the slope of the non-equilibrium curve in Figure 2-5 will depend upon the cooling rate.

Karlsson analyzed boron segregation for different cooling rates from different heat treatment temperatures and discovered that the highest degree of non-equilibrium segregation of boron to grain boundaries occurred for the highest heat treatment temperature and for an intermediate cooling rate of 13 °C/s. This cooling rate dependence was also found in other experiments on low and high alloy steels. Karlsson also noted that non-equilibrium segregation was still detected when cooling from high temperatures at high cooling rates (530 °C/s water quench). Thus it was concluded that at high heat treatment temperatures, non-equilibrium segregation is the dominant segregation mechanism for boron in austenite.

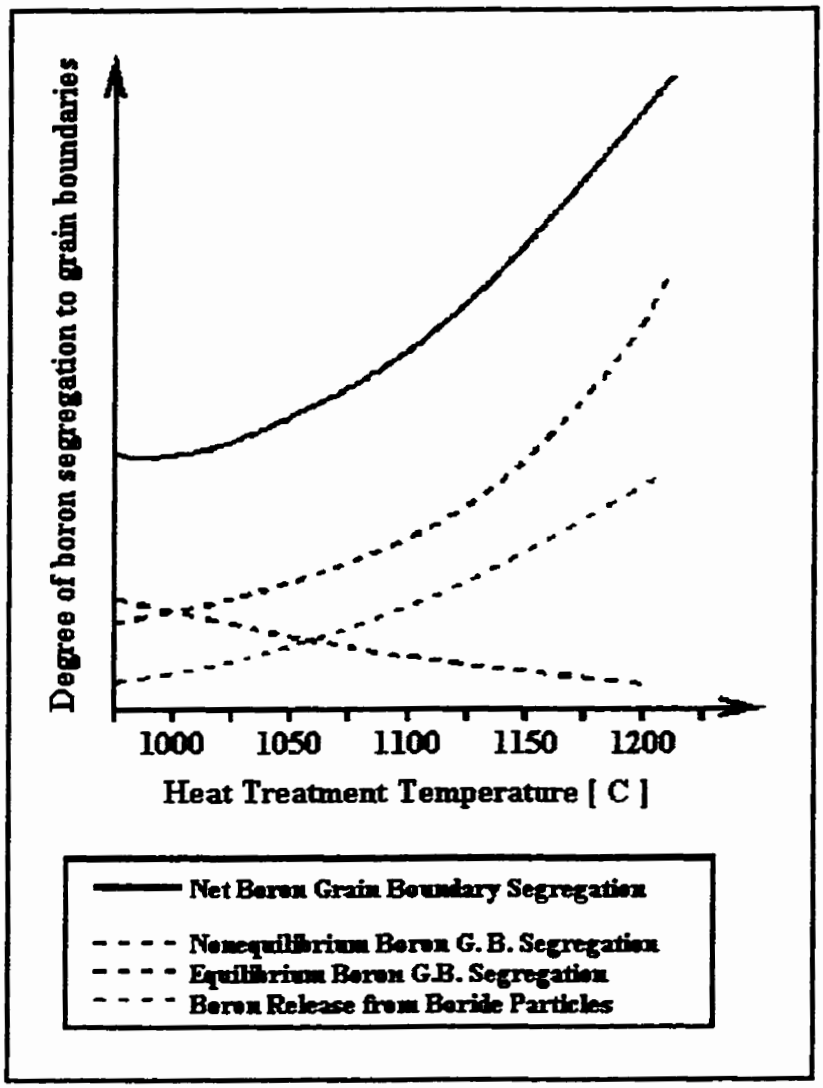

Figure 2-5: Schematic representation of boron grain boundary segregation after cooling from different heat treatment temperatures.

Special boundaries such as coherent twin boundaries are not efficient vacancy sinks like general grain boundaries. As a result, no boron was found on coherent twin boundaries. Karlsson also found little difference in the amount of segregation to high and low angle grain boundaries. It has been estimated that the binding energy of boron to austenite grain boundaries is about 0.4 to 0.6 eV

Huang also discovered a significant amount of non-equilibrium segregation of boron in cast 718 specimens air cooled from 1163 °C but did not detect appreciable boron segregation in specimens water quenched from 1163 °C [27]. A recent study detected very strong segregation of boron to grain boundaries in wrought Inconel 718 specimens which were air-cooled from different heat treatment temperatures [28]. Horton (et al.) recently confirmed boron segregation to grain boundaries and did not find segregation of boron to γ-γ'' interfaces [11].

2.5.5 Segregation of Other Trace Elements

Phosphorus has recently been shown to segregate to grain boundaries in heat treated 718 and it has been suggested that P co-segregates with Mo. The result of phosphorus segregation to grain boundaries has been suggested to result in higher stress rupture life due to a decrease in grain boundary binding energy accompanied by an increase in grain boundary cohesive force [29]. Horton also found phosphorus and carbon to segregate to grain boundaries and

suggested that an increase in stress rupture life due to boron and phosphorus additions may be the result of the elements affecting dislocation mobility by some pinning mechanism [11]. Guo (et al.) found phosphorus segregation to grain boundaries decreases δ nucleation and growth [8]. Guo (et al.) also found Si to segregate strongly to grain boundaries.

Mulford demonstrated equilibrium segregation of S in Ni and binary alloys with Cu, Al, Cr, Mo, W, and Hf and did not detect co-segregation effects between sulfur and the other elements [30]. Mulford considered the experimental results to agree well with the theoretical model of McLean for equilibrium segregation. Thompson also found sulfur segregation to grain boundaries in Ni [31].

2.6 Mechanisms of HAZ Microfissuring

2.6.1 Introduction

Investigations into the nature of heat-affected zone (HAZ) microfissuring in Alloy 718 have pointed to the liquation of Laves and primary carbides as the main contributing factors in intergranular HAZ liquation cracking [16,32]. However many other factors have been found to contribute to the HAZ microfissuring phenomenon. Such factors as processing, welding parameters, pre-weld heat treatments and grain size can create microstructural conditions which favour certain microfissuring mechanisms. These HAZ microfissuring mechanisms

include grain boundary liquation and wetting, grain boundary sliding and weld metal backfilling. Elemental segregation of trace elements to grain boundaries has recently been found to be a major concern in HAZ microfissuring analysis as it appears that trace elements such as boron in high concentrations at grain boundaries may reduce the grain boundary melting point and thus encourage HAZ grain boundary melting during welding without the need of a secondary phase film to be present.

2.6.2 Intergranular Liquation Cracking in HAZ

During the welding cycle, secondary phases such as carbides and Laves phase in the HAZ may liquate at the grain boundaries. This liquid may then travel along the grain boundary through grain boundary wetting. If this liquid is produced and is capable of wetting the grain boundaries and thus producing a continuous liquid film along HAZ grain boundaries the alloy would become highly susceptible to liquation cracking. Liquation cracking will occur as this liquid solidifies into a weak, brittle intermetallic phase which cannot withstand the thermal stresses present in the HAZ. Grain boundary sliding is also a common phenomenon leading to liquation cracking since the wetted grain boundaries are free to slide relative to one another. Upon cooling the stresses created by this movement are sufficient to cause separation of the grain boundaries, thus forming intergranular cracks. Thompson found that niobium carbides did not reprecipitate from grain boundary liquid and the intergranular liquid acted as a pseudo-binary of gamma and Laves phase [16]. Thompson also suggests that

grain boundary migration during elevated heat treatments may cause grain boundaries to intercept carbides which will increase the amount of carbides present at the grain boundaries and available for formation of grain boundary liquid.

It has been suggested that boron is a major contributor to liquation cracking as it may be responsible for allowing the grain boundary wetting phenomenon to take place when grain boundary liquid is present [14,16] and act as a grain boundary melting point suppressant [17].

2.6.3 Effect of Alloying Elements and Secondary Phases on Weldability

As previously discussed, Inconel 718 is a highly alloyed nickel-iron-based superalloy in which each alloying addition plays a particular role. Some of these alloying additions, however, affect the weldability of the alloy. Table 2-5 below lists the general degree of influence of different alloying elements on weldability of nickel-base superalloys [14]. Niobium is considered beneficial because it allows γ'' strengthening to occur as opposed to γ' and thus avoids the stain age cracking problem. However, as discussed earlier, niobium carbides and Laves phase lead to liquation HAZ cracking problems.

High boron content was found by Kelly to be a major contributing factor to HAZ microfissuring in cast 718 [14]. Kelly discovered that liquated Laves phase in the HAZ immediately wet the grain boundaries in high boron 718 (100ppm) but melted in situ in the

non-boron heat. Vincent suggested that boron is the most likely segregant which acts as a melting point depressant with possible synergistic effects from other trace elements [17].

Kelly found that high iron and low silicon were detrimental to weldability. Kelly theorized that this is due to the fact that iron promotes Laves phase formation and lowering silicon content causes carbide morphology to change from blocky to script where the more angular script carbides will act as crack initiation sites. Niobium content seemed to have variable effects depending on heat treatment but no explanation for this behaviour was found and thus niobium is considered to simply be a source for low melting point phases such as Laves phase and not directly beneficial or detrimental to weldability. Kelly's work also showed that higher sulfur contents had no detrimental effects on weldability whereas the effect of phosphorous on weldability was unclear. Hafnium and zirconium did not seem to affect weldability.

Beneficial	No Effect	Variable	Harmful
Niobium	Manganese	Aluminum	Lead (Pb)
Magnesium	Copper	Titanium	Sulfur (S)
	Chromium	Carbon	Phosphorus (P)
	Iron	Molybdenum	Zirconium (Zr)
	Cobalt	Silicon	Boron (B)

Kelly found that carbon content had no effect on weldability however the more extensive work done by Thompson (et al.) showed a definite increase in liquation cracking with increasing carbon (and thus carbide) content in cast 718 [16].

2.6.4 Effect of Pre-Weld Heat Treatments on Weldability

The purpose of pre-weld heat treatments is primarily to cause as much of the secondary phases present in the alloy to go into solution so as to avoid their interference with the welding process. Strengthening phases must be dissolved to avoid cracking tendencies due to internally generated stresses which occur during the welding cycle and other detrimental phases, such as Laves phase, must be dissolved in order to reduce the risk of HAZ liquation cracking. It is important to note however that the relatively large atomic radius of niobium atoms greatly reduces their mobility and thus they will remain highly concentrated in the grain boundary regions when a cast component is heat treated [14]. This relative immobility of niobium atoms allows them to be readily available to re-form Laves and other phases at the grain boundaries during the welding cycle, during subsequent heat treating, or in service.

Vincent suggested that higher solution temperatures should enhance segregation of grain boundary melting point depressants such as boron and hence increase liquation cracking at HAZ grain boundaries [17]. Valdez and Steinman found liquation cracking to increase as solution heat treatment temperature increased above 1950 °F (1066 °C) [16]. High

temperature heat treatments as well as heat treatments of extended times can also cause grain growth and grain boundary migration since Laves phase and possibly other minor phases which may act as pinning phases and impede grain growth have gone into solution [9]. Laves phase is typically completely dissolved into the matrix from solution and homogenization heat treatments whereas these heat treatments have little effect on carbide content and morphology [15]. The typical homogenization and solution anneal heat treatments for Inconel 718 are { 2000 °F (1093 °C) / 1 hour } and {1700 °F (927 °C) / 1 hour / air cool } respectively [16]. This solution heat treatment often leads to the formation of intergranular δ needles which, as Vincent has theorized, actually decreases microfissuring susceptibility in wrought 718 [24:61]. A large volume fraction of δ-phase was found, via hot ductility testing, by Mehl and Lippold to decrease repair weldability of cast alloy 718 [33]. Mehl and Lippold found that liquation cracking susceptibility of δ-phase embrittled 718 was greatly reduced when a pre-weld solution heat treatment temperature of 1038 °C was used which dissolved much of the δ-phase. A 927 °C pre-weld heat treatment had no effect on hot ductility behaviour of the alloy.

Solution heat treating above 1000 °C will maintain the "cleaner" microstructure produced through homogenization heat treatments. Age hardening heat treatments are performed at 1200 °F (649 °C). Table 2-6 below provides the various temperature ranges over which different phases form during heat treating and cooling (or perhaps exceedingly high service temperatures) and to what temperature they remain stable when present [24]. This table indicates that carbides as well as nitrides and borides will not be greatly affected by heat

treatments which are normally conducted at or below 1200 °C but homogenization heat treatment temperatures approaching 1200 °C will be useful in dissolving Laves and delta phases [34]. Homogenization heat treatments are followed by rapid (water) quenching to avoid or minimize re-precipitation of these phases.

Precipitate Phase	Temperature of Formation [°C]	Stability Temperature [°C]
Laves	~ 1167	~ 1175
Carbides	upon solidification	~ 1235
Delta (δ)	~ 843 to 995	~ 1010 (wrought)
Gamma Dbl. Prime (γ'')	~ 712 to 899	~ 677
Gamma Prime (γ')	~ 637 to 718	na
Borides and Nitrides	upon solidification	~ 1225 to 1290

2.6.5 Elemental Segregation Effects

Among the numerous studies of elemental segregation in alloy 718 and other nickel-base superalloys some have also considered the effect of elemental segregation on microfissuring susceptibility. Kelly reported a 31% increase in total crack length (TCL) when increasing the heat treatment from 1093°C /1h to 1163 °C HIP + 1093°C /1h in cast 718 [14]. Huang suggested a direct correlation between heat treatment temperature, degree of boron

segregation, and total crack length in specimens of conventionally cast 718 heat treated at different temperatures though the results were not fully conclusive since the study was not designed specifically to answer this question [27].

A recent work by Chen (et al.) demonstrated a direct correlation between cooling rates, boron content, and microfissuring susceptibility [28]. Chen (et al.) found that boron segregation to grain boundaries increased in high boron wrought 718 as compared to the same alloy with low boron content and also that boron segregation was much stronger in air cooled specimens as compared to water quenched. Finally, Chen (et al.) discovered that microfissuring was greatest where boron segregation was greatest and lowest for the condition of least boron segregation. This suggests that HAZ microfissuring susceptibility in Inconel 718 may be directly affected by boron concentration levels at the grain boundaries.

2.6.6 Grain Size Effect

It has been established that microfissuring in wrought alloy 718 is linearly dependent on grain size and that wrought material is generally more resistant to microfissuring than conventionally cast material which has a very large grain size (typically 2 to 10 mm) [35]. Thompson (et al.) suggested that a larger grain size allows for increased volume fraction of intergranular liquid in the HAZ grain boundaries which could affect the temperature range and time that is available for the liquid to wet the grain boundaries and thus result in more

extensive grain boundary sliding. Thompson also theorized that the longer distance between triple points, and hence an increased interface sliding length, in a larger grain size material increases the strains experienced at grain boundary triple points and thus raises the potential for crack initiation at triple points.

2.6.7 Effect of Welding Parameters on HAZ Microfissuring

As previously mentioned, changes in EB welding parameters affect the weld shape and total heat input per unit length. Changing welding parameters has also been found to affect HAZ microfissuring in several studies. Huang discovered a correlation between cracking index (C.I.) and weld travel speed in conventionally cast 718 given by;

$$C.I. = 0.095 + 0.0068(\text{speed})$$

where travel speed is in cm/min and C.I. is in cm/cm^2 [24]. Other work on Incoloy 903 resulted in the following equation;

$$C.I. = 0.000394\ SPD - 0.0034\ A - 0.0027\ V + 0.013\ (P/W_{MID}) + 0.00016\ WD$$

where SPD is welding speed [mm/min], A is welding current [mA], V is accelerating voltage [kV], P is depth of penetration, W_{MID} is middle weld width, and WD is working distance.

The overall result is that increasing current and welding speed may maintain the same heat input per unit length, however, the material is subjected to higher thermal gradients. As their is less time for preheating in front of the weld and faster cooling behind the weld, the stresses generated will be greater and thus are likely to aggravate HAZ microfissuring.

Modifying welding parameters to alter the transverse weld profile has also been found to affect microfissuring susceptibility. Boucher (et al.) found that microfissuring was eliminated at weld head width (max) to weld height (penetration) ratios above 1.6. Increasing welding speed has been found to decrease this ratio and thus aggravate HAZ cracking by changing the weld profile which may lead to stress increases in high stress HAZ areas such as under the shoulder of the weld [36].

2.7 Scope of The Investigation

Several key points from literature must be noted in order establish the purpose and scope of the study undertaken herein. One primary consideration is the fact that the MXcast microstructure is a unique cast structure which has been recently introduced into actual production components however weldability studies have yet to be done on this alloy. It has been shown that boron segregation to grain boundaries has been the subject of recent concern regarding its potentially detrimental effects on weldability of Inconel 718 in general. Furthermore, electron beam (EB) welding produces consistent high quality welds and enables

careful control of the welding parameters and thus introduces less outside error than other welding techniques such as TIG welding (Tungsten Inert-Gas). Finally, it has been noted that secondary phases such as Laves phase, γ'' and δ phase can greatly affect weldability of alloy 718 and thus these must be removed through pre-weld solution heat treatment.

In considering these known factors and what is yet unknown a focused study on the MXcast alloy was developed. The primary purpose of the investigation was to study the effect of different pre-weld heat treatments on the electron beam (EB) weldability of the MXcast IN-718 alloy and to characterize the microstructure of the material both in as-cast condition and after heat treating at various temperatures and times. This primary objective entailed several components which needed to be studied. Material characterization included the measurement of grain size and volume fraction of secondary phases through optical image analysis as well as morphological and crystallographic observations on SEM and TEM as well as compositional analysis via EDS (SEM and TEM). Heat treatment development involved devising an optimal homogenization heat treatment which dissolved most of the secondary phases while maintaining the fine grain size of the alloy and solution heat treatments which varied boron segregation levels while maintaining the homogenized structure and enabling theoretical equilibrium segregation levels of sulfur to be acheived.

EB weldability was evaluated in terms of actual HAZ microfissuring observations and quantification in heat treated samples through crack length measurement and SEM/EDS analysis. The study also considered segregation mechanisms and effects of elemental boron

and sulfur and the relationships between elemental segregation, heat treatment temperatures and times, cooling rates, secondary phase interactions, grain orientations and HAZ microfissuring. Welding parameters and grain size were maintained constant throughout the study and all experimental procedures were consistent both within the study and with conventional practices.

CHAPTER THREE

EXPERIMENTAL PROCEDURES

3.1 Material

Tables 3-1 and 3-2 provide the composition and mechanical properties of the MX 718 alloy used in this study and provided by Howmet corporation. The as-received MXcast (and HIPed) plates were 14.6 cm x 20.5 cm (not including end risers) of approximately 16 mm thickness with risers on each end as shown in Figure 3-1.

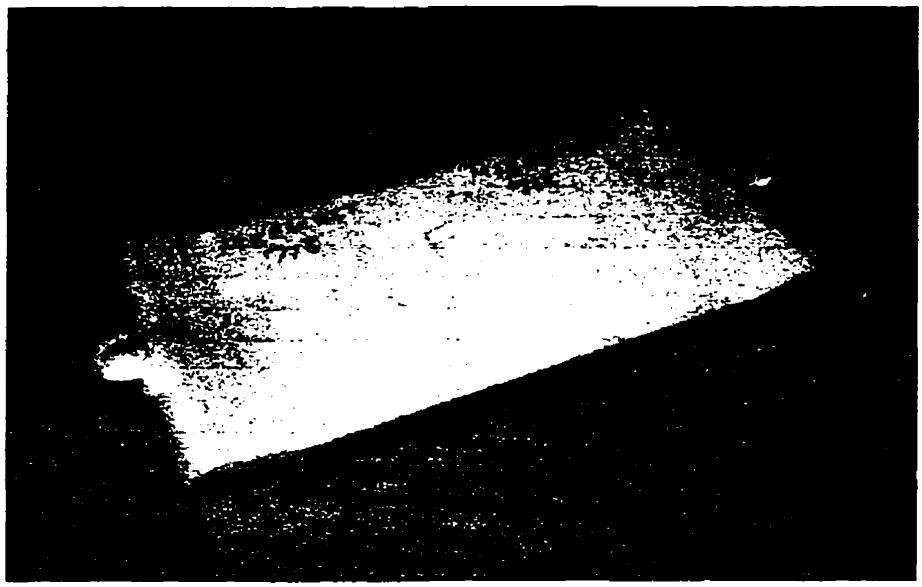

Figure 3-1: As-received Microcast-X Inconel 718 plate.

Table 3-1: Chemical Composition of Microcast Inconel 718 as provided by Howmet Corporation (wt%)			
Nickel (Ni)	52.81	Silicon (Si)	0.02
Chromium (Cr)	18.85	Manganese (Mn)	< 0.1
Iron (Fe)	Bal. (18.88)	Zirconium (Zr)	0.01
Niobium (Nb)	4.84	Copper (Cu)	0.01
Molybdenum (Mo)	3.04	Boron (B)	0.004
Titanium (Ti)	0.90	Phosphorus (P)	0.003
Aluminum (Al)	0.48	Sulfur (S)	0.001
Cobalt (Co)	0.10	Magnesium (Mg)	0.001
Carbon (C)	0.04	Silver (Ag)	< 5ppm

Table 3-2: Room Temperature Mechanical Properties of As-Cast (and HIP'd) Microcast Inconel 718 as provided by Howmet Corporation			
Tensile Strength [MPa (ksi)]	**1240 (179.9)**	**Elongation [%]**	**19.1**
Yield Strength [MPa (ksi)] (0.2% offset)	**1071 (155.3)**	**R.A. [%]**	**20.7**

3.2 Cooling Rate Tests

Cooling rate tests were performed on a test piece of cross section and length equivalent to the weld specimen sizes used in the electron-beam welding analysis. The cooling rate test involved the use of an implanted thermocouple lead at the approximate center of the specimen and an external thermocouple located on the outer surface adjacent to the internal thermocouple lead as shown in Figure 3-2. Data was recorded using a Omegaline 600A

plotter connected through two Omega digital thermocouple temperature controller displays and thermocouple leads. Specimens were quenched in an ice-brine mixture for water quenching results and cooled in front of an electric fan for air cooling rates.

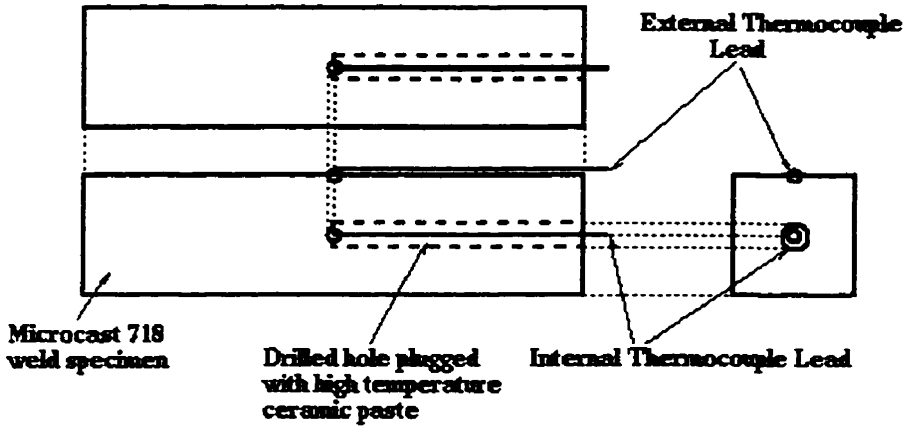

Figure 3-2: Cooling test specimen schematic

3.3 Heat Treatments

Preliminary Homogenization Heat Treatments

Extensive preliminary heat treatments were conducted on the as-received material to first establish the effect of different homogenization heat treatment temperatures and times on the microstructure of the alloy. These heat treatments were done at 1150, 1175, and 1200 °C for different times as shown in Table 3-3 followed by water quenching in each case. All heat

treatments were done in a cylindrical tube furnace, as shown in Figure 3-3, with specimens sealed in Corning Laboratory Glassware high temperature quartz glass which was first evacuated to at least $1x10^{-5}$ torr then filled with Argon to a pressure of approximately 150 mmHg prior to sealing with an oxy-acetylene torch. Encapsulating specimens prior to heat treatment greatly reduced oxidation of the specimens.

Table 3-3: Preliminary Homogenization Heat Treatments

Temperature [°C]	Heat Treatment Times [Hours]
1150	4.0, 15.0
1175	5.0, 10.0, 15.0, 20.0
1200	1.0, 2.0, 2.5, 4.0 15.0, 24.0
1250	0.5

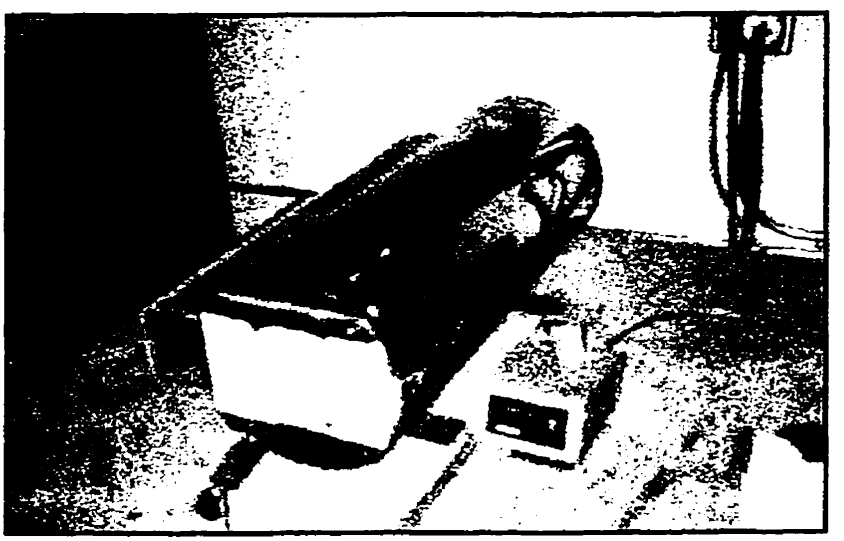

Figure 3-3: Heat treating furnace for all MX IN-718 specimens

After careful consideration of the results along with some experimentation with slow heating to prevent constitutional liquation of Laves phase, it was found that the optimum homogenization heat treatment to be used in further studies was; slow heating from 1000 °C to 1200 °C over 70 minutes and a 30-minute hold time at 1200 °C, followed by water quenching in ice-brine. This primary heat treatment will be hitherto referred to as "H" in designated heat treatments.

Solution Heat Treatments

Solution heat treatment times were calculated using a diffusion distance of 100 μm for boron and sulfur diffusion using equation (3). Table 3-4 summarizes the calculated results and Table 3-5 provides the final solution heat treatments. Each sample was given the primary homogenization heat treatment, H, followed by a designated solution heat treatment as per Table 3-5. Theoretical elemental diffusion rates were calculated as follows [26:10];

$$\text{Boron:} \quad D = (2.0 \times 10^{-7}) \exp[-0.97 / kT] \qquad (1)$$

$$\text{Sulfur:} \quad D = (4.6 \times 10^{-5}) \exp[-213.6 / RT] \qquad (2)$$

where:

D: diffusion coefficient [m^2/s]

T: heat treatment temperature [K]

$k = 8.617 \times 10^{-5}$ [eV/K]

$R = 8.315 \times 10^{-3}$ [kJ/mol K]

The time needed to reach equilibrium segregation for a given temperature, T, and a given grain size diameter, d, was calculated by:

$$t = d^2/D \qquad (3)$$

Temperature [°C]	Boron [sec.]	Sulfur [hrs.]
1000	162.3	28.4
1050	118.6	13.3
1100	88.7	6.5
1150	67.7	3.4
1200	52.6	1.8

Temperature [°C]	Heat Treatment Time [Hours]	Cooling Method
1000	30	WQ and AC*
1050	14	WQ and AC*
1100	8	WQ and AC*
1150	5	WQ and AC*
1200	2	WQ and AC*

*WQ = Water Quenching and AC = Air Cooling

The 1000 °C and 1200 °C solution heat treatments were eliminated because the 1200 °C heat treatment would produce grain growth and the 1000 °C heat treatment produced δ needles as discussed later. Thus six different heat treated conditions were further analyzed. These are designated; H+S1050AC, H+S1100AC, H+S1150AC, H+S1050WQ, H+S1100WQ, and H+S1150WQ with S referring to solution heat treatment, and 1050, 1100 and 1150 the heat treatment temperature in °C and AC and WQ refer to air cooling and water quenching respectively.

3.4 Sample Preparation

3.4.1 Metallographic Examination

Samples for metallographic examination (both optical metallography and SEM) were almost always sectioned from blocks of heat treated or as-cast material using a LECO CM-24A cutoff machine with LECO 811-975-010 (also 976 and 978) friction disks. The Inconel 718 specimens were found to be exceedingly difficult to cut using a diamond saw as the blade edge dulled very quickly and so required repetitive sharpening. Some sectioning was also accomplished using a Agemespark F400 EDM wire cutting machine as later discussed for thin foil specimen preparation. Samples were then mounted in thermosetting bakelite resin using a standard Buehler Simplimet II mounting press. Heating and cooling times of approximately 15 minutes each and a pressure of 5 ksi ensured a good mount. Specimens were then polished mechanically using abrasive SiC papers on grinding wheels and a hand grinder table from 80 to 600 grit followed by diamond polishing on polishing wheels typically up to 1 μm diamond slurry and even LINDE B alumina abrasive when needed for high magnification observations and optical metallography. Although several etchants were attempted it was found that a slightly stronger variation of Kalling's No.2 swab etchant (100 mL Ethanol, 100 mL HCl, 5 g of $CuCl_2$) produced the best results.

Optical micrographs were produced using a Nikon FX-35A 35 mm camera mounted on a Nikon EPIPHOT-TME inverted optical microscope, as shown in Figure 3-5, with black and

white ASA 125 film. Film and prints were developed using Kodak developing and fixer solutions. SEM micrographs were produced using Polaroid Professional 53 coaterless 4"x5" ISO 800/30° instant sheet film.

3.4.2 Carbon Extraction Replicas

Carbon extraction replicas for both SEM and TEM examination were created using a mounted, polished and etched specimen onto which carbon was deposited in an Edwards Auto 306 Vacuum Coater under a vacuum of about 1×10^{-5} torr. The specimen was rotated during carbon deposition to achieve a more uniform coating. Following carbon deposition the carbon film was scribed into a grid of squares approximately 4 mm^2 using a sharp edge. The specimen was then re-etched for several seconds via immersion in the original Kallings No.2 reagent. The carbon film was then floated off in distilled water by lowering the sample slowly into the water at a shallow angle. Water surface tension pulls off the carbon film. The carbon film pieces were then gathered and dried on 3 mm diameter, 200 mesh, copper grid disks for subsequent TEM and SEM examination.

3.4.3 Thin Foil Specimens

The first step in preparing thin foil specimens for TEM examination was to create thin wafers (approximately 300 μm thick) cut via wire EDM (electro-discharge machining). These wafers were then mechanically ground to remove the recast layer produced via EDM cutting and further ground down to an even thickness of approximately 100 μm for electropolishing and 50 to 75 μm for ion milling. 3 mm diameter discs were then punched from these wafers. Electropolished specimens were produced using the common jet polishing technique. The electropolishing solution and conditions used were 10% perchloric acid ($HClO_4$) in methanol with as low a current as possible (100 mA is very good), a voltage of 15 V and a medium flow rate. Ion milled disk specimens were first dimpled on each side in the center of the disk from the starting 50 to 75 μm thickness down to approximately 20 μm using a Gatan 656 Dimple Grinder. After dimpling the specimens are ion milled using a Gatan Model 600 Dual Ion Mill .

3.4.4 Welding and SIMS Analysis Specimens

After the final heat treatments had been chosen and verified, welding specimens were cut from the as-received material in bars of approximately 7.2 cm in length and 16 mm x 16 mm cross-section as shown in Figure 3-4. All welding specimens were sealed in quartz glass as previously described. Each 7.2 cm-long welding specimen was given the primary

homogenization heat treatment, H, then sectioned in two and each half was given a designated solution heat treatment followed by one half being water quenched and the other air cooled. Specimens for SIMS analysis were sectioned as cross-sectional wafers from the "center-end" of the original heat treated welding specimens prior to welding as shown in Figure 3-4. SIMS Specimens were given a fine (1 μm or better) mechanical polish in preparation for analysis.

Prior to electron beam welding the designated weld surface of each specimen to be welded was mechanically ground down to 600 grit SiC paper and cleaned in ethanol in an ultrasonic cleaner. Following EB welding each welded specimen was sectioned in cross-sectional wafers perpendicular to the weld via EDM machining. One set was sectioned in-house using the aforementioned wire EDM cutter while the other was sectioned at Bristol Aerospace Limited. Following sectioning all specimens were mounted, polished and lightly etched as described in section 3.4.1 and displayed in Figure 3-4.

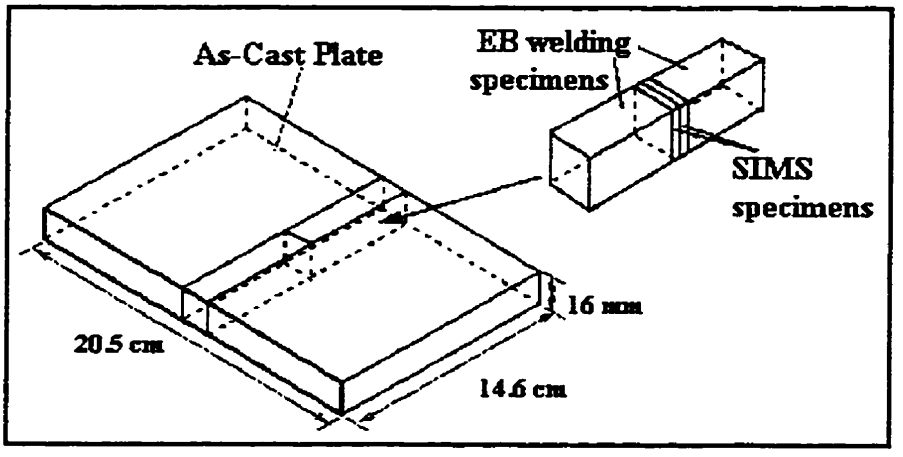

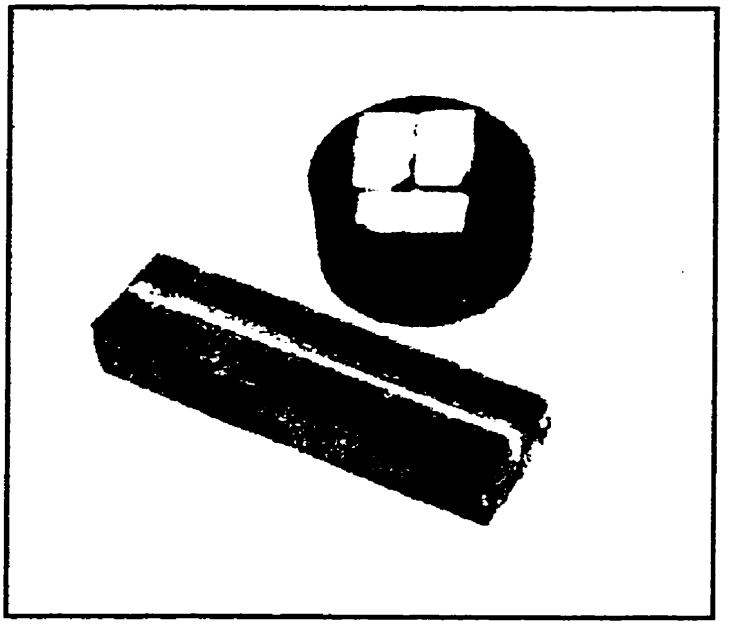

Figure 3-4: Specimens for EB welding, SIMS, optical, and SEM analysis.

3.5 Instrumentation

3.5.1 Optical Microscopy and Optical Image Analysis

Primary optical metallographic observations were conducted using a Nikon EPIPHOT-TME inverted optical microscope with a magnification range of 25 to 1000X and Nikon 35mm and Polaroid camera attachments for image recording as shown in Figure 3-5. Volume fraction and grain size measurements as well as other optical metallographic observations were conducted on a Leitz Image Analyzer. Volume fraction analysis was conducted using manual variable contrast point counting techniques.

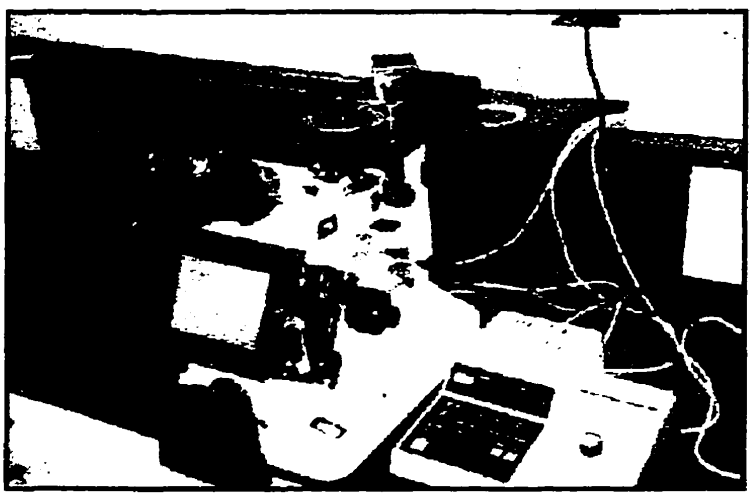

Figure 3-5: Nikon EPIPHOT-TME inverted optical microscope

Great care was taken in each image analyzed that only the desired phases were being counted. Grain size measurements were done entirely via extensive manual grain boundary

intercept counting with three line orientations, five parallel lines per screen, approximately 40 grains per image and over 20 images analyzed per condition. Deviations were all calculated using the standard 95% confidence interval.

3.5.2 Scanning Electron Microscopy (SEM)

SEM microstructural examination is one of the most informative and revealing methods for microstructural research. Microstructural examination using Secondary Electron Imaging (SEI), electron back-scatter imaging and Energy Dispersive Spectroscopy (EDS), for compositional analysis, as well as all HAZ microfissuring measurements were conducted on a JEOL JXA-840 SEM (Figure 3-6). Basic SEM and TEM principles and components are described in detail elsewhere in literature and thus will not be discussed here [37,38,39].

3.5.3 Transmission Electron Microscopy (TEM)

A JEOL 2000 FX TEM and Tracor Northern model TN 5400 EDS detector were used to conduct TEM examination of thin foil specimens and carbon extraction replicas of both the as-received material and heat treated specimens. Diffraction patterns from single carbide particles, along with Kikuchi patterns to center the diffraction patterns along a particular zone axis, were used to determine the crystal structure of the particles.

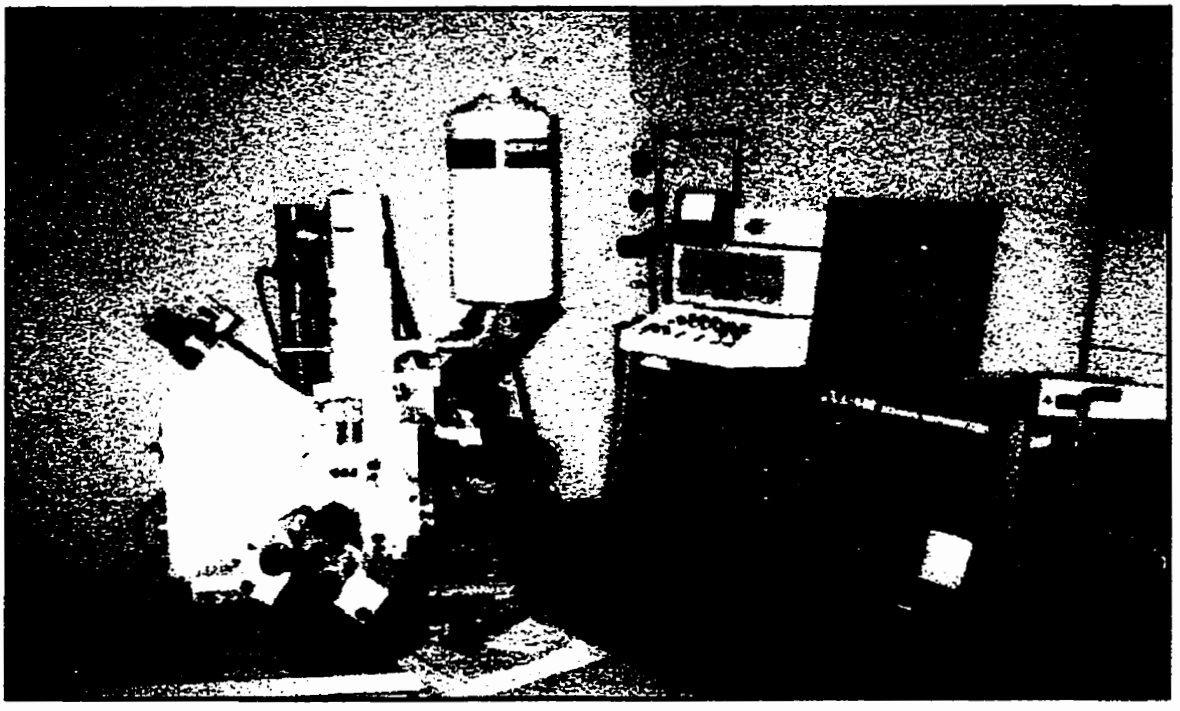

Figure 3-6: Jeol 840 Scanning Electron Microscope (SEM)

3.5.4 Hardness Testing

Although hardness testing was not critical to this study, macrohardness values of the variously heat treated specimens were measured using a standard Vickers pyramid hardness testing machine with a 10 kg load shown in Figure 3-7.

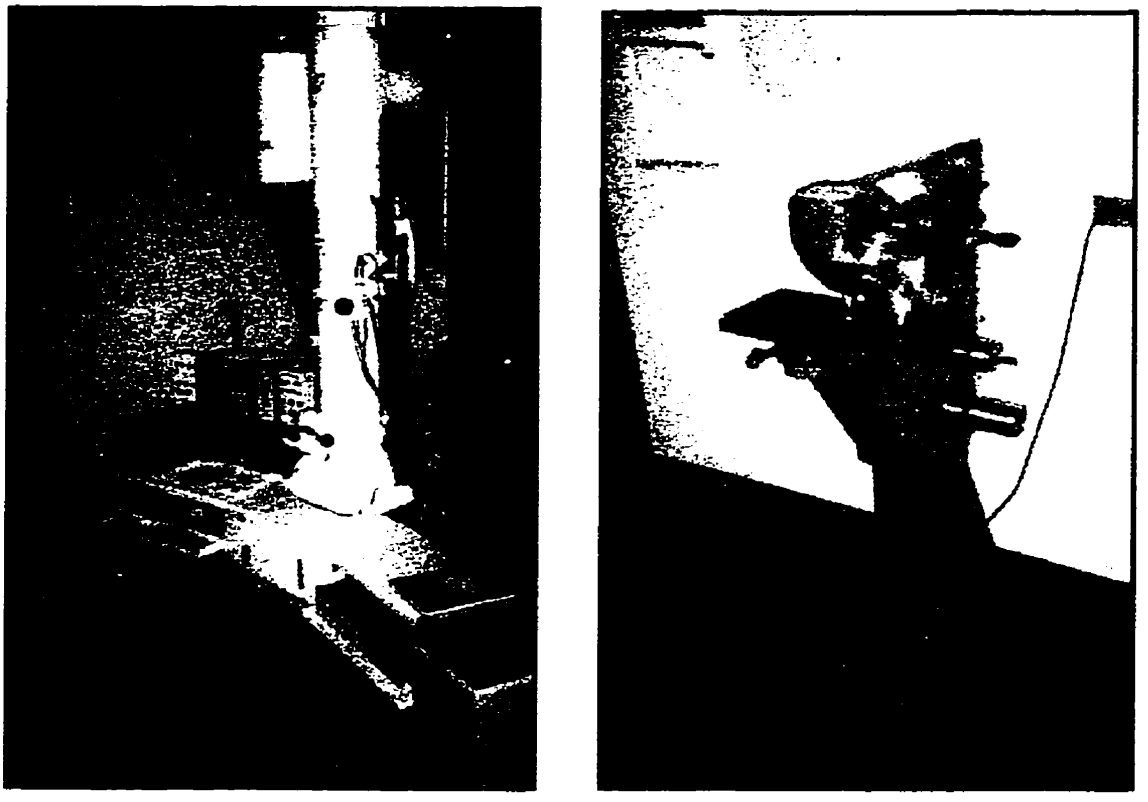

Figure 3-7: Jeol 2000 FX TEM (left) and Vickers hardness testing machine (right)

3.5.5 Secondary Ion Mass Spectrometry (SIMS)

SIMS analysis was vital to this investigation. SIMS equipment is capable of surface compositional analysis (to a depth of 5 to 10 nm) of trace elements in the parts per billion to parts per million range for a very wide range of elements and isotopes [40]. The basic principles of SIMS analysis is the bombardment of the surface to be analyzed with a focused energetic beam of ions under a high vacuum. The collision of the impinging primary ions with the specimen surface causes the ejection (sputtering) of surface atoms and molecules.

Some of the sputtered particles are charged (positively or negatively) and are termed secondary ions. These secondary ions are then passed through a mass spectrometer and thus the ions of different characteristic masses are separated for analysis. As a result, trace elements on the surface can be analyzed and located relative to one another, relative to other elements, or relative to other surface features such as grain boundaries. The spatial resolution of SIMS equipment is typically in the order of a few microns.

SIMS analysis was conducted at CANMET laboratories in Ottawa, Ontario on a Cameca IMS-4f Secondary Ion Mass Spectrometer and Photometrics Series 200 CCD Peltier cooled camera with the assistance of Dr. Gregory S. McMahon. Boron and sulfur were the two trace elements analyzed via SIMS. Boron detection was achieved using an oxygen (O_2^-) primary ion beam with a 250 μm diameter circular imaging area and detection of $^{10}B^{16}O_2^-$ (mass 42) molecular ions. Sulfur detection (S^- secondary ion) was achieved using a cesium (Cs^+) primary ion beam and 100 μm diameter imaging area. Figure 3-8 displays a schematic of the SIMS equipment layout and the actual SIMS used.

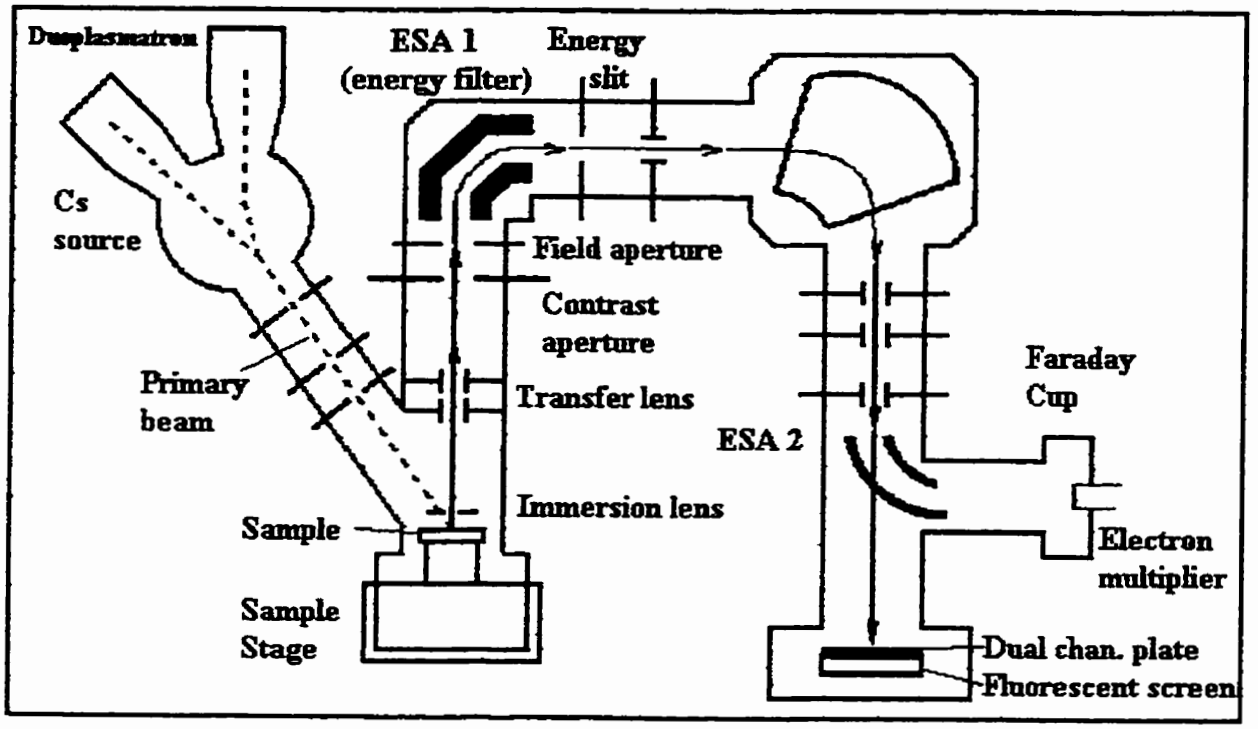

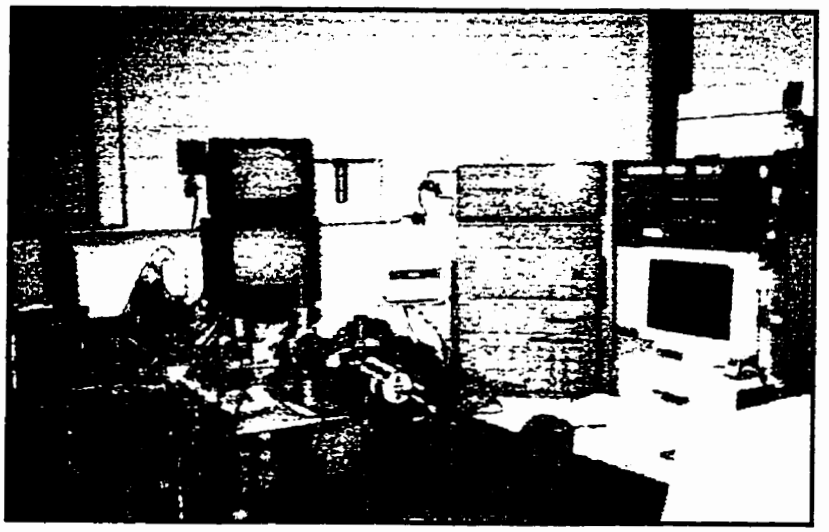

Figure 3-8: SIMS schematic (top) and actual Cameca IMS-4f SIMS (bottom)

3.5.6 Orientation Imaging Microscopy (OIM)

OIM Specimens were prepared from the same specimens used for SIMS analysis mounted in a semi-circular bakelite mold in order to accommodate the specially designed specimen holder. OIM specimens were mechanically polished to 1 micron finish and then electropolished using a 20% sulfuric acid (H_2SO_4) in methanol in order to minimize surface deformation due to mechanical polishing.

3.5.7 Electron Beam Welding and Evaluation of Microfissuring

Electron beam welding of specimens was conducted at Bristol Aerospace Limited in Winnipeg, Manitoba using a Sciaky Mark VII electron-beam welder. A single-pass, focused on surface, bead-on-plate electron beam weld was created on the weld specimens using EB welding parameters give in Table 3-6 below. These welding parameters were chosen to be identical to those used by Dr. Xiao Huang in her doctoral research in order to create some possibilities for comparisons of results. All welding was done at the same time under controlled conditions in order to maximize consistency in the results and reduce the possibility of introducing outside error. Two sets of weld specimens of the same size and same heat treatments were EB welded in order to demonstrate repeatability of the results. Since the trends in each set corresponded well with each other the microfissuring results are presented as one large data set.

Table 3.6: EB Welding Parameters Used for EB Welding of MX-IN-718 Specimens	
Travel Speed	60 ipm (152.4 cm/min)
Accel. Voltage	44 kV
Beam Current	79 mA

Microfissuring evaluation was conducted on the SEM using image collection and analysis via manual measurement of linear segment approximations of each individual microfissure surrounding each cross-section analyzed. A correction factor of 1.3 was needed to transform the image length measured via the IPP program into an actual length in microns. This conversion factor was determined using a stainless steel optical standard and correlating the measurements obtained on IPP to actual lengths marked on the standard. The conversion factor was found to be consistent over the magnification range used for microfissure length measurement.

HAZ Area Estimation

HAZ area was assumed constant for all welds since welding parameters were kept constant and thus the heat input per unit length and weld shape was also constant in all cases. HAZ area was estimated using the optically visible line of liquated or partially liquated Laves and other phases surrounding the weld cross-section in the as-cast welded specimen. One side of

the HAZ was sectioned into areas which were measured on the Leitz image analyzer and the result multiplied by two due to symmetry of the weld profile.

HAZ area was needed to calculate what is known as the Cracking Index (CI). CI is calculated by;

$$CI = \Sigma L_i \; / \; (\text{HAZ Area}) \quad [\text{cm/cm2}]$$

where ΣL_i = Total Crack Length for a given cross-section.

CI is a useful indicator of the extent of microfissuring since other welds may have different heat inputs or weld profiles and hence different HAZ areas. By normalizing the total crack lengths measured with the total HAZ area, the results can be compared to other EB weld microfissuring data using different HAZ areas.

CHAPTER FOUR

RESULTS

4.1 Microstructural Examination

4.1.1 Microstructure of As-Received Microcast-X 718 Material

As shown in Figure 4-1, the microstructure of the Microcast-X material was fine-grained and non-dendritic in nature as opposed to the highly dendritic large-grained microstructure typical of conventionally cast 718. The as-cast (and HIP'd) material was found to display extensive amounts of precipitates of various morphologies which were identified through both morphological observations and compositional EDS analysis (presented later). Laves phase was primarily located at grain boundary triple points and surrounded by γ'' particles. MC carbides or carbonitrides (M(C,N)) were observed to be evenly dispersed within the grains and occasionally appearing along grain boundaries. The δ needles commonly found in conventionally cast 718 appeared only rarely among clusters of γ'' particles. Figure 4-2 displays the carbides, rare δ phase needles, Laves phase, and γ'' precipitates at higher magnification.

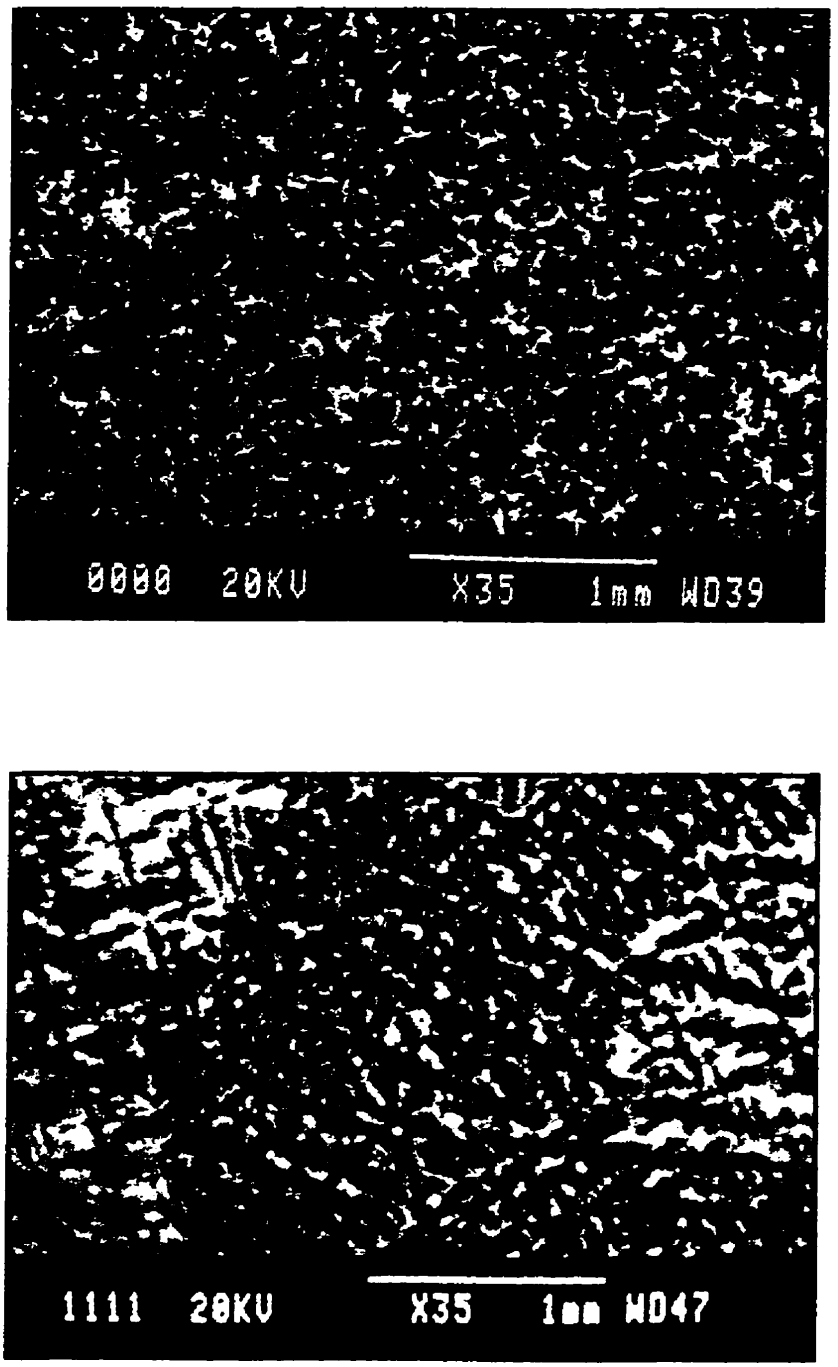

Figure 4-1: As-received Microcast-X Inconel 718 (top) and conventional cast 718 (bottom).

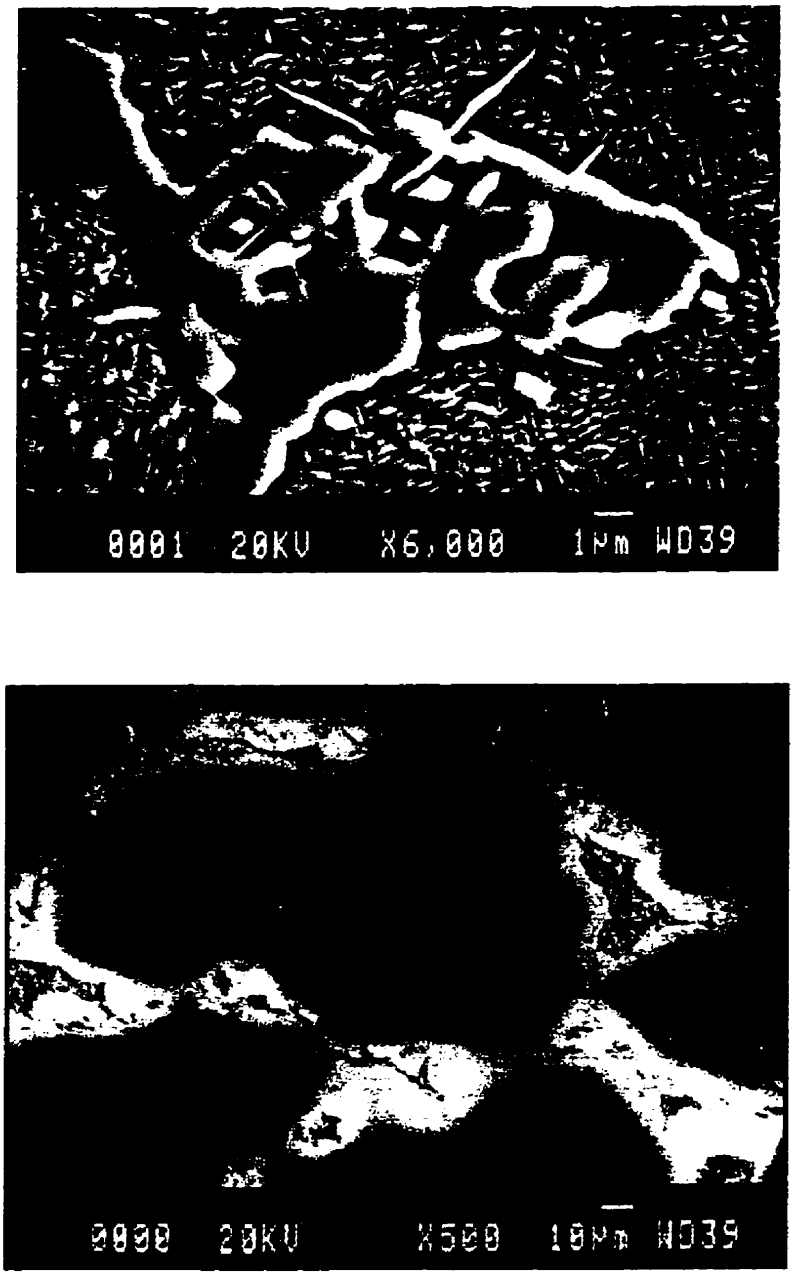

Figure 4-2: SEM micrographs at 6000X (top) and 500X (bottom) magnification showing Laves phase , γ'' particles, δ phase and carbide precipitates found in as-cast MX IN-718.

4.1.2 Microstructure After Homogenization Heat Treatments

After conducting the various homogenization heat treatments, discussed in Chapter 3, it was found that many of the heat treatments produced very similar microstructures and thus only one micrograph is presented below for each type of microstructure. All homogenization heat treatments dissolved all γ'' precipitates and little or no re-solidified Laves phase remained. However residual Laves was detected in specimens heated quickly or heat treated for very short periods of time. Grain growth was always sporadic with a sudden increase in growth, forming mixed clusters of small and large grains which later stabilized at a large grain size after sufficient time at a particular heat treatment temperature, as shown in Figures 4-3 to 4-5. The optimum homogenization heat treatment of 70 minutes slow heating from 1000 °C to 1200 °C followed by a holding time of 30 minutes at 1200 °C then water quenching resulted in virtually no residual or resolidified Laves phase and thus the "cleanest" microstructure achieved with no significant grain growth. Carbide (and carbonitride) volume percentage remained the same while all other observable phases had gone into solution.

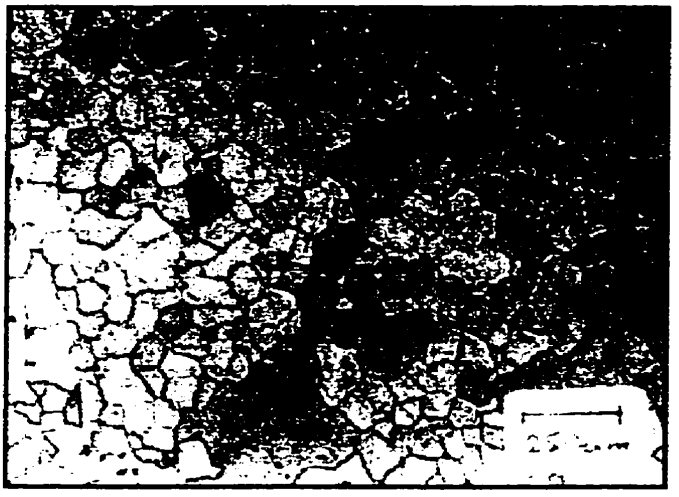

Figure 4-3: Homogenized microstructure with little or no grain growth achieved for heat treatments of 4 hours at 1150 °C, or 1 hour or less at 1200 °C.

Figure 4-4: Homogenized microstructure with sporadic mixed grain growth achieved for heat treatments of 5 hours at 1175 °C, or 1 to 3 hours at 1200 °C.

Figure 4-5: Homogenized microstructure with stable large grains achieved for heat treatments of >15 hours at 1150 °C, >10 hours at 1175 °C, or >4 hours at 1200 °C.

4.1.3 Microstructure After Solution Heat Treatments

The microstructure of all the specimens which were given one of the six designated heat treatments following the initial optimum homogenization heat treatment was a clean fine-grained microstructure as shown in Figure 4-6 with a small amount of fine precipitates (Figure 4-8 and 4-9), identified via TEM to be a mixture of fine sulfide particles and occasional particles high in Mo (likely to be carbide or boride particles but were not identifiable via TEM/EDS due to difficulty in light element detection), appearing along grain boundaries as well as within the grains. Solution heat treating at 1000 °C created extensive δ phase formation as shown in Figure 4-7.

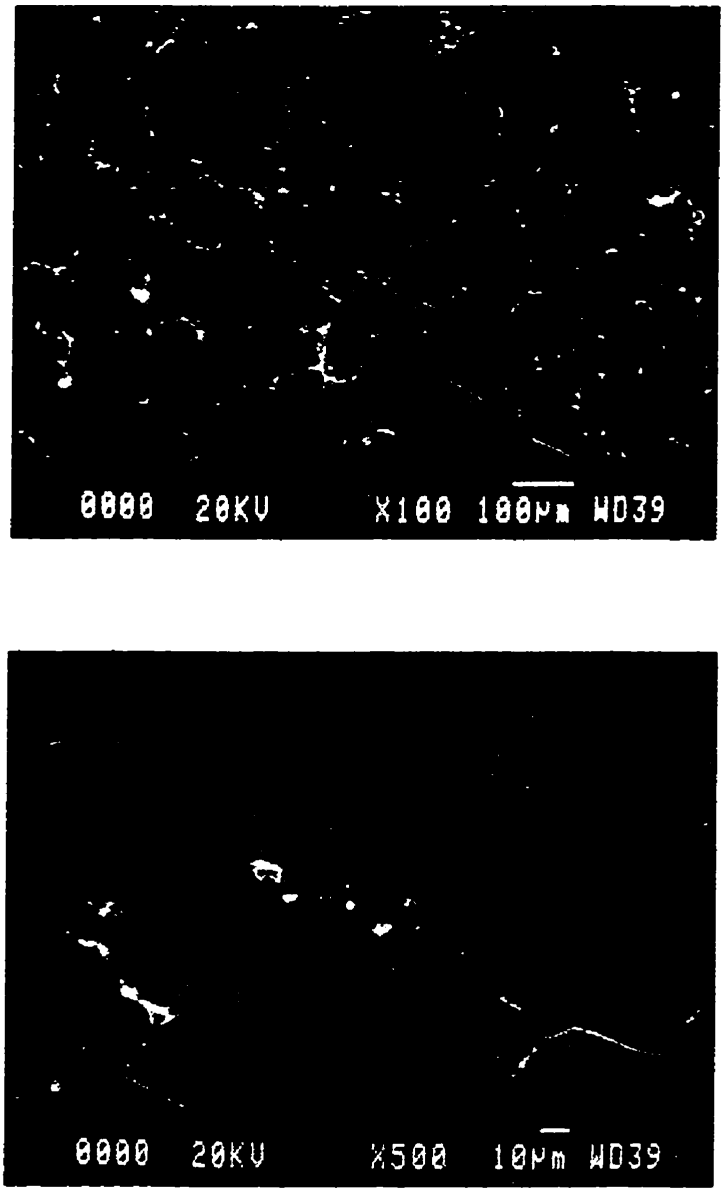

Figure 4-6: Solution heat treated microstructure with no grain growth achieved for heat treatments of 14, 8 and 5 hours at 1050 °C, 1100 °C and 1150 °C respectively at 100X (top) and 500X (bottom) magnification.

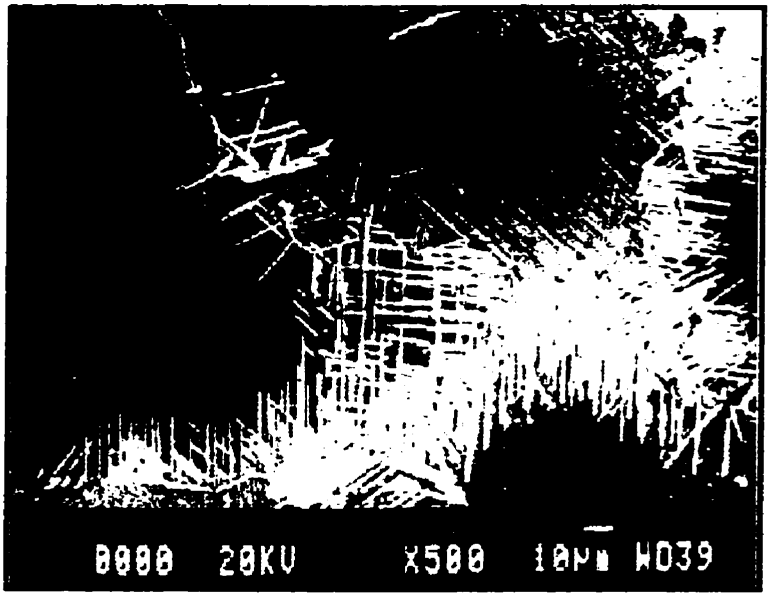

Figure 4-7: Solution heat treated microstructure with extensive δ phase formation along grain boundaries resulting for a solution heat treatment of 30 hours at 1000 °C (AC and WQ).

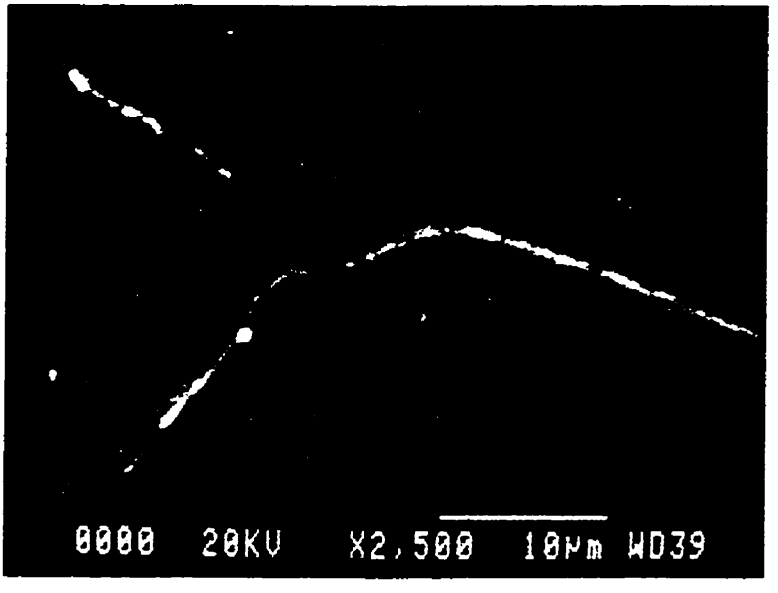

Figure 4-8: SEM micrograph of fine spheroidal precipitates found in solution heat treated specimens.

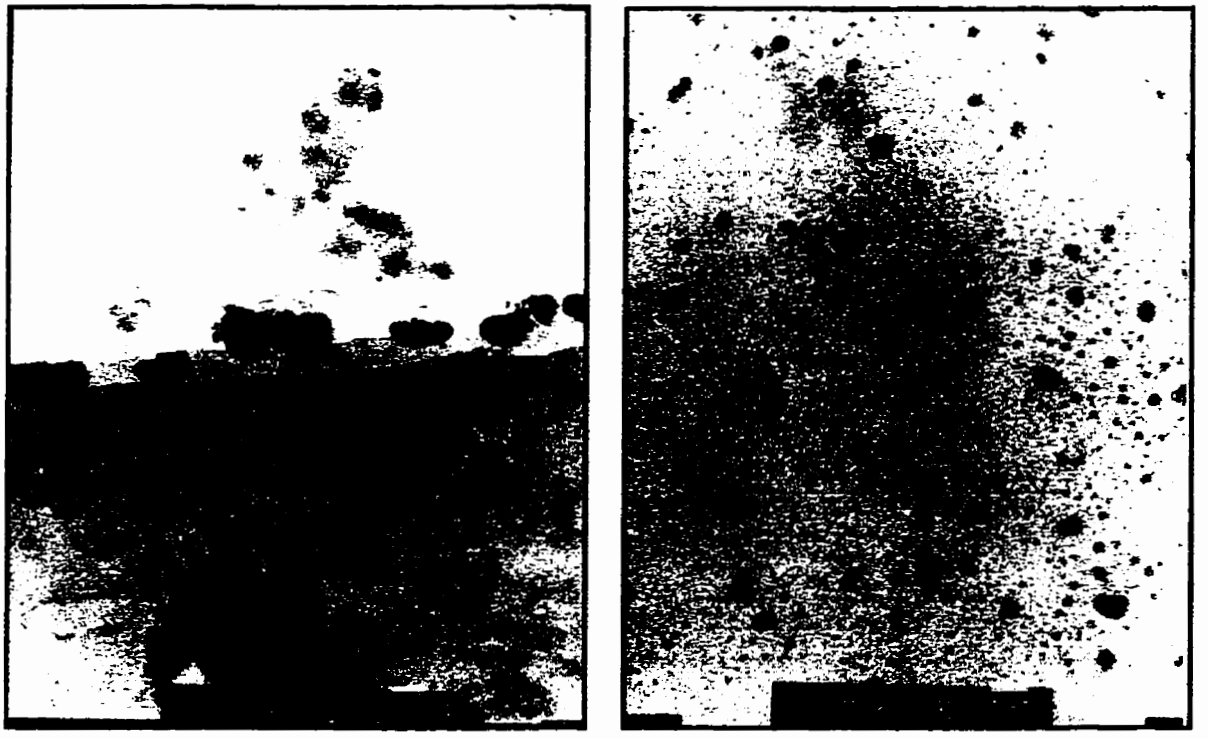

(i) High in titanium (ii) High in manganese

Figure 4-9: TEM micrographs of fine spheroidal sulfide precipitates found in solution heat treated specimens.

Carbide particles were also analyzed via TEM examination of carbon extraction replicas as shown in Figure 4-10. The diffraction patterns were acquired and analyzed in order to determine the crystal structure of the carbide particles. Using these diffraction patterns and the wavelength of the beam electrons at an accelerating voltage at 200.0 kV these particles were shown to be of FCC structure with lattice parameter a = 0.446 nm which identifies them to be, as expected, MC-type carbide or M(C,N)-type carbonitride well within experimental error and not $M_{23}C_6$.

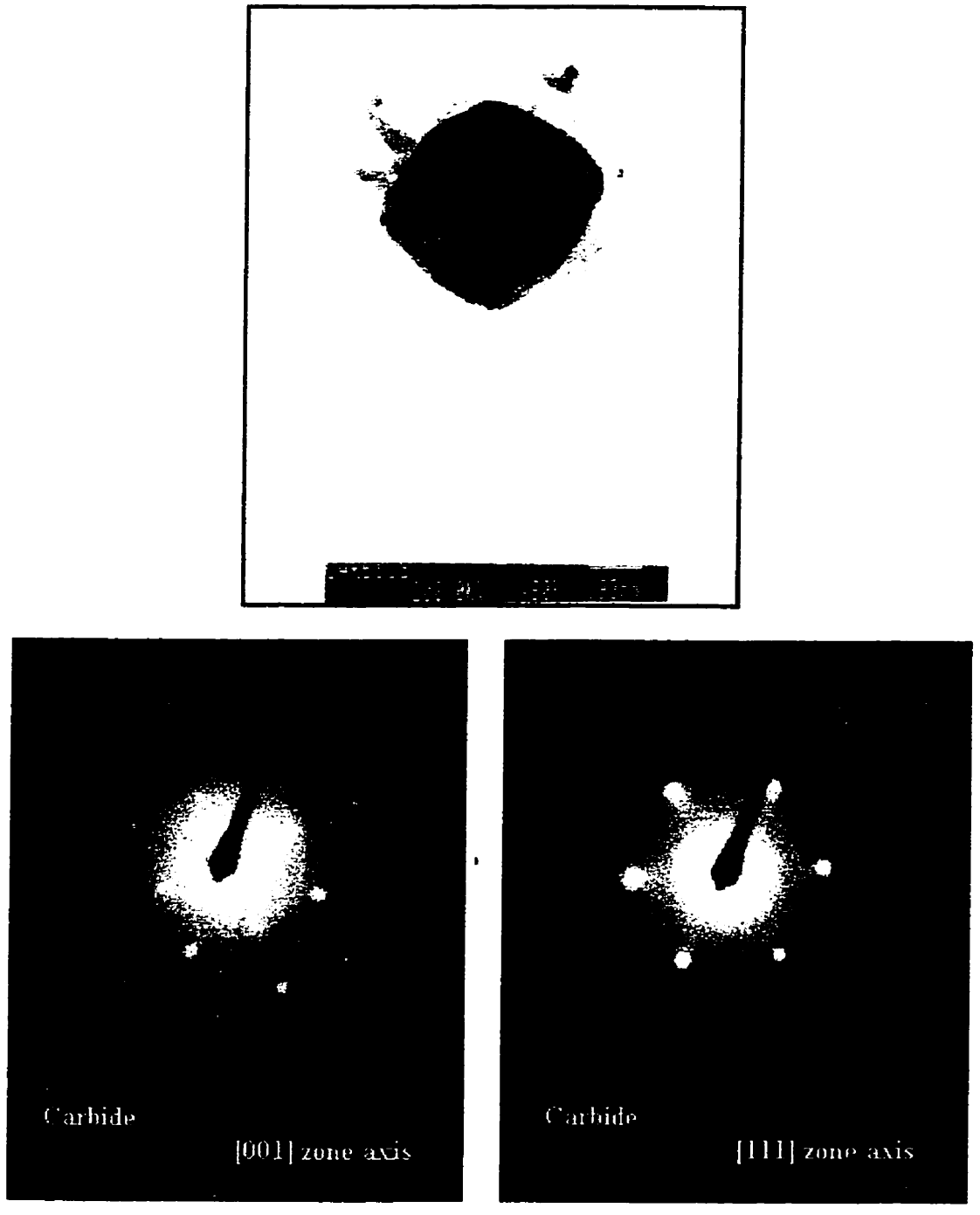

Figure 4-10: TEM micrograph and diffraction patterns for a niobium carbide particle.

4.2 Grain Size Measurements

Grain size measurements conducted on Leitz Image Analyzer served to quantify the increase in grain size with homogenization heat treatment time and are provided in Table 4-1 along with a 95% confidence limit (CL) where HLD refers to holding time and SH to slow heating from 1000 °C. Grain sizes increased suddenly from the order of 100 microns to nearly 1 mm when the material was heat treated at 1200 °C. Grain size measurements were also conducted on specimens after the final heat treatments which were used for EB welding in order to verify that the grain size remained virtually constant. These measurements are provided in Table 4-2.

Table 4-1: Grain Size Measurements for Homogenization Heat Treatments of MX IN-718

Homogenization Heat Treatment	Grain Size [μm]
1200 °C - 70 min. SH, 30 min. HLD - WQ	90 ± 6
1200 °C - 120 min. SH, 30 min. HLD - WQ	110 ± 15
1200 °C - 1 hour HLD - WQ	79 ● 2
1200 °C - 2 hour HLD - WQ	89 ± 3
1200 °C - 2.5 and 3 hour HLD - WQ	mixed
1200 °C - 4 hour HLD - WQ	700 ± 40
1200 °C - 15 hour HLD - WQ	780 ± 36
1200 °C - 24 hour HLD - WQ	no apparent increase

Table 4-2: Grain Size Measurements for Homogenized and Solution Heat Treated Specimens	
Solution Heat Treatment	**Grain Size [μm]**
1050 - 14 hrs - AC/WQ	89 ± 7
1100 - 8 hrs - AC/WQ	100 ± 10
1150 - 5 hrs - AC/WQ	88 ± 6
As-Cast +HIP'd	85 ± 3

4.3 Cooling Rate Test

Cooling rate tests were conducted as described previously in order to establish the cooling rates experienced by the welding specimens for the purpose of comparison to previous work and for future studies. Cooling results are presented in Table 4-3 below and show some variation between internal and external cooling rates during water quenching while both internal and external cooling rates matched extremely well under air cooling conditions. Actual cooling curves are presented in Figure 4-11. Specimen mass was measured to be 138.8 grams.

Table 4-3: Cooling Rate Test Results (Rates are given for cooling from 1200 to 600 °C)		
Cooling Method	**Internal [°C/sec]**	**External [°C/sec]**
Water Quench	100	600
Air Cool	5.6	5.6

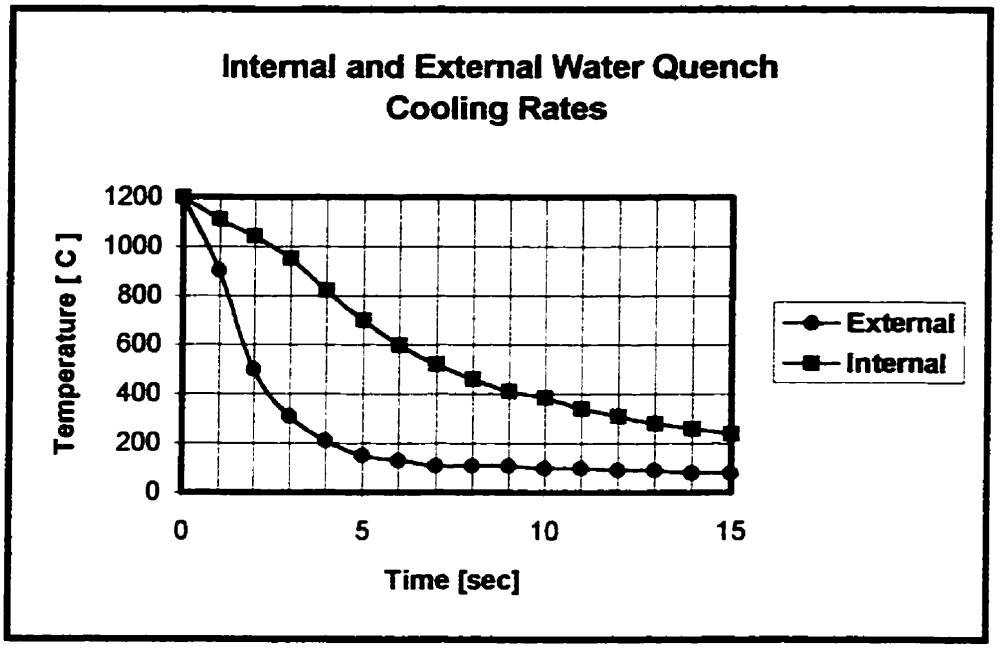

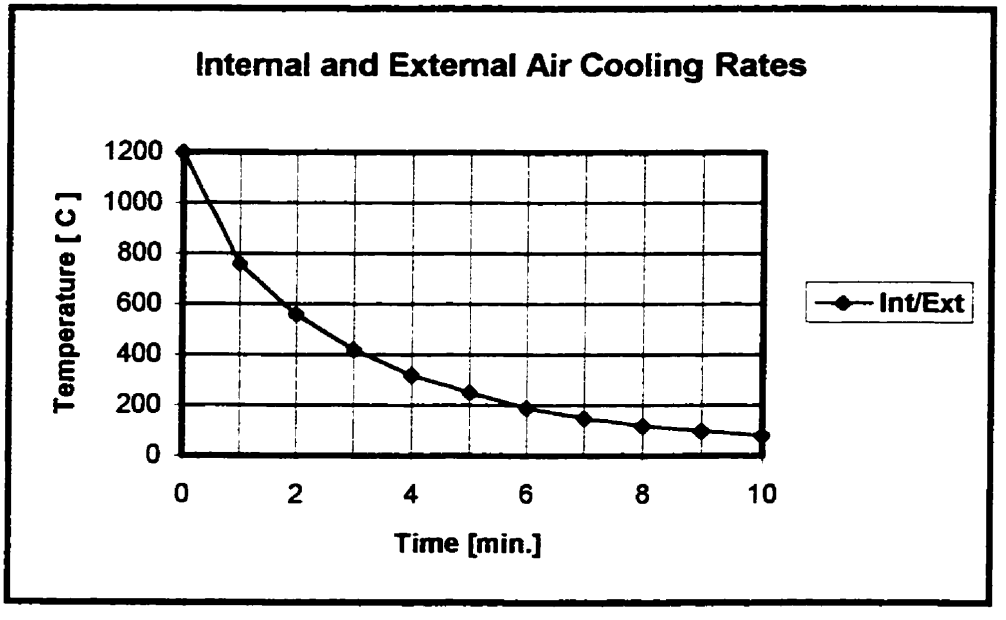

Figure 4-11: Water quench (top) and air cooling (bottom) cooling rate tests for Microcast-X IN-718 weld specimens.

4.4 Hardness Measurements

Macrohardness measurements were conducted using a standard Vickers hardness tester in order to verify hardness consistency for the different solution heat treatment conditions and comparison with the as-cast material hardness. Results are presented in Figure 4-12. Conversions to Rockwell were not done since the as-cast value would appear on the Rockwell C scale while corresponding heat treated values would appear on the Rockwell B scale.

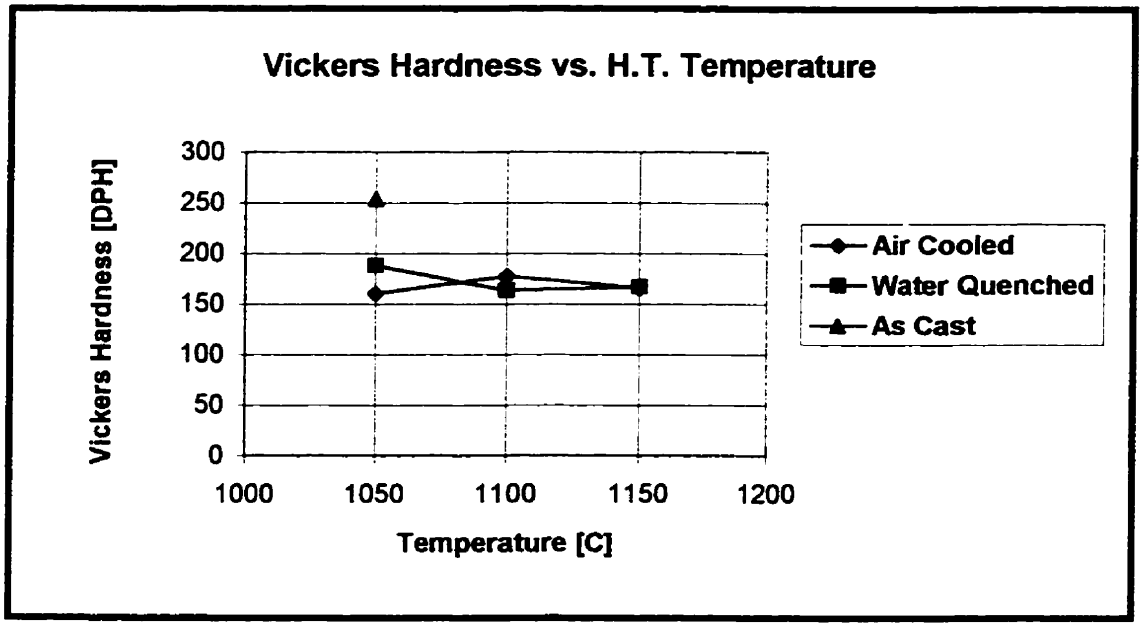

Figure 4-12: Vickers diamond pyramidal macrohardness values for solution heat treated and as-cast specimens.

4.5 Volume Percentage of Phases and Residual Porosity

Volume percentage of secondary phases and porosity level in the as-cast material were analyzed and are presented in Table 4-4 below. Carbide and porosity levels were also measured in the homogenized and variously solution heat treated conditions and no significant changes to either were found as compared to the as-cast condition. δ and γ'' phases were not present in the heat treated specimens and residual Laves content was small enough to be immeasurable via the image analysis technique used.

Table 4-4 : Volume Percentage of Phases in As-Cast Microcast-X Inconel 718 (95 % CL)

Porosity	0.22 ± 0.06
Carbides	1.8 ± 0.2
Laves	2.7 ± 0.8
γ''	13.4 ± 0.8
All	18.1 ± 1.7

4.6 Qualitative Analysis of Secondary Phases

Several phases were analyzed using SEM/EDS and TEM/EDS compositional analysis and are provided in Table 4-5a and 4-5b. EDS spectra of these phases are presented in Figures 4-13 to 4-16. Copper peaks visible on the TEM spectra result from the copper grid upon which the carbon extraction replicas are trapped and the silicon peaks originate from the EDS detector itself.

Table 4-5a: SEM/EDS Chemical Composition of Secondary Phases (wt%)

Phase	Nb	Mo	Ni	Fe	Cr	Ti	Al	Si	Nb+Mo
NbC	76.9	11.5	0.8	0.3	0.5	9.6	-	0.3	88.5
Laves	29.8	8.9	32.8	15.8	10.0	2.5	-	0.1	38.7
HAZ liquid - As-cast	28.5	9.3	32.0	17.2	10.6	2.2	0.1	0.2	37.7
HAZ liquid - Sol. H.T.	11.8	5.0	41.6	24.5	15.0	1.7	0.1	0.3	16.8
Near Grain Boundary	9.4	4.4	40.3	28.7	15.0	1.5	0.5	0.2	13.8
Base Metal	6.0	5.0	41.8	28.0	16.7	1.5	0.5	0.4	11.0

Table 4-5b: TEM/EDS Chemical Composition of Precipitate Particles (wt%)

Phase	Nb	Mo	Ni	Fe	Cr	Ti	Mn	S	Nb+Mo
Sulfide (high Ti)	-	-	2.6	0.3	3.5	58.4	3.4	31.9	-
Sulfide (high Mn)	-	-	13.6	8.0	3.3	-	28.1	47.1	-
High Mo (boride or carbide)	38.9	43.4	1.2	2.7	13.3	0.4	-	-	82.3

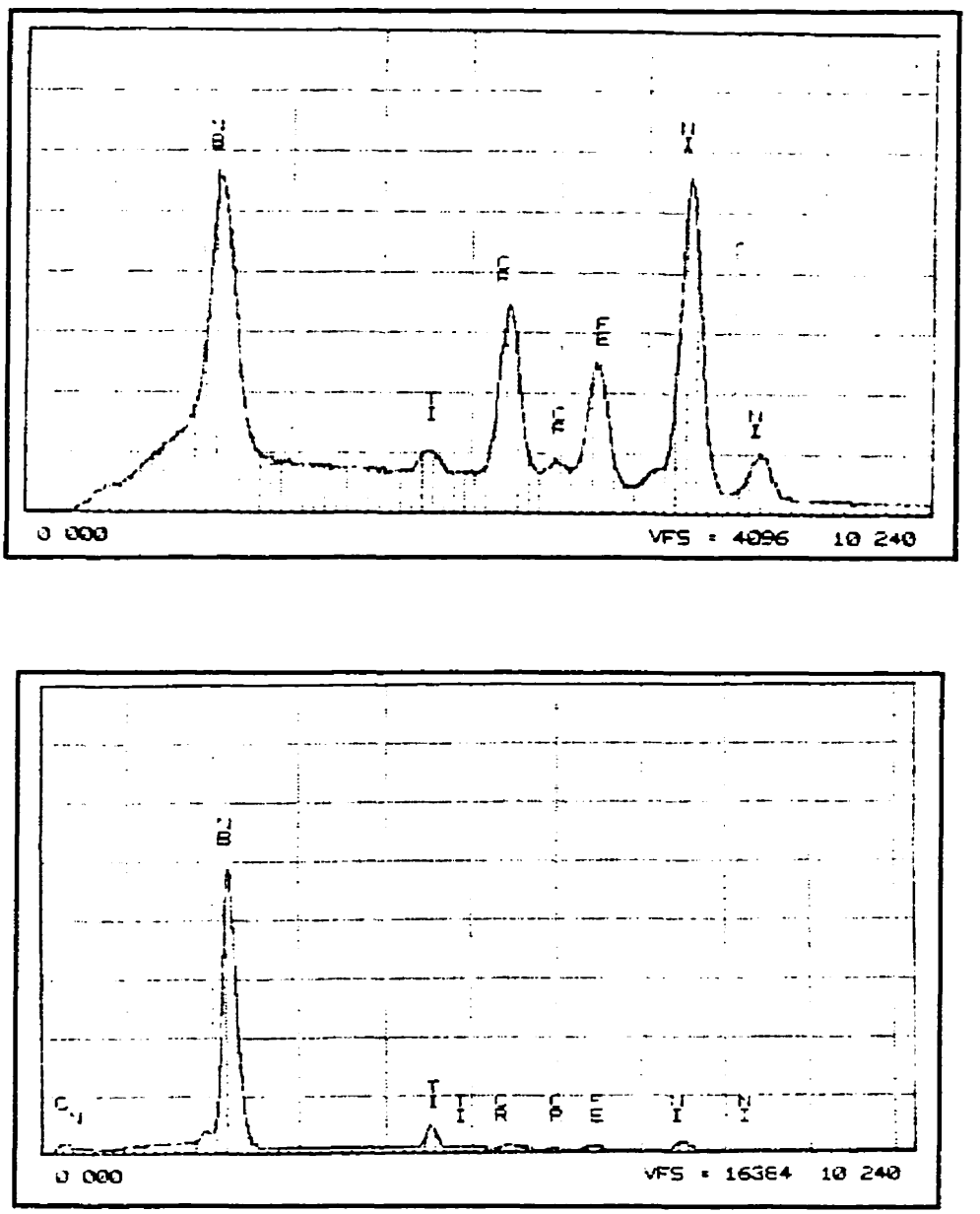

Figure 4-13: SEM/EDS spectra for Laves phase (top)

and (Nb,Mo,Ti)(C,N) carbonitrides (bottom).

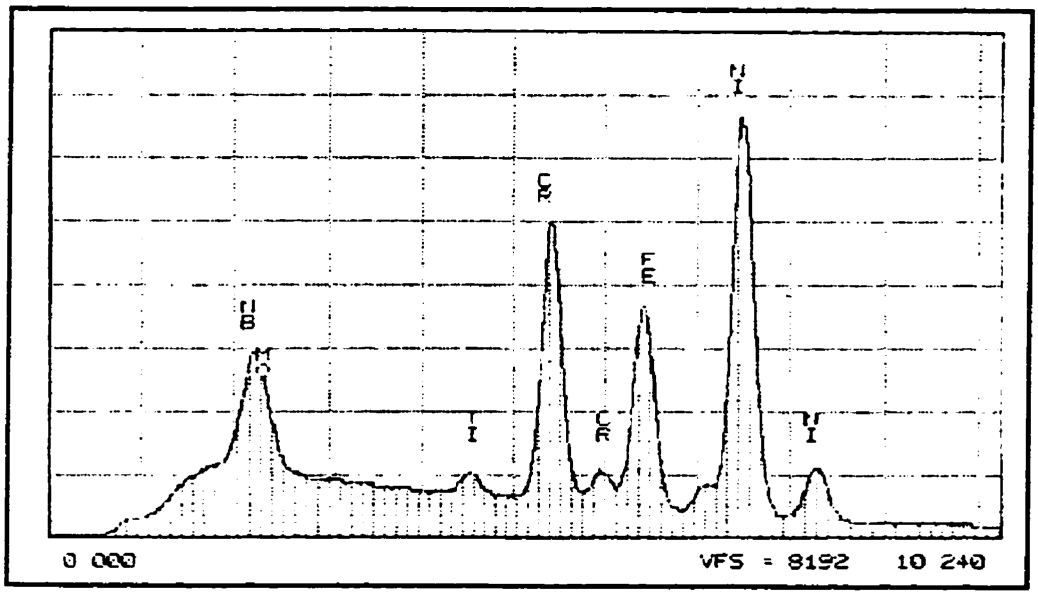

Figure 4-14: SEM/EDS spectrum for resolidified HAZ grain boundary liquid

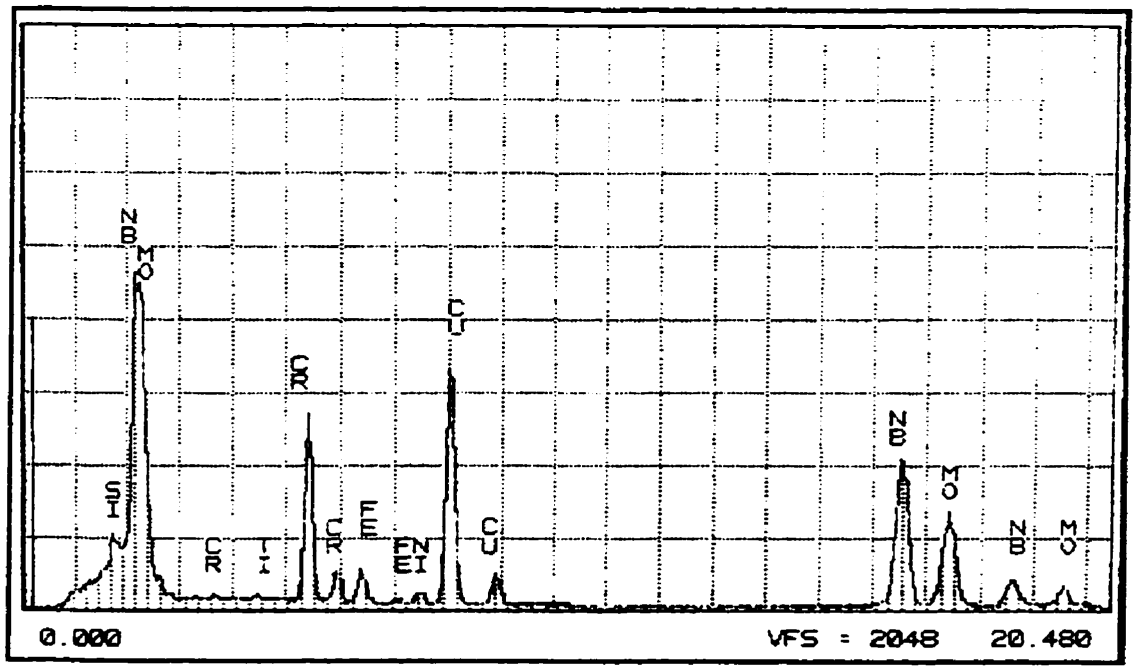

Figure 4-15: TEM/EDS spectrum for grain boundary precipitate particles high in Mo.

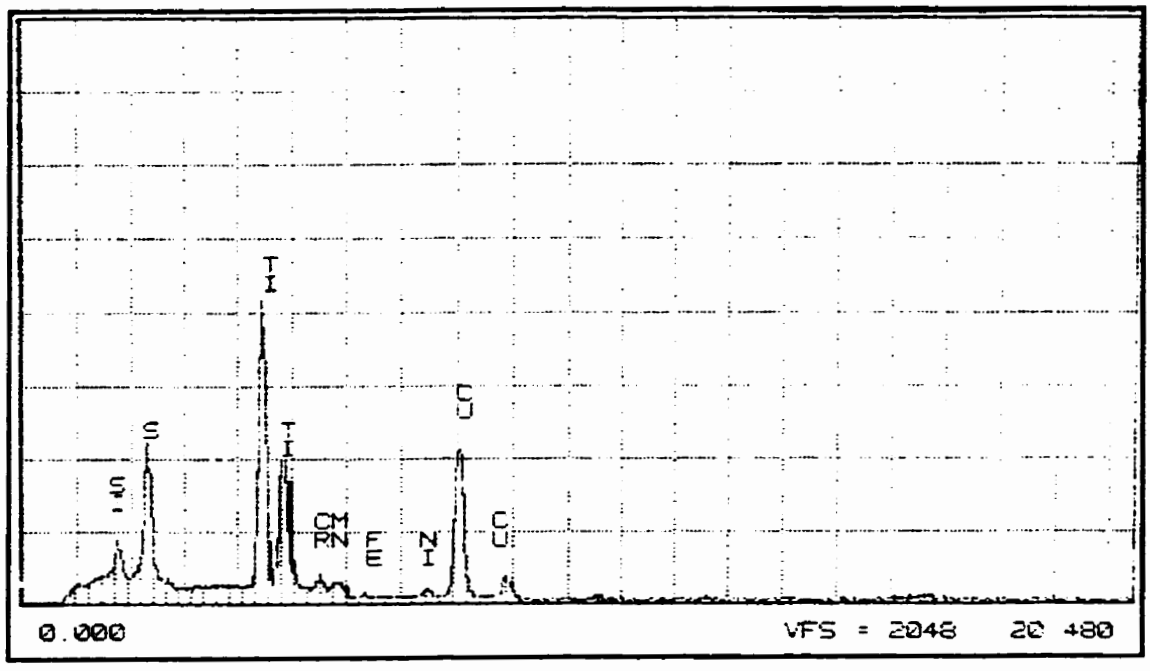

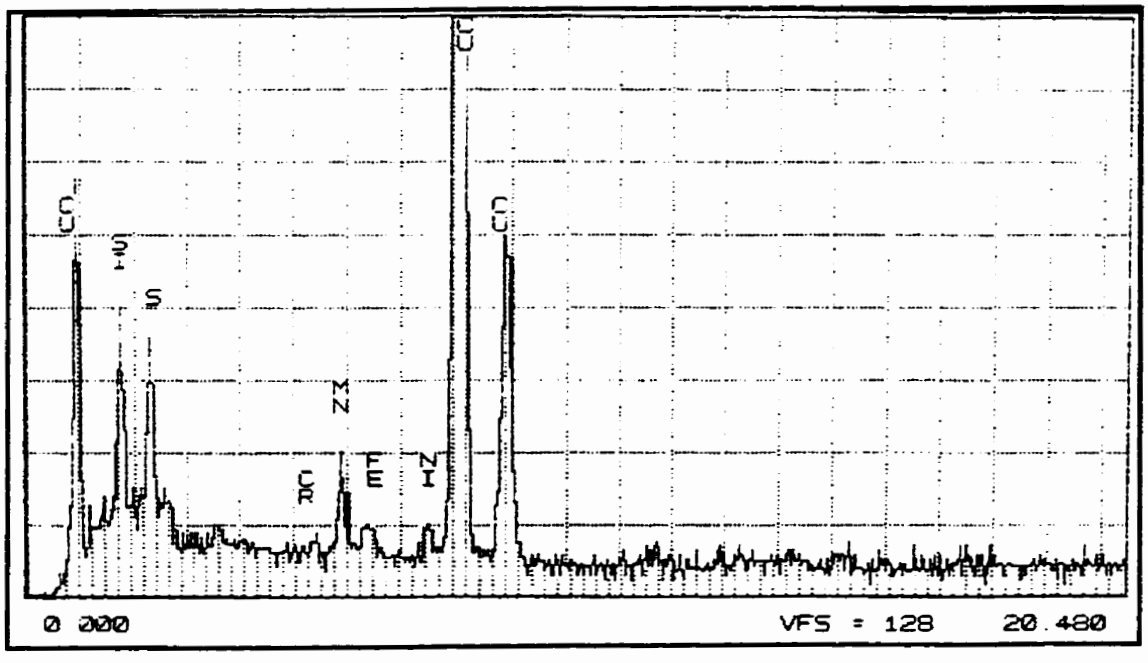

Figure 4-16: TEM/EDS spectra for sulfide particles; (top) high in Ti, (bottom) high in Mn.

4.7 SIMS Analysis

4.7.1 Introduction

Secondary Ion Mass Spectrometry (SIMS) analysis was conducted, as described in Chapter 3, on the six differently heat treated specimens and on the as-cast material in order to locate elemental boron and sulfur relative to grain boundaries and other microstructural features. Carbon was also analyzed but did not show any significant information aside from carbide locations and thus is not presented here.

4.7.2 Boron Segregation

Boron demonstrated a very strong trend coinciding with expected behaviour. Boron segregation was significantly stronger in all air cooled specimens as compared to water quenched specimens and the intensity of boron segregation to grain boundaries increased with increasing heat treatment temperature. The resulting boron SIMS images are presented in the following pages in Figures 4-17 to Figure 4-20. Boron scans are 250 microns in diameter.

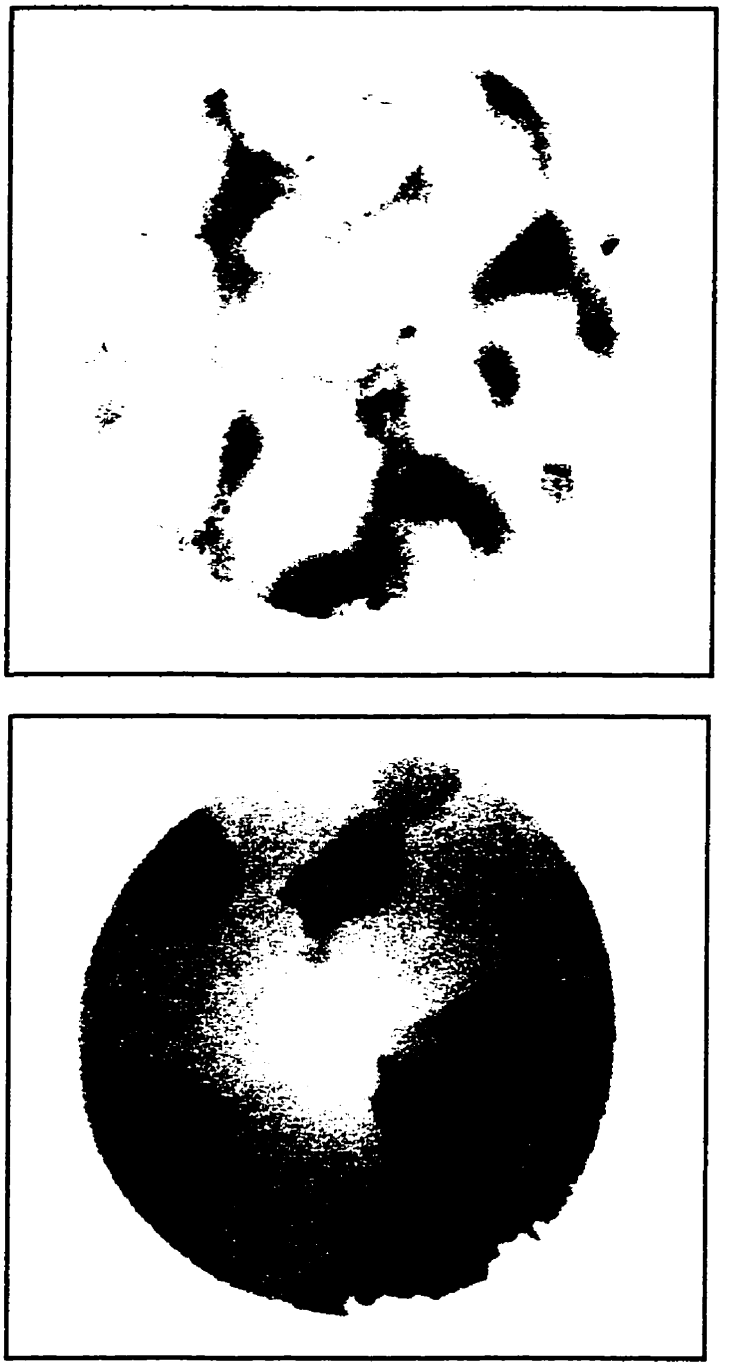

Figure 4-17: SIMS boron (top) and oxygen sputter (bottom) images for as-cast MX IN-718 showing boron initially segregated near grain boundaries.

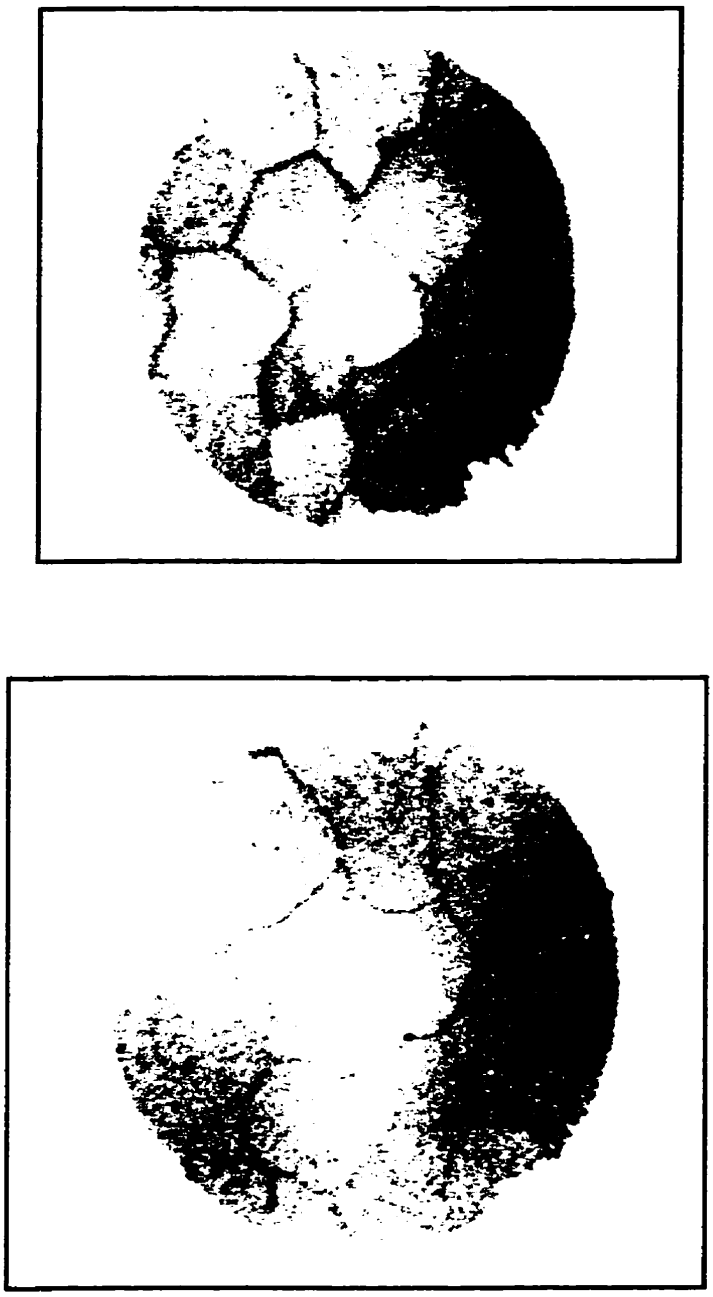

Figure 4-18: Air cooled (top) and water quenched (bottom) SIMS boron images for a solution heat treatment temperature of 1050 °C.

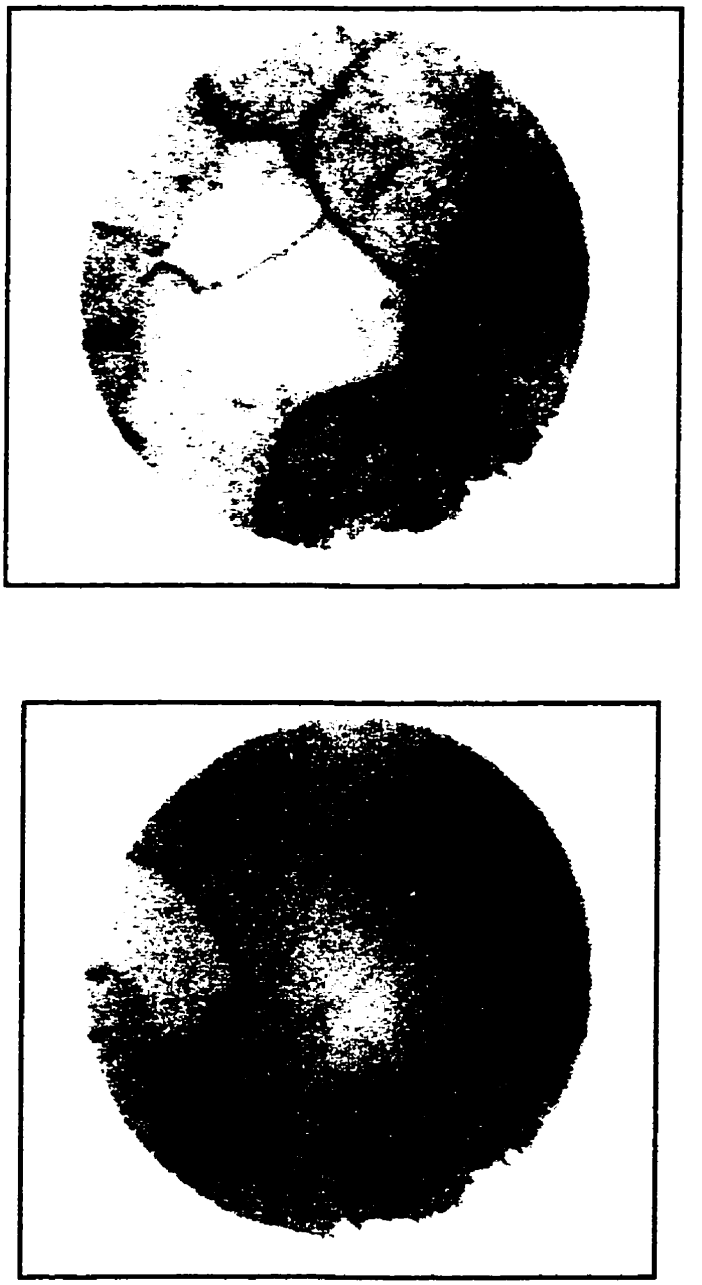

Figure 4-19: Air cooled (top) and water quenched (bottom) SIMS boron images for a solution heat treatment temperature of 1100 °C.

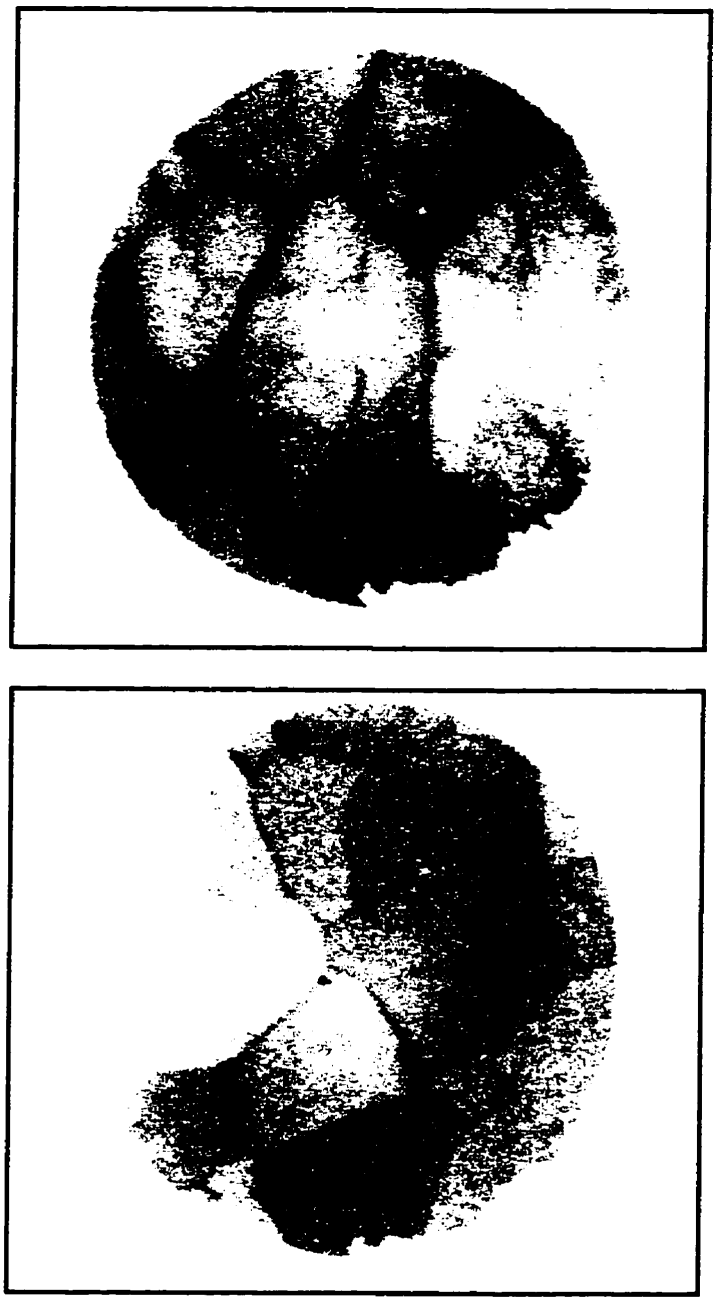

Figure 4-20: Air cooled (top) and water quenched (bottom) SIMS boron images for a solution heat treatment temperature of 1150 °C.

4.7.3 Sulfur Segregation

SIMS imaging of sulfur, as shown in Figure 4-21, revealed sulfur segregation to grain boundaries to be virtually the same for each heat treatment level with sulfur appearing primarily as sulfide particles. These results are as expected since heat treatments were designed to achieve equilibrium levels of sulfur segregation at each temperature. Cooling rate did not seem to affect sulfur segregation appreciably. Sulfur did not appear to segregate to carbide particles. These sulfide particles are also shown decorating the grain boundaries in Figure 4-9.

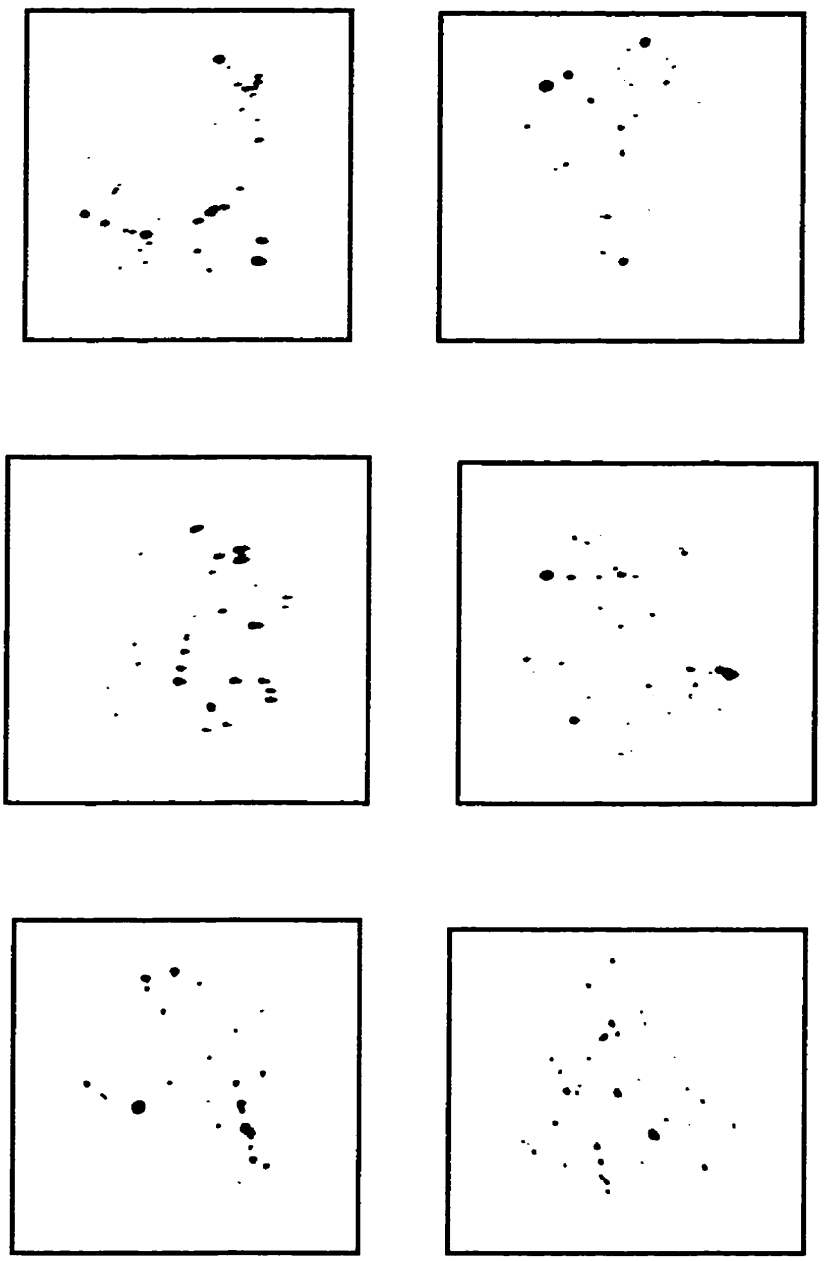

Figure 4-21: Air cooled (left) and water quenched (right) SIMS sulfur images for solution heat treatment temperatures of 1050 °C (top), 1100 °C (middle) and 1150 °C (bottom).

4.8 OIM Analysis

The following images are examples of OIM scan results for each heat treatment temperature as well as the as cast structure. Image mapping results are provided in Figures 4-22 to 4-30 with red boundaries indicating CSL (coincident site lattice) boundaries of sigma values between 1 and 15. Histograms of misorientation angle and CSL boundary types (sigma value) generated from numerical analysis of the acquired data are presented in Figures 4-27 to 4-30. A pole figure map which was typical of all scans is provided in Figure 4-22 to demonstrate the lack of preferred orientation of grains in the material.

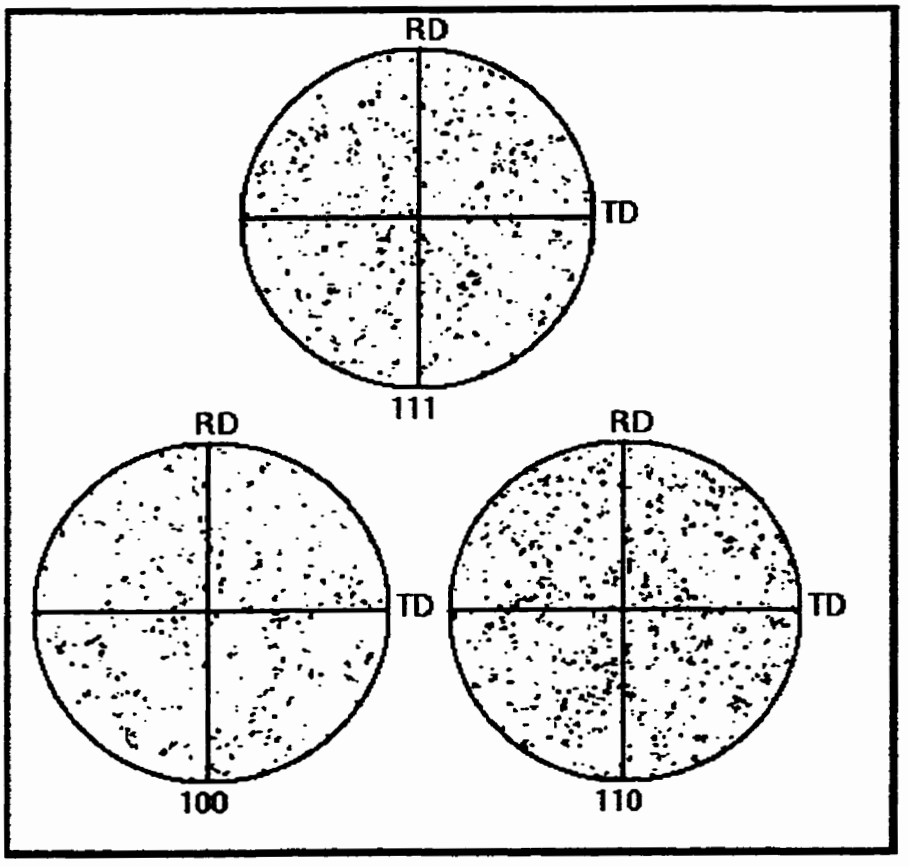

Figure 4-22: Three pole figures showing lack of preferred crystallographic orientation found in all specimens.

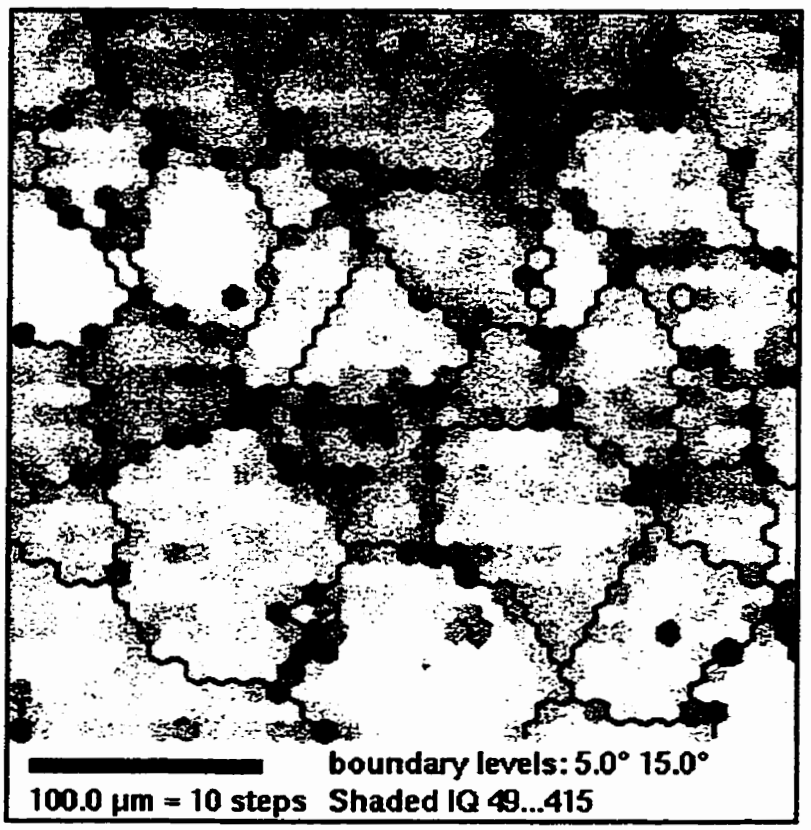

Figure 4-23: OIM image map of grain boundaries in as cast MX IN-718.

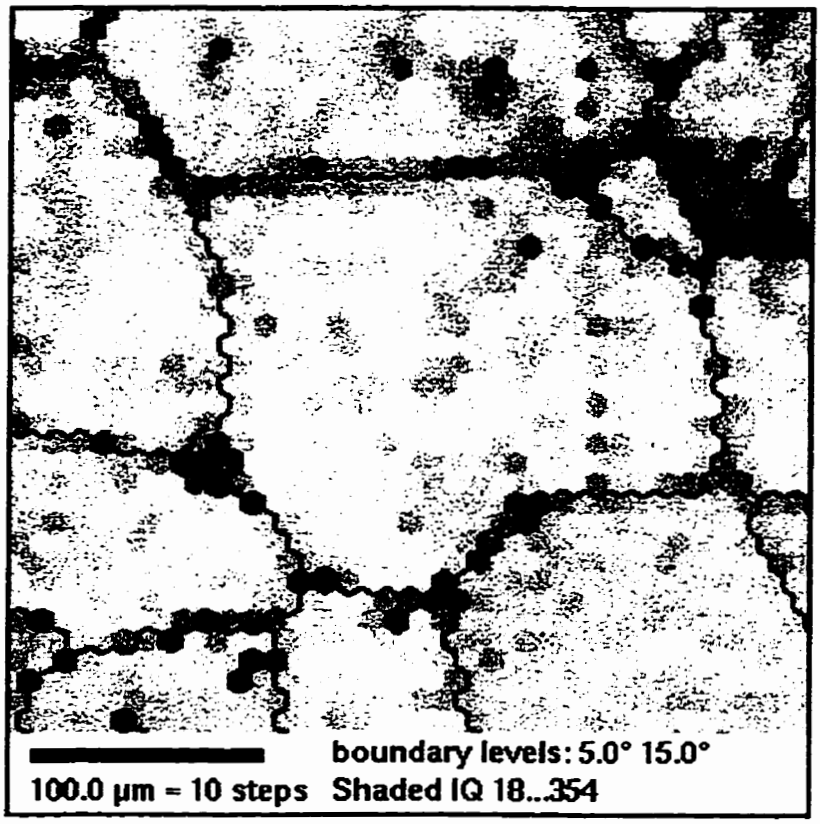

Figure 4-24: OIM image map of grain boundaries in MX IN-718 with primary homogenization followed by 1050 °C / 14 hour solution heat treatment.

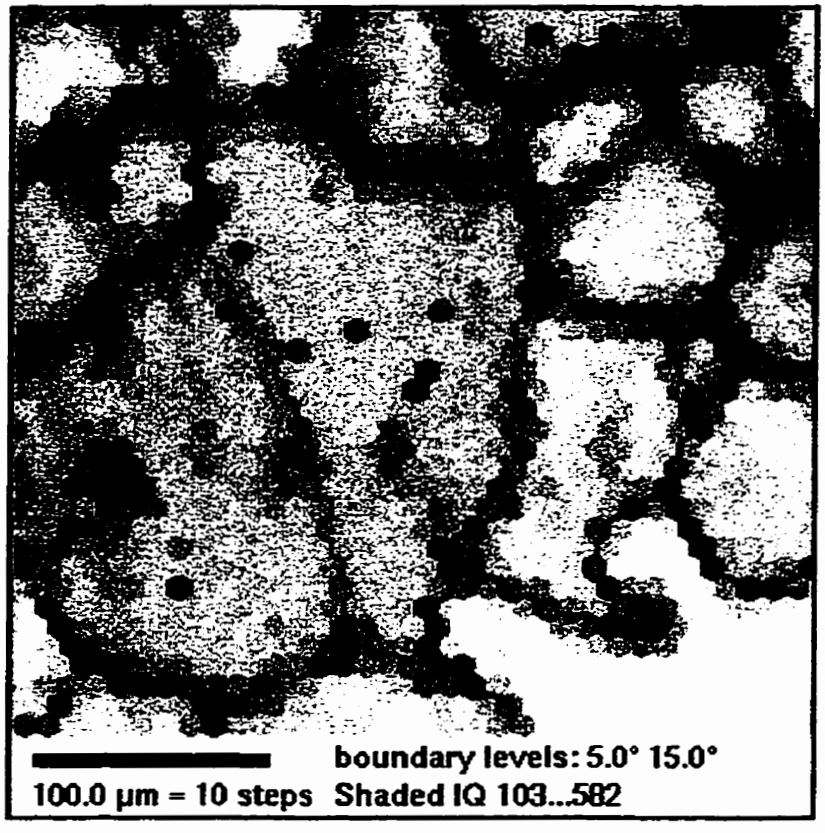

Figure 4-25: OIM image map of grain boundaries in MX IN-718 with primary homogenization followed by 1100 °C / 8 hour solution heat treatment.

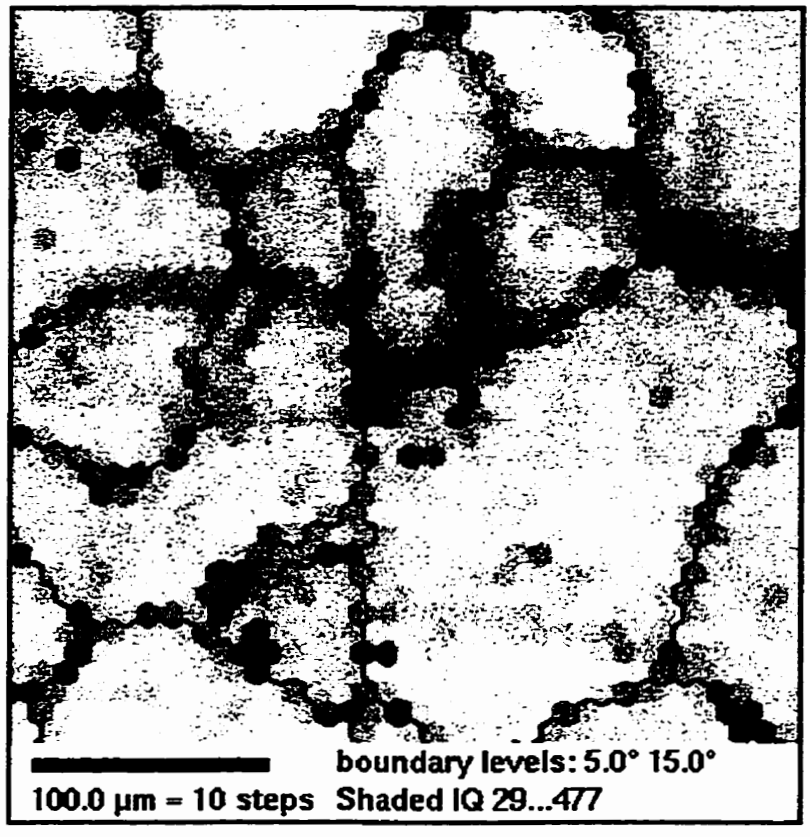

Figure 4-26: OIM image map of grain boundaries in MX IN-718 with primary homogenization followed by 1150 °C / 5 hour solution heat treatment.

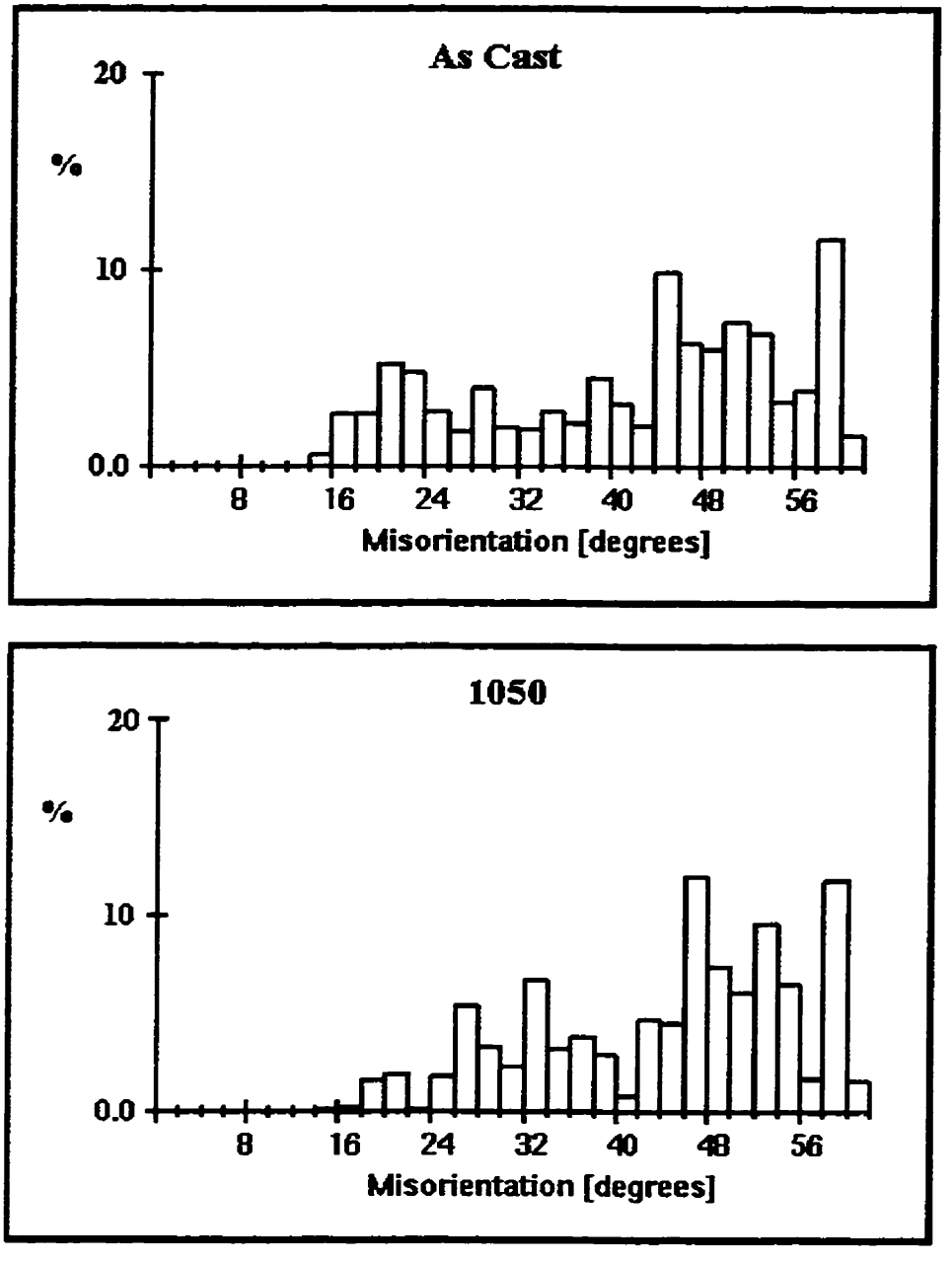

Figure 4-27: Grain boundary misorientation angle distribution for as cast (top) and 1050 °C solution heat treated (bottom) specimens.

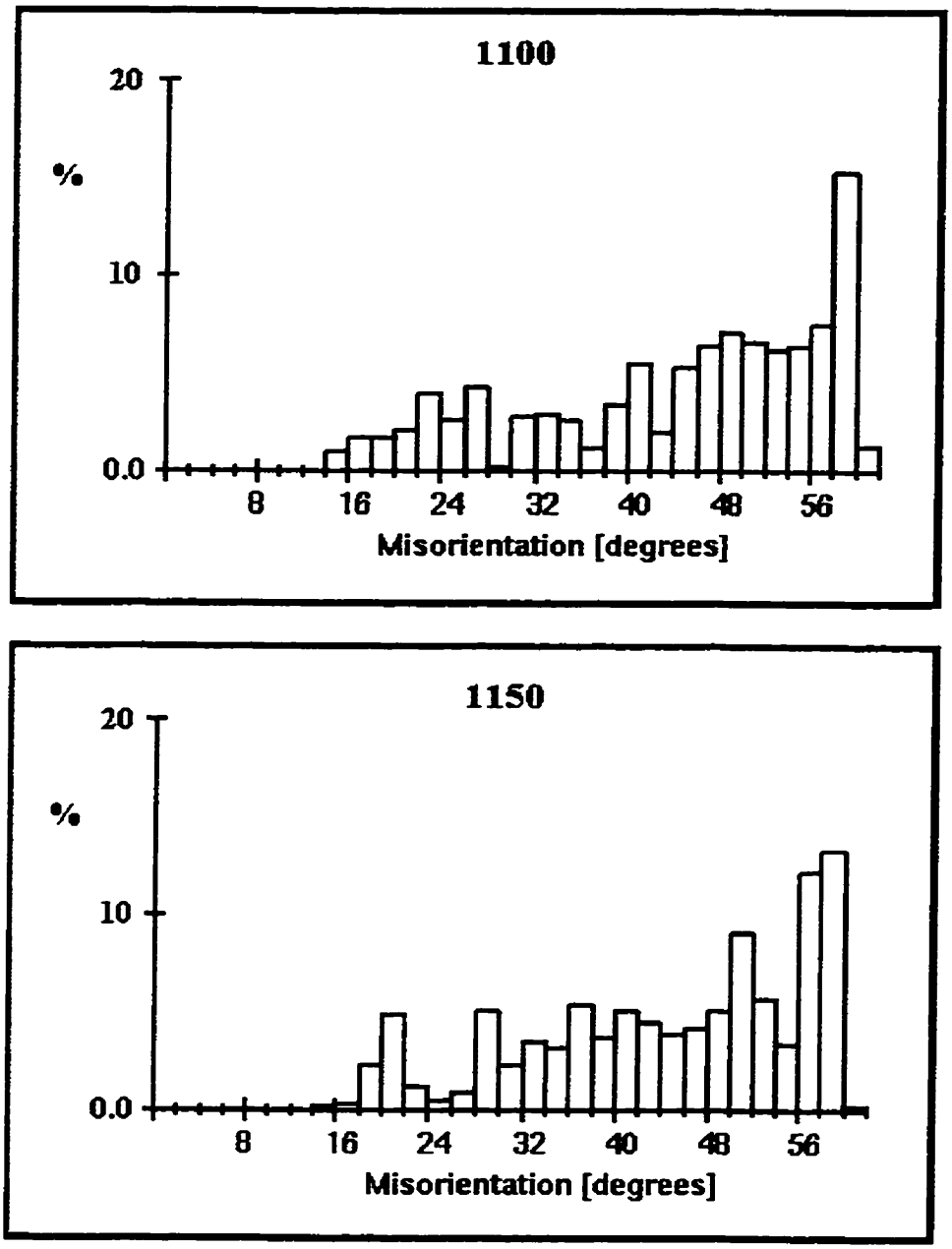

Figure 4-28: Grain boundary misorientation angle distribution for 1100 °C (top) and 1150 °C (bottom) solution heat treated specimens.

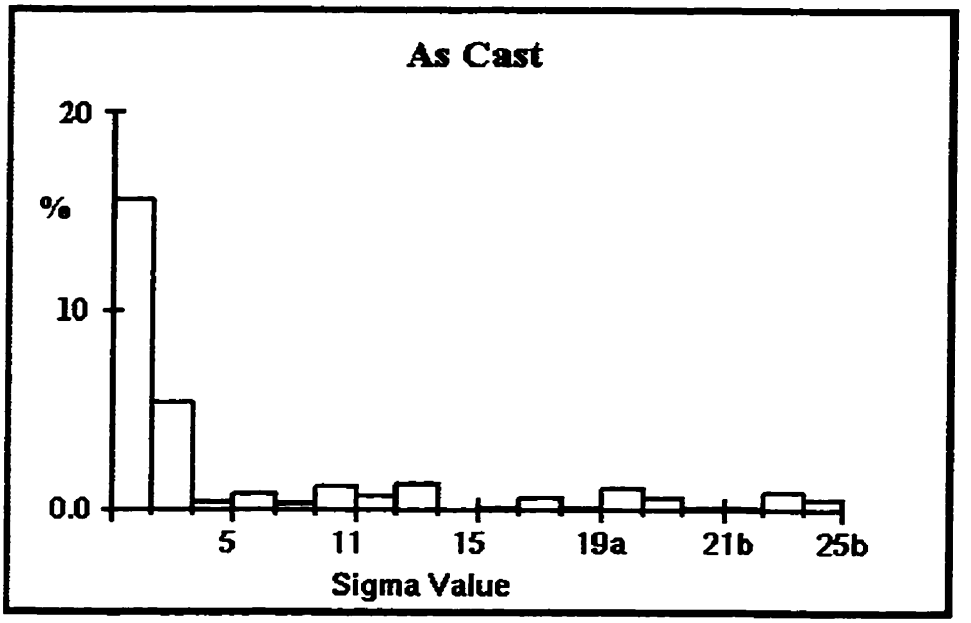

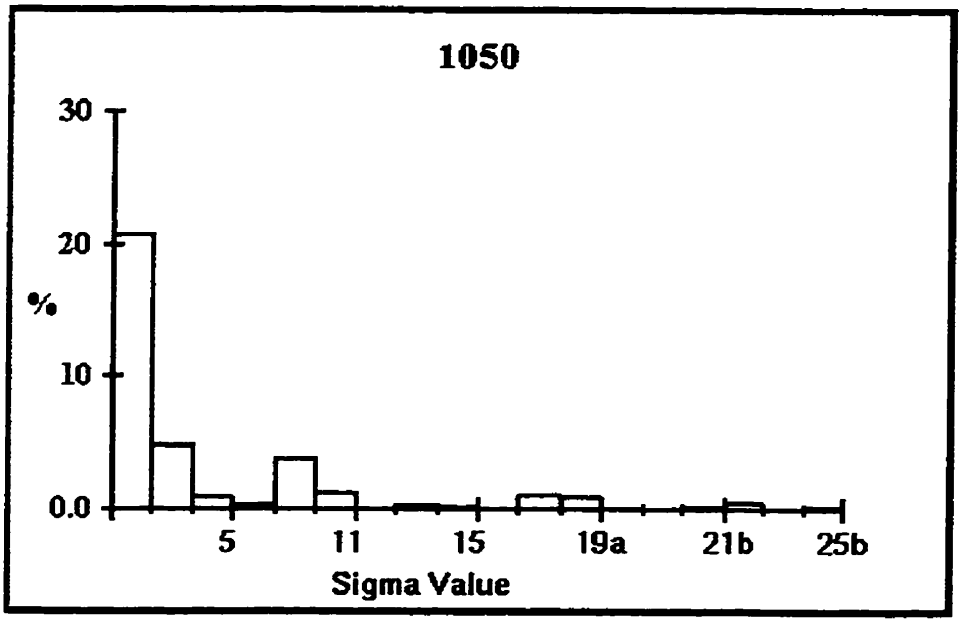

Figure 4-29: CSL boundary distribution for as-cast (top) and 1050 °C solution heat treated (bottom) specimens.

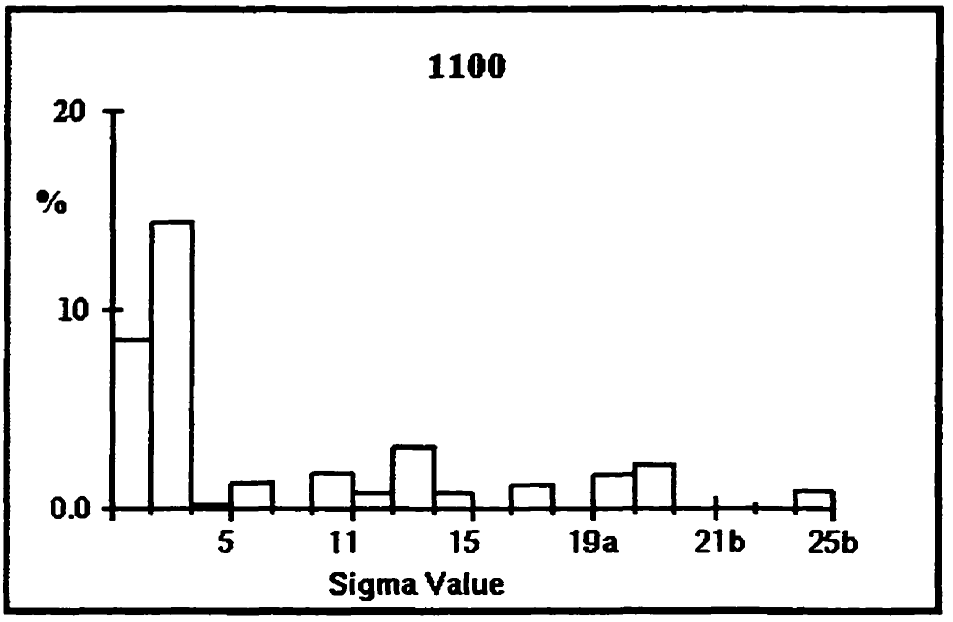

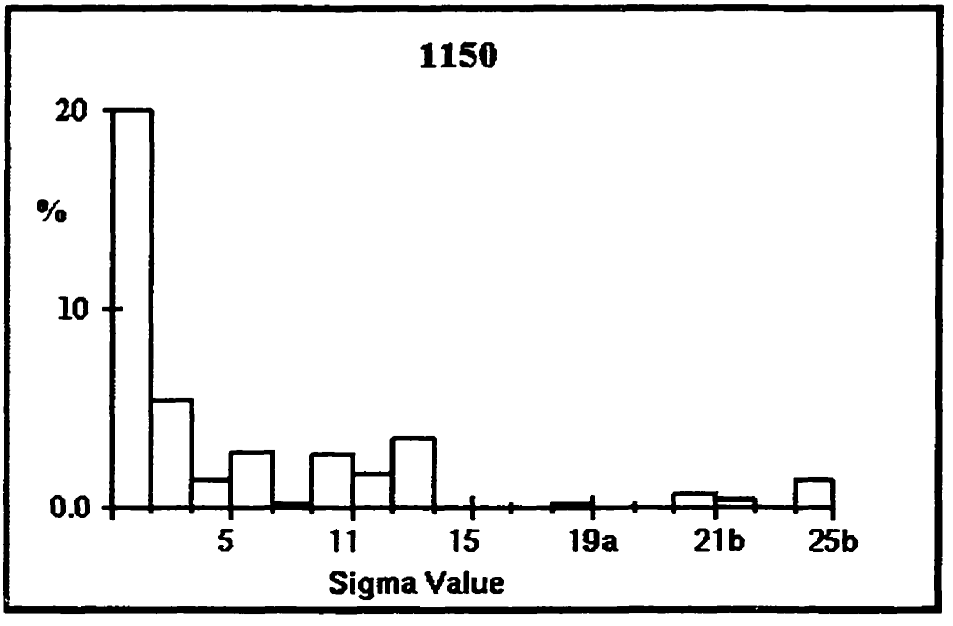

Figure 4-30: CSL boundary distribution for 1100 °C (top) and 1150 °C solution heat treated (bottom) specimens.

4.9 EB Weld Microstructure and HAZ Microfissuring

4.9.1 Fusion Zone Microstructure and Weld Profile

Fusion zone microstructure was observed to be of fine dendritic structure, as shown in Figures 4-31, with an interdendritic precipitate phase shown in Figure 4-32. Weld shape was observed to be of a "nail" shape common to high energy, deeply penetrating EB welds. Pre-weld heat treatments did not have any observable effect on fusion zone microstructure.

Table 4-6: SEM/EDS Chemical Composition of Interdendritic and Dendritic Regions of Microcast-X IN-718 Weld Metal and Base Metal (wt%)

Phase	Nb	Mo	Ni	Fe	Cr	Ti	Al	Si	Nb+Mo
Interdendritic	22.7	9.2	33.5	20.3	12.2	1.8	-	0.3	31.9
Dendritic	3.0	4.9	42.7	31.4	16.6	1.1	0.2	0.1	7.9
Base Metal	6.0	5.0	41.8	28.0	16.7	1.5	0.5	0.4	11.0

Figure 4-31: Optical micrograph of EB weld fusion zone at low magnification.

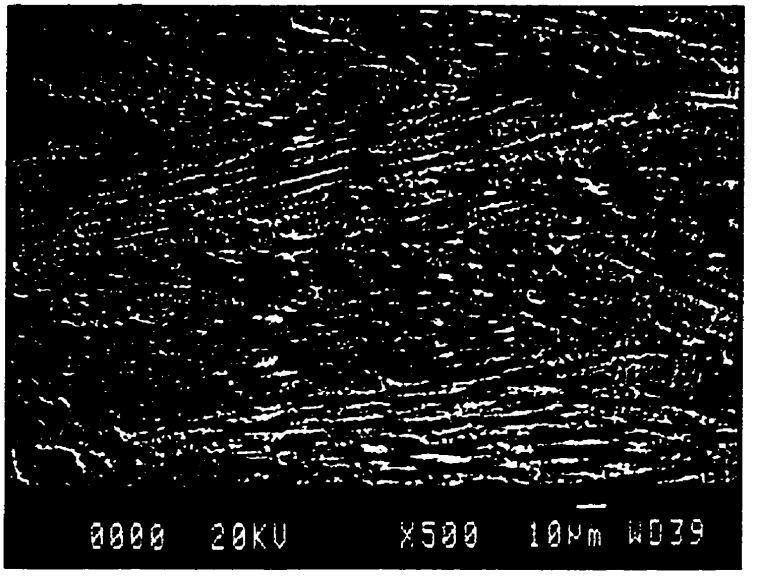

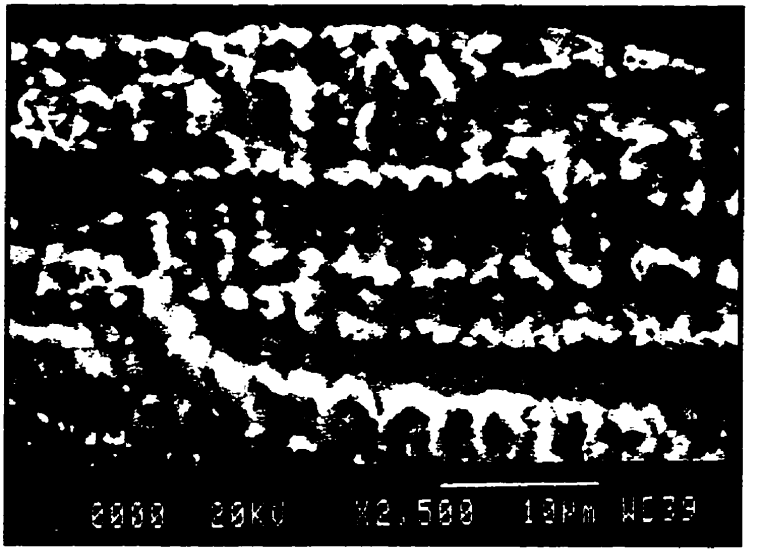

Figure 4-32: SEM micrographs of EB weld fusion zone at 500X magnification (top) and 2500X magnification (bottom) showing interdendritic eutectic phase.

4.9.2 HAZ Microstructure and HAZ Area Estimation

HAZ area is considered to be constant throughout all the samples due to the constancy of the material type and welding parameters. HAZ area estimation is difficult as no detectable grain growth was observed. HAZ limit was thus estimated by the extent of partial liquation of Laves phase in the as-cast material which is clearly visible at 200X magnification. Total HAZ area was estimated to be 3.00 mm^2 using the Leitz Image Analyzer which was carefully calibrated to give accurate measurements.

No visible grain growth was detected in the heat affected zone of the electron beam welds analyzed owing to the low heat input due to high travel speed and also the small heat affected zones characteristic of electron beam welds. HAZ regions were, like the base metal, generally devoid of precipitates other than carbides which appeared to remain unaffected. Small amounts of liquated Laves phase was observed in some specimens in which small amounts of residual Laves phase existed. Extensive Laves phase liquation in the HAZ was noted in the EB welded as-cast material leading to large networks of interconnected resolidified grain boundary liquid in the HAZ. Weld cross-sections which intercepted large porosity clusters were eliminated from the microfissuring analysis to eliminate porosity interference with cracking behaviour and microfissuring analysis results. Fortunately high porosity levels appeared in only a few sections.

4.9.3 HAZ Microfissuring Analysis

4.9.3.1 HAZ Microfissuring: Microstructural Examination

HAZ microfissuring was often observed to be accompanied by a resolidified liquid phase appearing along the microfissure as shown in Figure 4-33. Cracking was most extensive under the nail head of the welds with both longer and more numerous cracks appearing in the area. In water quenched specimens almost all cracks occurred under the nail head. No cracking within the weld metal was found.

Air cooled specimens demonstrated both longer microfissures and a larger number of microfissures. Both air cooled and water quenched specimens contained significant amounts of resolidified grain boundary liquid appearing along HAZ microfissures. No cracks were detected within the fusion zone other than small extensions of HAZ microfissures leading into the weld metal. HAZ microfissures were also noted to begin primarily at the HAZ - fusion zone interface but were also capable of occurring away from the fusion zone boundary. HAZ microfissures were capable of passing through several grain boundary triple points, however, many cracks did end at triple points thereby suggesting that grain boundary triple points may act as both crack initiation sites and to arrest crack propagation.

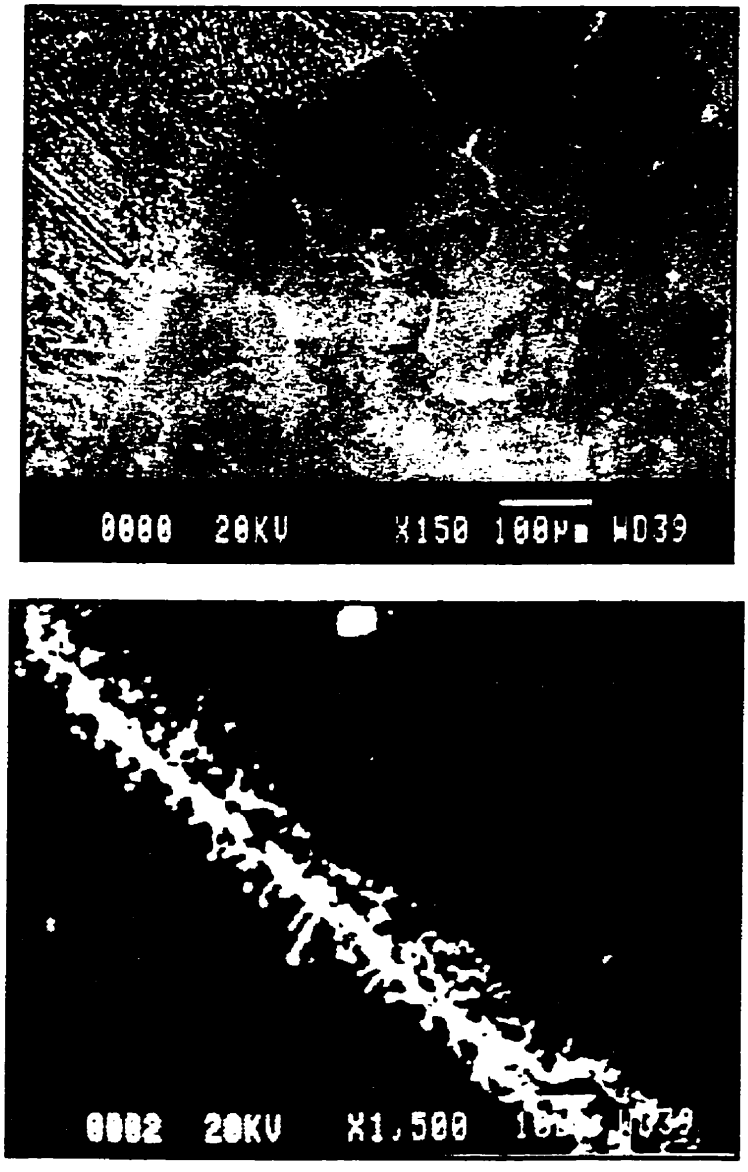

Figure 4-33: Intergranular HAZ microfissure with re-solidified grain boundary liquid phase at 150X (top) and 1500X (bottom) magnification

4.9.3.2 HAZ Microfissuring Evaluation

HAZ microfissuring evaluation involved the measurement of each microcrack detected in each cross-section analyzed for each heat treatment condition. Between 12 and 16 cross-sections were analyzed for each condition resulting in the microfissuring evaluation presented in Figures 4-34 to 4-37 on the following pages. Note that two separate heat treatment sets were created and the results combined into one large set for each heat treatment condition. Measurements are of course subject to human error and interpretation but are consistent laterally within the data set since all measurements were performed in the same manner by the same observer. Tables 4-6 and 4-7 present the overall results.

Heat Treatment	Maximum Crack Length (μm)	Average No. of Cracks	Average Crack Length (μm)
As-Cast (none)	245 ± 28	10.7	106 ± 13
H+S1050WQ	311 ± 40	8.7	125 ± 18
H+S1100WQ	304 ± 36	13.8	117 ± 11
H+S1150WQ	359 ± 49	12.2	142 ± 17
H+S1050AC	300 ± 54	12.8	122 ± 14
H+S1100AC	376 ± 49	15.1	124 ± 13
H+S1150AC	390 ± 70	20.6	123 ± 12

Heat Treatment	Total Crack Length (μm)	Cracking Index (x 10^{-4} μm/μm^2)
As-Cast (none)	1122 ± 117	3.87 ± 0.40
H+S1050WQ	1088 ± 114	3.75 ± 0.39
H+S1100WQ	1611 ± 135	5.56 ± 0.47
H+S1150WQ	1668 ± 154	5.75 ± 0.53
H+S1050AC	1551 ± 146	5.35 ± 0.50
H+S1100AC	1878 ± 147	6.48 ± 0.51
H+S1150AC	2525 ± 330	8.71 ± 1.14

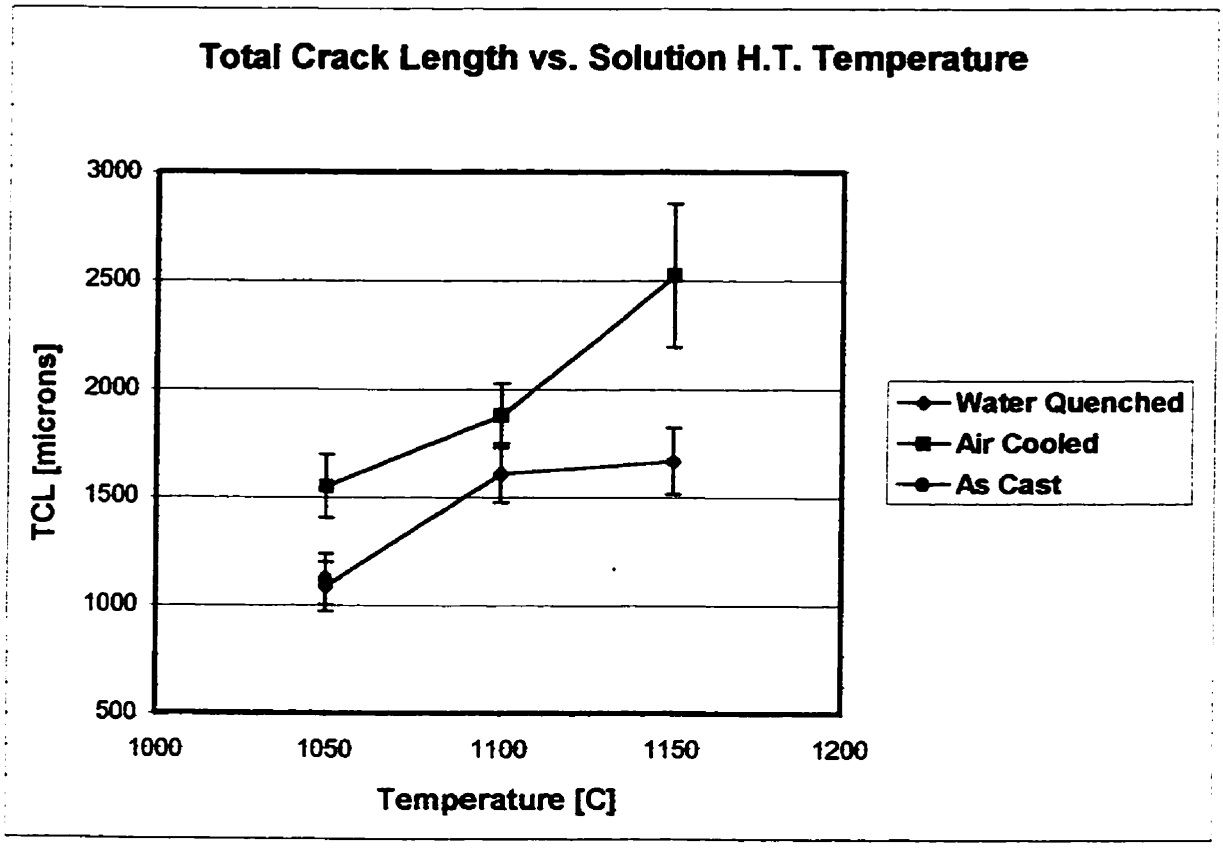

Figure 4-34: Variation in total crack length (TCL) with heat treatment temperature and cooling rate.

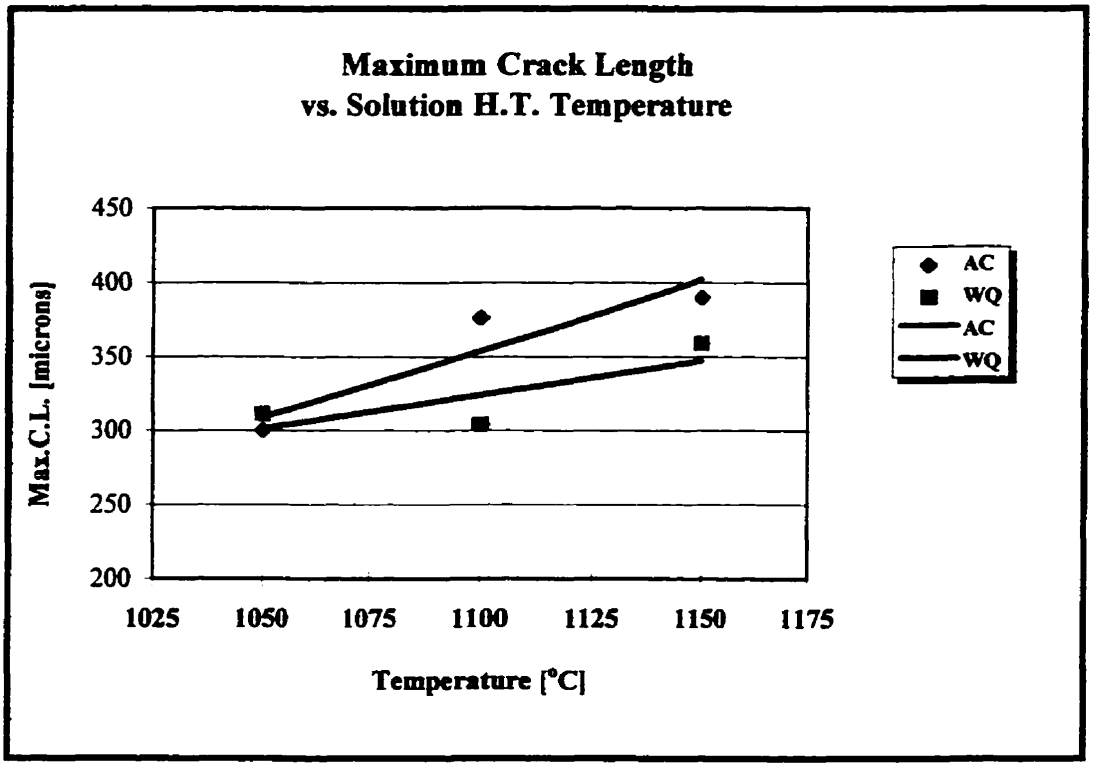

Figure 4-35: Variation in maximum crack length with heat treatment temperature and cooling rate.

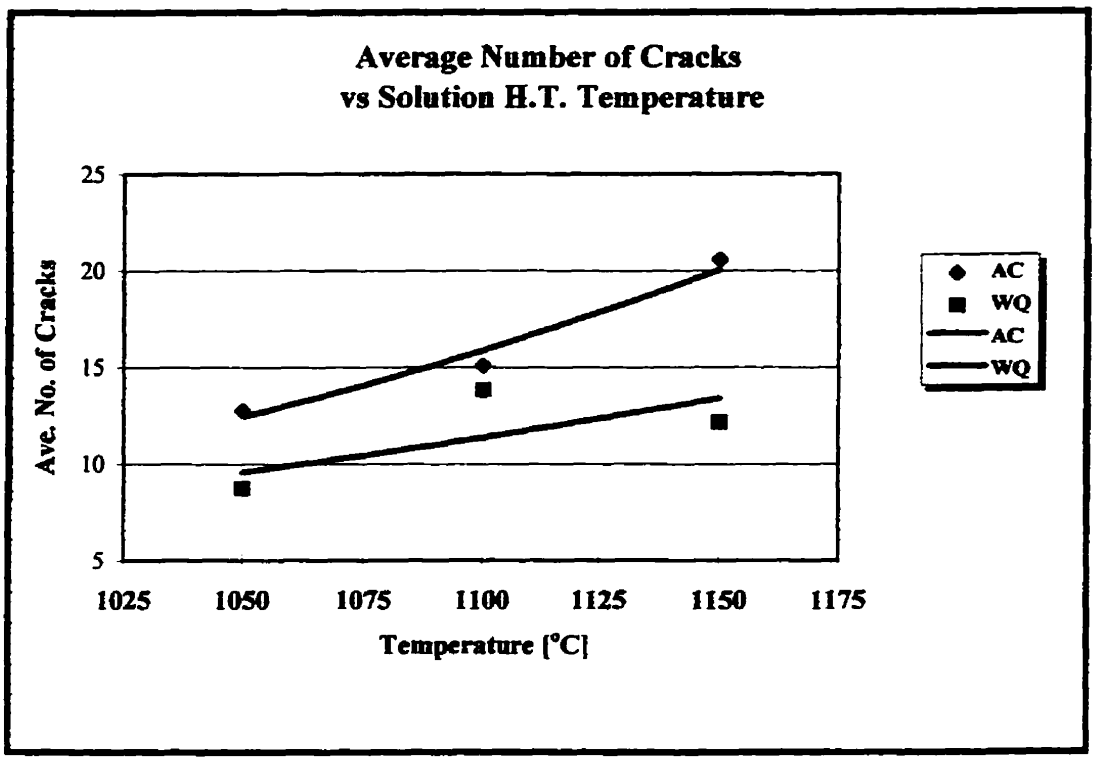

Figure 4-36: Variation in average number of cracks with heat treatment temperature and cooling rate.

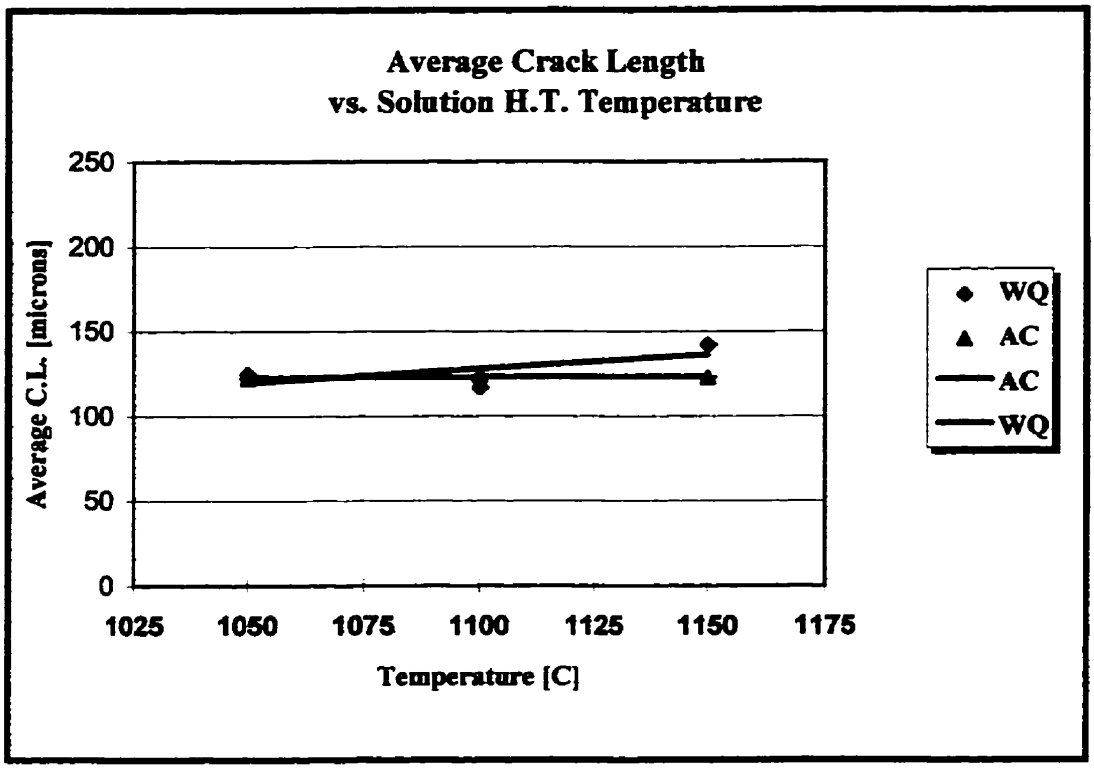

Figure 4-37: Variation in average crack length with heat treatment temperature and cooling rate.

CHAPTER FIVE

DISCUSSION

5.1 Microstructural Examination

5.1.1 Microstructure of As-Received Microcast-X 718 Material

As expected, the microcast material is observed to be formed of equiaxed, non-dendritic, fine grains of ASTM grain size 4 to 5. Solidification of this material has resulted in niobium concentration at the grain boundaries resulting in the formation of Laves phase surrounded by dense clusters of γ'' as shown in Figures 4-1 and 4-2. Carbide (and carbonitride) precipitation occurs both inter- and intragranularily and was found to be most often NbC and (Nb,Mo,Ti)(C,N) of irregular lobed morphology. Form and orientation of carbide particles appeared to be random. δ phase was not common in the as-cast material but appeared occasionally as long needles extending from the intergranular Laves phase.

5.1.2 Microstructure After Homogenization and Solution Heat Treatments

Laves and γ'' precipitates were found to dissolve almost completely after the initial 1200 °C heat treatment, H, and carbide content and morphology was found to remain stable during

homogenization. Grain growth was sporadic and rapid for heat treatments exceeding two hours at 1200 °C and after slightly longer times at lower temperatures. Similar rapid rates in grain growth in wrought 718 when heat treated at 1200 °C were observed by Thompson [41]. Liquation of Laves phase was found to occur under circumstances of rapid heating thereby requiring slow heating rates (~3 °C/min) for temperatures exceeding 1000 °C. The ideal homogenization heat treatment was established and appropriate solution heat treatment temperatures and times were calculated. Results demonstrated that, as desired, the fine grain size was maintained after these solution heat treatments, however, extensive δ precipitation (Fig. 4-7) occurred at a solution heat treatment temperature of 1000 °C. Thus the final solution heat treatment temperatures chosen were necessarily limited to 1050, 1100, and 1150 °C. Precipitates remaining in the solution heat treated specimens includes carbides, and fine boride and sulfide particles.

5.1.3 Fusion Zone Microstructure

Fusion zone microstructure was characteristic of rapid solidification with fine dendrite needles growing virtually perpendicular to the fusion zone boundary toward the weld centerline. Fine dendritic structures in EB welds of 718 are common due to the high cooling rates achievable through lower overall heat input levels (highly localized) and high weld travel speeds [42]. This also results in a smaller heat-affected zone (HAZ) area. As shown in Figure 4-32, the interdendritic regions of the weld metal consist of a precipitate phase. It is

suggested that this interdendritic phase is Laves phase as found in other investigations [42] and as would be expected from solidification theory as it relates to alloy 718. Table 5-1 displays the quantitative EPMA results of Radhakrishnan (et al.) for EB welded cast 718 in as-welded condition (no post weld heat treatment) [42]. Figure 5-1 presents a comparison of niobium levels in the dendritic and interdendritic regions of the fusion and the base metal to show the strong relative agreement between the results of Radhakrishnan (et al.) and of this study.

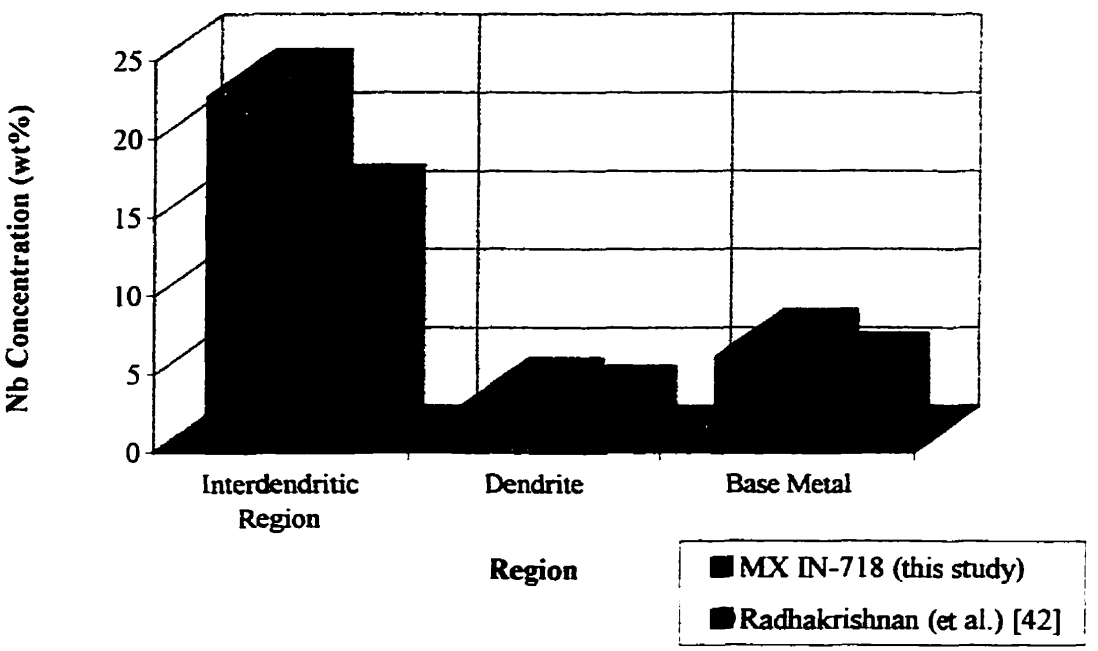

Figure 5-1: Comparison of EB weld fusion zone niobium levels via EDS detection for this study and those found by Radhakrishnan (et al.) [42].

Region	Nb	Ni	Cr	Fe	Mo	Si	Ti
Interdendritic Laves	15.347	49.521	16.084	15.564	3.220	0.144	1.465
Dendritic (matrix)	2.486	50.450	19.212	20.947	2.506	0.058	0.662
Base metal	4.621	52.367	18.426	19.837	2.714	0.044	0.923

5.1.4 HAZ Microstructure and HAZ Microfissuring

Weld specimens heat treated prior to welding did not show any consistent re-precipitation of discrete Laves phase in the HAZ, however resolidified HAZ grain boundary liquid (GBL) was common, especially along HAZ microfissures. Other investigators found similar resolidified products in the HAZ close to the fusion zone in cast and wrought 718 [17, 24, 32, 43]. The EDS results from this study for Laves phase and HAZ grain boundary liquid and those of Huang for EB welded cast 718 [24], Baeslack and Nelson for GTA welded cast 718 [32], Radhakrishnan and Thompson for Gleeble simulated HAZ in wrought 718 [43], and Vincent for EB welded wrought 718 [17] are presented in Table 5-2 for comparison. The results presented in Table 5-2 show strong agreement between Laves EDS scans which fall within experimental error. The primary source for HAZ GBL in as-cast specimens appears to be liquation of Laves phase. HAZ GBL in solution heat treated specimens are likely a resolidified Laves/γ eutectic liquid as theorized by Knorovsky (et al.) or a γ-Laves-NbC pseudo-ternary eutectic as suggested by Radhakrishnan (et al.). The composition of

HAZ GBL may vary depending upon the immediate sources of this liquid in each case since HAZ grain boundary liquid may stem from several sources [43].

Region	Nb+Mo	Ni	Cr	Fe	Si	Ti
Laves (this study)	38.73	32.81	10.05	15.84	0.12	2.46
Laves [32]	33.0	40.6	12.7	13.1	na	0.6
Laves [24]	31.9	38.5	13.5	12.5	4.0	2.5
Laves [43]	27.3	45.2	13.0	11.6	na	1.1
Laves [17]	33.0	44.0	15.5	12.0	2.0	2.5
HAZ GBL as-cast	37.74	31.99	10.57	17.23	0.23	2.16
HAZ GBL sol. h.t.	16.75	41.63	15.00	24.53	0.12	1.72
HAZ GBL Laves [24]	37.22	36.04	13.01	11.82	0.98	2.09
Laves/γ eutectic [32]	27.6	44.3	14.1	12.4	na	1.6
Eutectic γ [43]	12.7	58.3	14.2	12.8	na	1.7
Base metal	7.34	52.37	18.43	19.84	0.04	0.92

One source of the HAZ grain boundary liquid is residual Laves phase present at the time of welding, however, this was minimal for solution heat treated samples used in this study. Weld metal backfilling is also one source of HAZ grain boundary liquid but cannot account for all of it. Backfilling is common since interdendritic regions containing Laves or Laves-γ eutectic type constituents of high niobium content in the weld metal often correspond to HAZ grain boundary intercepts at the fusion zone boundary. Interdendritic liquid weld metal, high in niobium, migrates along HAZ grain boundaries and thus further encourages liquation

cracking. Vincent observed Laves "walls" in HAZ microfissures immediately adjacent to the fusion zone and suggested that this was "a rapidly-frozen liquid phase drawn in from the weld pool as the microfissure is formed" [17].

Carbide liquation is also a source of Nb for this Nb-rich HAZ grain boundary liquid, however, the carbide liquation temperature has been found to be between 1215 and 1235 °C [43] and several investigators have indicated HAZ carbide liquation to be uncommon [32]. It was also observed in this study that, even though some carbide liquation was noticed, many unaffected NbC particles where situated in the HAZ immediately adjacent to the fusion zone and thus carbide liquation is likely a source for the some of observed HAZ grain boundary liquid but not the primary source.

Another potential source for resolidified HAZ GBL stems from the nature of HAZ grain boundary liquation and resolidification itself. As discussed in Chapter 2, niobium will be in high concentrations in the regions adjacent to the grain boundaries due to the solidification process and the relative immobility of niobium in the γ matrix during heat treatments. During the welding cycle, HAZ grain boundaries themselves liquate and this liquid will be rich in niobium. The grain boundary liquid becomes further enriched in niobium as resolidification proceeds inward from the grain boundary walls pushing niobium ahead of the solid-liquid interface. Finally, in similar fashion to the interdendritic regions of the fusion zone, the liquid reaches the Laves-γ eutectic composition and solidifies. A weak, brittle secondary phase film now exists at the HAZ grain boundaries which is highly susceptible to cracking since it is

incapable of withstanding the remaining stresses from thermal contraction and expansion and other residual welding stresses. Similar observations were made by Vincent which support this argument [17].

It is also important to note that HAZ microfissuring was found in all specimens and the greatest degree of microfissuring and longest microfissures were invariably detected in the area of the HAZ located just under the "nail-head" of the weld. This indicates that the shoulder of the weld is the region of highest stress concentration and these stress levels will depend primarily on the welding parameters, joint characteristics and work piece fixturing.

5.2 Elemental Grain Boundary Segregation of Boron and Sulfur

5.2.1 Effect of Heat Treatment Temperature on Boron Segregation

As shown in Figures 4-17 to 4-20 the degree of boron segregation to grain boundaries was qualitatively observed to increase significantly with heat treatment temperature in air cooled specimens and showed a slight increase with increasing heat treatment temperature for water quenched specimens. Since the heat treatment temperatures are relatively high, non-equilibrium segregation is expected to occur even for high cooling rates such as water quenching was detected in the water quenched specimens. Thus it can be stated that a higher solution heat treatment temperature will provide a higher energy initial state for non-

equilibrium segregation to occur upon cooling. This results in higher diffusion rates from the increased number of vacancies available at higher temperatures as well as extra diffusion time available during cooling from a higher heat treatment temperature for a given cooling rate. As expected, as heat treatment temperature increased the magnitude of non-equilibrium segregation increased for a given cooling rate.

5.2.2 Effect of Cooling Rate on Boron Segregation

It is also important to note that the air cooled specimens showed much greater boron segregation than the water quenched specimens for any given solution heat treatment temperature. These results confirm that boron segregation is predominantly of non-equilibrium type and is highest for the slower cooling rate (air cooling) as also found by Karlsson [26].

It is important to note that SIMS analysis of the as-cast material showed boron to reside in the vicinity of the grain boundaries but was not solely concentrated directly at the grain boundaries. Heat treating causes boron to diffuse evenly throughout the grains via equilibrium segregation, as previously discussed, followed by non-equilibrium segregation of boron to the grain boundaries upon cooling.

5.2.3 Sulfur Segregation

Solution heat treatment times were devised to provide the same level of equilibrium segregation of sulfur for the different heat treatment temperatures. Results indicated that sulfur was primarily precipitated as fine sulfide particles with some segregation to grain boundaries. Levels of segregation of sulfur to grain boundaries appeared to be fairly equal among the different heat treatments used, yet further work would be needed to determine conclusively if this is the case.

5.2.4 Grain Boundary Orientation

OIM results suggested that crystallographic orientations and types of grain boundaries in all specimens were of random orientation with high angle grain boundaries predominating and independent of heat treatment temperature and whether the material was heat treated or not. These results further serve to confirm that no special mechanisms of microfissuring were dominating for any particular heat treatment. This further supports the finding that overall segregation of boron increases with increasing solution heat treatment temperature and decreasing cooling rate and is not, in this study, a case of preferred grain orientations encouraging additional boron segregation and possibly affecting microfissuring.

5.3 HAZ Microfissuring Analysis

5.3.1 Constants

When analyzing microfissuring susceptibility, variables which were held constant must be noted in order to pinpoint the factors affecting HAZ microfissuring. Grain size was held constant in order to eliminate grain size effects as well as to maintain the fine-grained MXcast structure. Welding parameters were maintained constant and all welding was performed under the same conditions at the same time in order to eliminate potential for welding variables to affect results and also to enable comparison with some of Dr. Huang's work on conventionally cast 718 which used the same EB welding parameters [24,27]. Welding was conducted along the same face of each specimen in order to eliminate any differences in casting orientations although none were observed in the cast structure. OIM results further support the lack of preferred crystallographic orientation in all specimens both heat treated and as-cast.

Solution heat treated microstructures were devoid of most precipitates other than carbide, carbonitride and sulfide particles which virtually eliminates the effect of other secondary phases such as δ, Laves, or γ'' on HAZ microfissuring. Solution heat treatments were all conducted in the same furnace with equal sized specimens in order to maintain heating and cooling parameters (e.g. heat convection and conduction rates) constant. This was achieved by maintaining a constant cross-section and specimen size and orientation in the furnace. All

specimens were furthermore heat treated in argon-filled high temperature glass capsules to virtually eliminate oxide formation. Therefore, the only directly observed difference between the various heat treated specimens involved boron segregation level.

5.3.2 Effect of Heat Treatment on HAZ Microfissuring

The results indicate that overall microfissuring followed the same trend as boron segregation levels, that is, increasing microfissuring with increasing heat treatment temperature with an increase in microfissuring of air cooled specimens as compared to water quenched specimens for each heat treatment temperature. Since no changes in the type of microfissuring but only levels of microfissuring severity was noted for different heat treated conditions, the results suggest a definite correlation between magnitude of elemental boron segregation to grain boundaries and microfissuring susceptibility.

Results are difficult to compare to Huang's work [24] at this time since Huang's heat treatment times and temperatures were different from those used here. However, Huang's results generally tend to indicate slightly greater values for microfissuring of conventionally cast 718 as compared to those found in this study for MXcast 718. More extensive work using conventionally cast, MXcast, and wrought material of the same composition would be needed to compare microfissuring susceptibility of the three different alloy microstructures.

In order to further analyze the microfissuring data, results were separated into the average maximum crack length, the overall average crack length, and the average number of cracks as presented in Figures 4-34 to 4-37. Results indicate that no single parameter increases with heat treatment temperature or cooling rate but rather both maximum crack lengths and number of cracks generally increase. These trends, along with microstructural observations, indicate that microfissuring severity is aggravated overall with higher solution heat treatment temperature and not limited to one area or mechanism.

The results of this study have shown that the degree of microfissuring correlated well with the observed level of elemental boron segregation to grain boundaries. Furthermore, both observations and numerical results suggest that the same mechanisms of microfissuring were operating in all types of heat treated specimens. This is consistent since it has been suggested that boron acts as a grain boundary melting point suppressant and thus specimens with increased levels of boron segregation will be subject to additional HAZ grain boundary melting and produce additional grain boundary liquid. The mechanisms of HAZ microfissuring remain the same in each case as described in section 5.1.4 and are not dependent upon pre-weld solution heat treatment temperature or cooling rate.

CHAPTER SIX

CONCLUSIONS

1. The fine grain size of the MX-cast Inconel 718 material may be maintained in pre-weld heat treatments through short homogenization heat treatment time and solution heat treatments between 1050 and 1150 °C. These heat treatments will result in a "clean" pre-weld microstructure virtually free of Laves, γ'', δ phase precipitates.
2. The precipitate phases found in the MXcast material were NbC carbides and (Nb, Mo, Ti)(C,N) carbonitrides and intergranular Laves phase surrounded by γ'' particles with occasional appearances of δ needles.
3. Hardness dropped to a consistent level for all solution heat treated conditions from the original as-cast hardness level.
4. Resolidified HAZ grain boundary liquid was found to have a higher Nb content in as-cast weld specimens as compared solution heat treated specimens suggesting that the origin of the HAZ grain boundary liquid is primarily liquation of Laves phase in as-cast specimens and more likely to be a resolidified Laves/γ eutectic liquid stemming from several different sources including HAZ grain boundary melting in solution heat treated specimens.
5. Boron segregation to grain boundaries was observed to increase with increasing solution heat treatment temperature and was higher in air cooled specimens as compared to water quenched specimens at each solution heat treatment temperature.
6. Sulfur was observed to be primarily concentrated in globular sulfide particles that precipitated both along grain boundaries and within grains in solution heat treated

specimens. Sulfur distribution was observed qualitatively through SIMS to be fairly equivalent for all heat treatments and thus independent of cooling rate and consistent with the estimated equilibrium segregation times which were used for each solution heat treatment temperature.

7. Crystallographic orientations were found to be random with high angle grain boundaries being most common.
8. HAZ microfissuring susceptibility correlated well with observed levels of boron grain boundary segregation.
9. HAZ liquation cracking is therefore suggested to be directly related to the concentration of elemental boron at grain boundaries during welding. It is apparent that a higher level of boron grain boundary segregation will cause additional melting and wetting of HAZ grain boundaries and in turn increase HAZ microfissuring susceptibility.

REFERENCES

[1] Bouse, G.K., Dunham, R.A., and Lane, J., "Mechanical Properties of Fine-Grain Microcast-X Alloy 718 Investment Castings for SSME. Gas Turbine Engine, and Airframe Components", Superalloys 718, 625, 706 and Various Derivatives ed. E.A. Loria, The Minerals, Metals & Materials Society, 1997, pp. 459-468.

[2] Sims, C.T., "Superalloys: Genesis and Character", Superalloys II, ed. Sims, C.T., and Hagel, W.C., John Wiley & Sons, Inc., 1987, pp. 3-26.

[3] Miller, H.E., and Chambers, W.L., "Gas Turbine Design and Superalloys", Superalloys II, ed. Sims, C.T., and Hagel, W.C., John Wiley & Sons, Inc., 1987, pp. 27-57.

[4] Muzyka, D.R., and Brown, E.E.., "Nickel-Iron Alloys", Superalloys II, ed. Sims, C.T., and Hagel, W.C., John Wiley & Sons, Inc., 1987, pp. 165-188.

[5] Schirra, J.J., "Development of an Improved Heat Treatment for Investment Cast Inconel 718 (PWA 649)", Superalloys 718, 625, 706 and Various Derivatives ed. E.A. Loria, The Minerals, Metals & Materials Society, 1997, pp. 439-446.

[6] Overfelt, R.A., Sahai, V., Ko, Y.K., and Berry, J.T., "Porosity in Cast Equiaxed Alloy 718", Superalloys 718, 625, 706 and Various Derivatives ed. E.A. Loria, The Minerals, Metals & Materials Society, 1994, pp. 189-200.

[7] Bouse, G.K., and Behrendt, M.R., "Mechanical Properties of Microcast-X Alloy 718 Fine Grain Investment Castings", Superalloys 718 - Metallurgy and Applications ed. E.A. Loria, The minerals, Metals & Materials Society, 1992, pp. 319-328.

[8] Guo, S., Sun, W., Lu, D., and Hu, Z., "Effect of Minor Elements on Microstructure and Mechanical Properties of IN 718 Alloy" Superalloys 718, 625, 706 and Various Derivatives ed. E.A. Loria, The Minerals, Metals & Materials Society, 1997, pp. 521-530.

[9] Thompson, R.G., and Boutwell, B.A., "Microstructure of Fine Grain Alloy 718 Casting", Superalloys 718, 625, 706 and Various Derivatives ed. E.A. Loria, The Minerals, Metals & Materials Society, 1994, pp. 213-228.

[10] Xie, X., et al., "Segregation Behaviour of Phosphorus and Its Effect on Microstructure and Mechanical Properties in Alloy System Ni-Cr-Fe-Mo-Nb-Ti-Al", Superalloys 718, 625, 706 and Various Derivatives ed. E.A. Loria, The Minerals, Metals & Materials Society, 1997, pp. 531-542.

[11] Horton, J.A., et al., "Microstructural Characterization of Superalloy 718 with Boron and Phosphorous Additions", Superalloys 718, 625, 706 and Various Derivatives ed. E.A. Loria, The Minerals, Metals & Materials Society, 1997, pp. 401-408.

[12] Yu, W., Lu, D., Guo, S., Yuan, J., and Xu, Z., "Effect of Phosphorous on Fatigue Properties of Inconel 718 Alloy" Superalloys 718, 625, 706 and Various Derivatives ed. E.A. Loria, The Minerals, Metals & Materials Society, 1997, pp. 543-551.

[13] Yun, Z., et al., "Delta Phase and Deformation Fracture Behaviour of Inconel 718 Alloy", Superalloys 718, 625, 706 and Various Derivatives ed. E.A. Loria, The Minerals, Metals & Materials Society, 1997, pp. 229-236.

[14] Kelly, T.J., "Elemental Effects on Cast 718 Weldability", Welding Journal, February, 1989, pp. 44s-51s.

[15] Mitchell, A., Schmalz, A.J., Schvezov, C., and Cockcroft, S.L., "The Precipitation of Primary Carbides in Alloy 718", Superalloys 718, 625, 706 and Various Derivatives ed. E.A. Loria, The Minerals, Metals & Materials Society, 1994, pp. 65-78.

[16] Thompson, R.G., Mayo, D.E., and Radhakrishnan, B., "The Relationship between Carbon Content, Microstructure, and Intergranular Liquation Cracking in Cast Nickel Alloy 718", Metallurgical Transactions A, Vol. 22A, February, 1991, pp. 557-567.

[17] Vincent, R., "Precipitation Around Welds in the Nickel-Base Superalloy, Inconel 718", Acta Metall., Vol. 33, No. 7, 1985, pp. 1205-1216.

[18] Mitchell, A., and Schmalz, A.J., "The Role of TiN Precipitation in Determining Microporosity in Castings of IN718 Alloy" - Abstract, Superalloys 718, 625, 706 and Various Derivatives ed. E.A. Loria, The Minerals, Metals & Materials Society, 1997, pp. 119.

[19] Lane, J.M., "Investment-cast superalloys challenge wrought materials", Advanced Materials & Processes, April, 1990, pp. 107-108.

[20] Lane, J.M., "Microcast-X IN-718", Alloy Digest, June, 1995.

[21] Murata, Y., Morinaga, M., Yukawa, N., Ogawa, H., and Kato, M., "Solidification Structures of Inconel 718 with Microalloying Elements", Superalloys 718, 625, 706 and Various Derivatives ed. E.A. Loria, The Minerals, Metals & Materials Society, 1994, pp. 81-88.

[22] ASM Committee on Electron Beam Welding "Electron Beam Welding", Metals Handbook: Ninth Edition, Vol. 6, 1983, 609-646.

[23] Easterling, Kenneth, Introduction to the Physical Metallurgy of Welding, Second Edition, 1992.

[24] Huang, Xiao, A Microstructural Study of Heat Affected Zone Microfissuring of Electron Beam Welds in Cast Alloy 718, Dept. of Mech. and Ind. Engineering , University of Manitoba , July 1994.

[25] Karlsson, L., and Norden, H., "Overview No. 63: Non-equilibrium Grain Boundary Segregation of Boron in Austenitic Stainless Steel - II. Fine Scale Segregation Behaviour" Acta Metall., Vol. 36, No. 1, 1988, pp. 13-24.

[26] Karlsson, L., and Norden, H., and Odelius, H., "Overview No. 63: Non-equilibrium Grain Boundary Segregation of Boron in Austenitic Stainless Steel - I. Large Scale Segregation Behaviour", Acta Metall., Vol. 36, No. 1, 1988, pp. 1-12.

[27] Huang, X., Chaturvedi, M.C., Richards, N.L., "Effect of Homogenization Heat Treatment on the Microstructure and Heat Affected Zone Microfissuring in Welded Cast Alloy 718", Metallurgical and Materials Transactions A, Vol. 27A, March, 1996, pp. 785-790.

[28] Chaturvedi, M.C., Chen, W., Saranchuk, A., and Richards, N.L., "The Effect of B Segregation on Heat-Affected Zone Microfissuring in EB Welded Inconel 718", Superalloys 718, 625, 706 and Various Derivatives ed. E.A. Loria, The Minerals, Metals & Materials Society, 1997, pp. 743-751.

[29] Zhu, Y., et al., "Effect of P, S, B and Si on the Solidification Segregation of Inconel 718 Alloy", Superalloys 718, 625, 706 and Various Derivatives ed. E.A. Loria, The Minerals, Metals & Materials Society, 1994, pp. 89-98.

[30] Mulford, R.A., "Grain Boundary Segregation in Ni and Binary Ni Alloys Doped with Sulfur", Metallurgical Transactions A, Vol. 14A, May, 1983, pp. 865-870.

[31] Thompson, A.W., "Effect of Sulfur Segregation to Grain Boundaries on Yielding, Flow and Fracture of Nickel", Grain Boundaries in Engineering Materials, 1974, pp. 607-618.

[32] Baeslack III, W.A., and Nelson, D.E., "Morphology of Weld Heat-Affect Zone Liquation in Cast Alloy 718", Metallography, Vol. 19, 1986, pp. 371-379.

[33] Mehl, M.E., and Lippold, J.C., "Effect of δ-phase Precipitation on the Repair Weldability of Alloy 718", Superalloys 718, 625, 706 and Various Derivatives ed. E.A. Loria, The Minerals, Metals & Materials Society, 1997, pp 731-741.

[34] Ko, Y.K., and Berry, J.T., "Characterization of the Dendritic Microstructure of Investment Cast Alloy 718", Superalloys 718, 625, 706 and Various Derivatives ed. E.A. Loria, The Minerals, Metals & Materials Society, 1994, pp 201-212.

[35] Thompson, R.G, et al., "The Relationship Between Grain Size and Microfissuring in Alloy 718", Welding Research: Supplement to the Welding Journal, April, 1985, pp. 91s-96s.

[36] Boucher, C., Valera, D., Dadian, M., and Granjon, H., "Hot Cracking and Recent Progress in the Weldability of Nickel Alloys: Inconel 718 and Waspalloy", presented at the 15th Conference of Special Steels, Saint Etienne, 13-14, May, Translation by the Welding Institute, Cambridge, England, 1976.

[37] Hirsch, P.B., et al., Electron Microscopy of Thin Crystals, Butterwirth & Co., London, 1965.

[38] Goldstein, J.L., et al., Scanning Electronm Microscopy and X-Ray Microanalysis, Plenum Press, New York, 1981.

[39] Thornton, P.R., Scanning Electron Microscopy, Chapman and Hall Ltd., London, 1968.

[40] Pantano, C.G., "Secondary Ion Mass Spectrometry", Metals Handbook: Ninth Edition, Vol. 10, ASM Handbook Committee, 1983, pp.610-627.

[41] Radhakrishnan, B., and Thompson, R.G., "Kinetics of Grain Growth in the Weld Heat-Affected Zone of Alloy 718", Metallurgical and Materials Transactions A, Vol. 24A, December, 1993, pp. 2773-2785.

[42] Radhakrishnan, C.H., Rao, K.P., and Srinivas, S., "Laves Phase in Superalloy 718 Weld Metals", Journal of Materials Science Letters, Vol. 14, 1995, pp. 1810-1812.

[43] Radhakrishnan, B., and Thompson, R.G., "A Phase Diagram Approach to Study Liquation Cracking in Alloy 718", Metallurgical and Materials Transactions A, Vol. 22A, April, 1991, pp. 887-901.

IMAGE EVALUATION
TEST TARGET (QA-3)

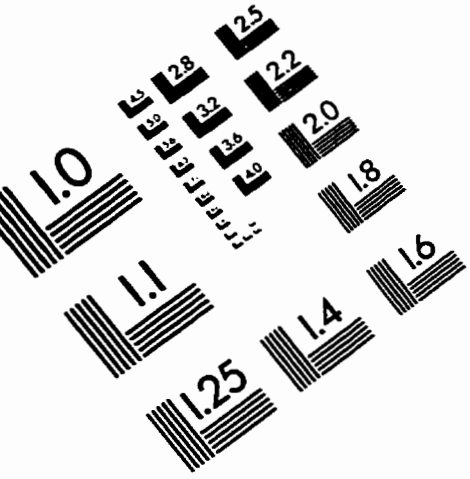

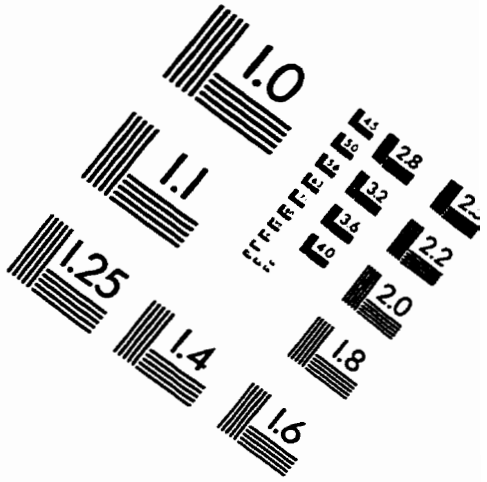

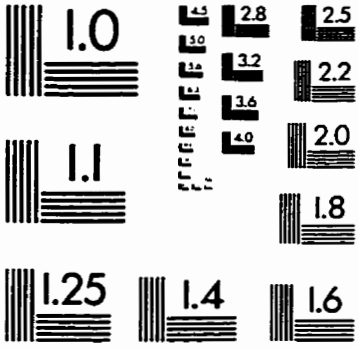

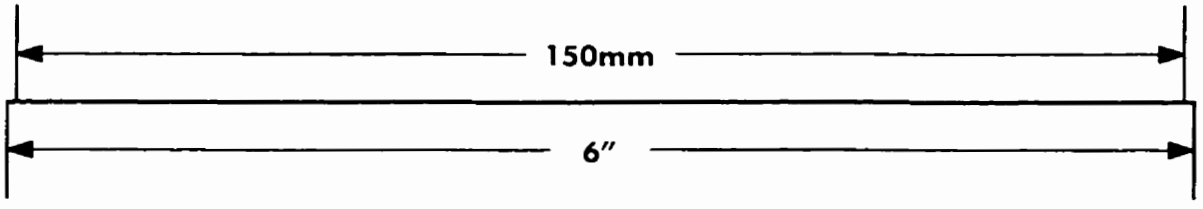

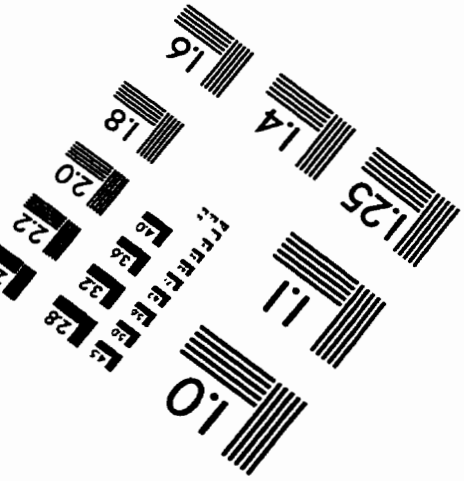

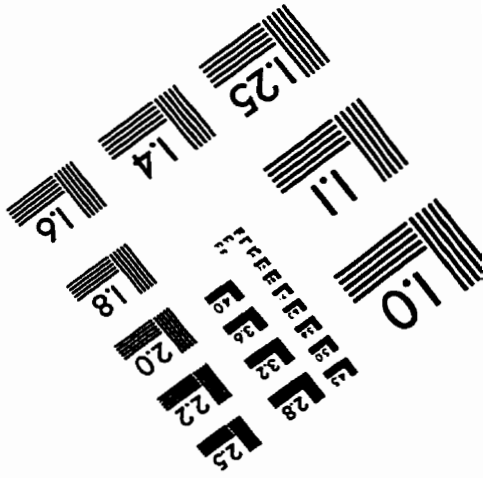

APPLIED IMAGE, Inc
1653 East Main Street
Rochester, NY 14609 USA
Phone: 716/482-0300
Fax: 716/288-5989